

**Topics in Cosmic Ray Measurement and
Particle Detectors Development**
量度宇宙射線及研製粒子探測器

LEUNG, Shing Chau

梁乘宙

A Thesis Submitted in Partial Fulfilment
of the Requirements for the Degree of
Master of Philosophy
in
Physics

The Chinese University of Hong Kong

September 2014

Thesis Assessment Committee

Professor WONG, King Young (Chair)

Professor CHU, Ming Chung (Thesis Supervisor)

Professor ONG, Hock Chun Daniel (Committee Member)

Professor WONG, Tsz King Henry (External Examiner)

Abstract

We developed a multiwire chamber prototype for the CUHK Muon Telescope to measure cosmic muons. We designed, simulated and assembled the chamber, and carried out the related programmings. We also analyzed 1.5 years of cosmic muon data using the muon telescope and compared them to a simulated cosmic muon map. Moreover, we participated in the development of the SEABAS DAQ system for the FE-I4 pixel front-end read-out in the ATLAS experiment at the Large Hadron Collider at CERN.

摘要

吾等研製多絲電離室，用其高方位及高度角解像度量度渺子，吾等詳細設計、模擬、製作及編程此電離室。吾等於一年半內以香港中文大學渺子望遠鏡（CUHK Muon Telescope）量度宇宙射線渺子分佈，並取之與電腦模擬渺子分佈圖比較。再者，吾等參與歐洲核子研究組織（CERN）大型強子對撞器（LHC）之超環面儀器（ATLAS）實驗，助其研發SEABAS資料擷取系統，用其讀出像素探測器內之前端晶片FE-I4。

ACKNOWLEDGMENTS

I wish to express my gratitude to my supervisor, Prof. Ming-Chung Chu, for his guidance on my research and providing me the opportunity to take part in the ATLAS experiment at CERN.

I would thank Dr. Maurice Garcia-Sciveres at Lawrence Berkeley National Laboratory for teaching me about the pixel detector and helping me with the SEABAS project.

I am very grateful for all the collaborators who have assisted me greatly in my projects. I express my greatest thank to K. K. (Soap) Kwan for his hardware knowledge and his works on the wire chamber and muon telescope hardware, firmware and software designs. I thank Y. L. (Wolf) Chan for his cosmic muon map and his help in wire chamber DAQ driver programming. I also thank Dr. Y. H. Tam and K. H. Martin Kwok for their programs and statistical analysis on the muon telescope data. I thank deeply Prof. Shih-Chieh Hsu in the University of Washington in Seattle, Dr. Minoru Hirose in the Tokyo Institute of Technology and J. J. Teoh in the Osaka University for their assistance in the SEABAS project.

Lastly, I give thanks to all the undergraduates, especially P. H. (Benny) Tam, who have participated diligently in the muon telescope and wire chamber researches.

Contents

1	Cosmic Muon Simulation	8
1.1	Introduction	8
1.1.1	Motivation	8
1.1.2	Nature of Cosmic Rays	10
1.2	Distribution of Cosmic Muons	14
1.2.1	Energy and Zenith Angle Dependences	14
1.2.2	Cosmic Muon East-to-West Ratio	16
1.3	The CUHK Muon Telescope	17
1.3.1	Detection Mechanism	18
1.3.2	Angular Resolution	19
1.3.3	Detector Location	25
1.4	Cosmic Muon Simulation	26
1.4.1	Cosmic Muon Data Set	26
1.4.2	East-west Muon Flux Asymmetry Simulation	28
2	Measurement-Simulation Comparison	34
2.1	Methods	34
2.2	Measurement Results	37

	5
2.3 Conclusion	41
3 Wire Chamber Design	43
3.1 Introduction	43
3.2 Structural Design	44
3.3 Operation Specification	50
4 Wire Chamber Simulation by GARFIELD-9	53
4.1 Introduction	53
4.2 Wire Chamber Modeling	54
4.3 Mechanical Equilibrium of the Sensing Wires	57
4.4 Signal Response	60
4.4.1 Event Settings and the Multiplication Factor .	60
4.4.2 Electron Arrival Timings	63
4.4.3 Current Signals	64
4.5 Response to Gas or Geometry Deviation	68
5 CUHK Wire Chamber Front-end	74
5.1 Analog Front-end	74
5.1.1 Introduction	74
5.1.2 Pre-Charge Amplifier Circuit	75
5.1.3 Charge Amplification with Operational Am- plifier	77
5.1.4 Front-end Discriminator	79
5.2 Digital Front-end	81

5.2.1	Introduction	81
5.2.2	SPI Communication between Back-end and Front-end	82
5.2.3	Assignment of Front-end Address with the Ac- tion Button Code	85
5.2.4	Threshold Generation and Scanning	86
5.2.5	Analog Injection Test and Cross-talk Scan . .	88
6	Back-end and Data Acquisition Software	91
6.1	Introduction	91
6.2	FPGA Back-end Module	93
6.2.1	Inter-module Communication	93
6.2.2	Event Builder	95
6.2.3	Singles Rate	98
6.3	DAQ Software	99
6.3.1	Threshold Scan Program	100
6.3.2	Take Data Program	101
7	SEABAS DAQ for ATLAS Pixel Front-end Read-out	102
7.1	Introduction	102
7.1.1	Overview of the Large Hadron Collider	102
7.1.2	Overview of the ATLAS Experiment	104
7.1.3	The ATLAS Pixel Detector	105
7.1.4	FE-I4 Pixel Front-end Chip	106
7.2	The SEABAS DAQ System	109

7.2.1	The SEABAS Boards	109
7.2.2	SEABAS DAQ Firmware and Software	110
8	Conclusion	115
A	Muon Asymmetry Flux Effect Result Table	117
B	List of the SPI Reords for FE-BE Communication	119
C	List of the Back-end Addresses	123
	Bibliography	125

Chapter 1

Cosmic Muon Simulation

1.1 Introduction

1.1.1 Motivation

Cosmic ray muons have always been a subject of interest in both the physics and non-physics communities. Understanding the properties of cosmic muons are essential for many studies.

Cosmic muons are an important background in underground particle physics experiments. Many of those experiments devise various techniques to reject the muon background.

An example is the Daya Bay Reactor Antineutrino Experiment [1]. The antineutrino detector chambers are immersed in a water pool surrounded by photomultiplier tubes (PMT), at the same time covered by resistive plate chambers (RPC) on the top. The combination of the PMTs-water Čerenkov detectors and the RPCs is used to reject the cosmic muon signals so that the antineutrino signals can be extracted from the remaining data [2].

Another example is the ATLAS experiment [3] in the Large Hadron Collider (LHC) at CERN. The ATLAS experiment has a muon spectrometer to identify the muons generated by the LHC proton-proton collisions, and to measure their

tracks, energies and momenta. The muon spectrometer consists of many RPCs, monitored drift tubes (MDT) and thin gap chambers (TGC) modules. The particle tracks from cosmic muons are used to align and verify the relative positions of all those modules [4]. Similar strategies are used in the inner tracker alignment and the track reconstruction commissioning [5].

A detailed understanding of the cosmic muons is critical to these sensitive physics experiments.

Moreover, cosmic rays are closely related to the Earth's and the interplanetary weathers.

Some data suggest that the solar activities affect the cosmic ray flux. The cosmic ray flux is anti-correlated with the 11-year sunspot cycle [6, 7]. Solar activities affect strongly the satellite, atmosphere-based communication and even the entire Earth's climate. The relation between the solar activities and cosmic rays has shown the possibility of studying the space weather through studying cosmic muons.

The cosmic ray flux also affects the Earth's weather. The cosmic ray flux is positively correlated to the Earth's low cloud coverage [7]. Theories suggest that cosmic rays produce ionization clusters in the atmosphere, on which water vapor condenses to form clouds. This effect is recently demonstrated in the CLOUD experiment [8] in CERN. The cloud formation rate is closely connected to the surface albedo of the Earth, which in turn has strong effects on the global temperature and long term climate. The implication is that cosmic rays may provide us a way to indirectly investigate the long term climate trend, such as the global warming.

From a daily life point of view, cosmic muons are high momentum charged particles that can damage or generate soft failures in electronic devices. The effect of cosmic muons is increasingly damaging as the dimension and the operating voltage of the consumer electronics shrink [9, 10]. Like the semiconductor industry, many of the future nano-technologies require a good understanding of

the cosmic ray physics.

Cosmic muons are also a readily available tool to carry out radiography on large man-made or natural structures. The nuclear disaster of Fukushima Daiichi Nuclear Power Plant happened on March 2011 had cost great harm on the local communities and environment. Recently scientists used cosmic ray muons to image the condition of the damaged interior Fukushima Reactors [11]. This radiographic study allows scientists to identify the radioactive core material locations without having to enter the damaged power plant. The potentially challenging and dangerous task is now eased with the use of cosmic rays.

The above examples of cosmic ray studies and their importance have motivated us to develop simulations and particle detectors to predict and measure the properties of the cosmic muons to a high precision.

1.1.2 Nature of Cosmic Rays

Primary cosmic rays are very energetic particles originated isotropically from outside the Earth, in deep space far away from the solar system. The exact origin of the cosmic rays is uncertain. One compelling theory is that high energy particles are Fermi accelerated to cosmic rays by astrophysical shock fronts [12]. One form of such shock fronts is the plasma fluid expelled by a supernova explosion. Charges are trapped in the Alfvén waves of the plasma, and are forced to bounce back-and-forth between the boundaries of the shock front. The net result is the acceleration of the charges to very high energies, up to more than 10^{20} eV. The recent Fermi-LAT satellite observation of supernova remnants [13] offers a strong piece of evidence for this mechanism.

Despite their mysterious origin, various properties of cosmic ray are well-studied. The constituents of primary cosmic rays are 93% protons, 6% helium-4 nuclei, 1% electrons and traces of heavier nuclei and antiparticles [16]. The intensity of the cosmic ray nuclei as a function of the energy-per-nucleon (E)

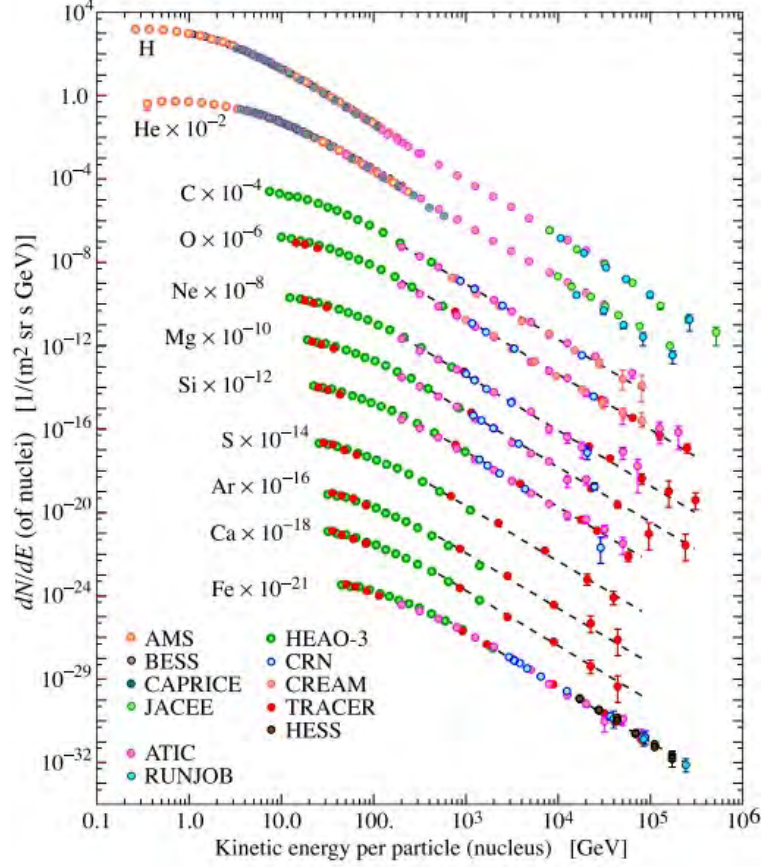


Figure 1.1: The intensities of various elements in cosmic rays versus energy-per-nucleon from Ref. [16].

approximately follows a universal power law:

$$I(E) \propto \left(\frac{E}{1 \text{ GeV}} \right)^{-2.7} \frac{\text{nucleons}}{\text{m}^2 \text{ s sr GeV}}, \quad (1.1)$$

plotted in Fig. 1.1.

Primary cosmic rays have to pass through the Lorentz force shielding by both the helio-magnetic field and the geo-magnetic field before reaching the Earth's outer atmosphere. Cosmic rays with low momenta bend with greater curvatures in a magnetic field. They are deflected off from Earth if their momenta are below a certain threshold, called geomagnetic cutoff rigidity. The cutoff rigidity ranges from 0 GV on the geomagnetic poles to > 14 GV near the equator. A review paper is available in Ref. [14].

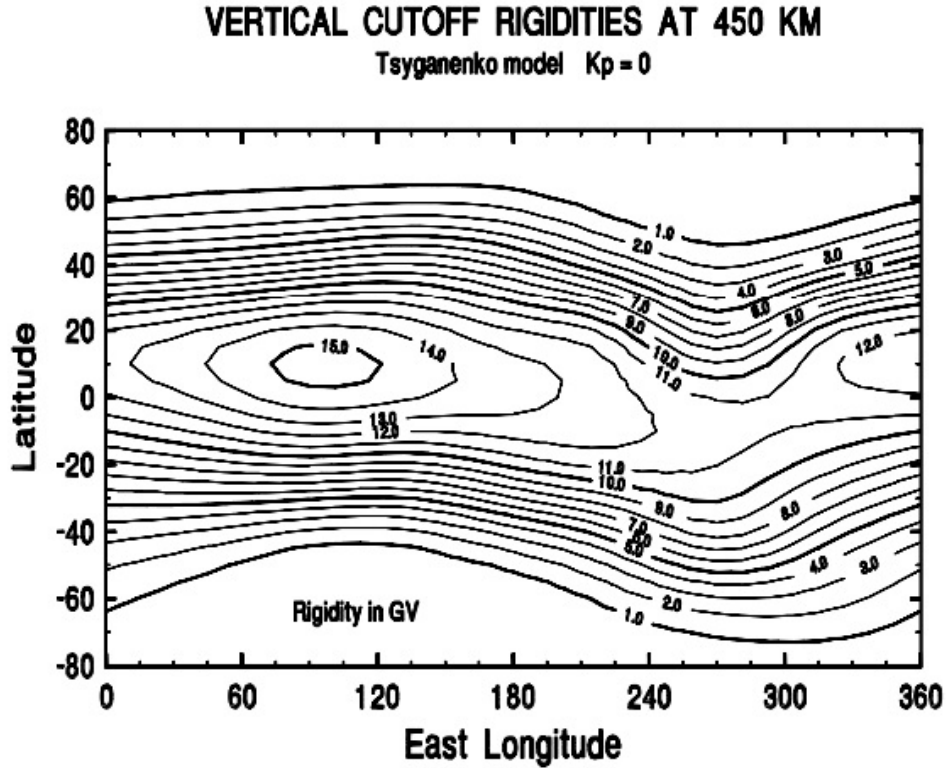


Figure 1.2: A geomagnetic cutoff rigidity contour map at $K_p = 0$. $K_p \in [0, 5]$ is an index to quantify the geomagnetic disturbance under conditions such as solar storm. The unit of the contour plot is in energy per unit charge E/e (GV) since the magnetic field bending is only sensitive to the energy-to-charge ratio. The plot is from Ref. [14].

Hong Kong is among the places with the highest rigidities. The geomagnetic cutoff rigidity above Hong Kong is 16.3 GV extracted from the nearest data point in Ref. [15].

While the cutoff rigidity sets the approximate cutoff for the primary cosmic ray particles, the exact cutoff energy depends on the specific trajectory of each individual particle. The rigidity map also varies with the relative Solar-Earth position and the specific space weather conditions. Geomagnetic storms due to events such as high speed solar winds or solar coronal mass ejections can perturb the rigidity map.

The portion of primary cosmic rays that reaches the Earth does not reach the surface of the Earth directly. The primary particles interact with the particles in the atmosphere strongly and produce hadronic showers. These particles produced by primaries are called secondary cosmic rays. They include protons, neutrons, kaons, pions, muons, electrons and neutrinos, etc. The secondary hadrons interacts strongly in the atmosphere. Most of them either decay or scatter into other particles. Otherwise, together with electrons, they are stopped by energy dissipation before reaching the Earth's surface.

Pions are the mesons that are produced in the greatest quantity in the quantum chromodynamical (QCD) scattering of primary cosmic ray particles in the atmosphere. The second most favored meson state is kaon. Therefore, the two main contributing processes for the production of muon secondaries detected on the ground surface are pion and kaon decays,

$$\begin{aligned}\pi^+ &\longrightarrow \mu^+ + \nu_\mu \\ \pi^- &\longrightarrow \mu^- + \bar{\nu}_\mu\end{aligned}\quad (> 99.9\%) \quad (1.2)$$

and

$$\begin{aligned}K^+ &\longrightarrow \mu^+ + \nu_\mu \\ K^- &\longrightarrow \mu^- + \bar{\nu}_\mu\end{aligned}\quad (63.6\%). \quad (1.3)$$

Some other decay channels of kaon may include pions and electrons production.

While neutrinos rarely interact with any matter, muons are the most common candidates to be investigated as secondary cosmic ray particles. They are easy to detect by both solid and gas detectors as muons are charged leptons. At the same time, cosmic muons arrive at the surface in great quantity since their decay is slowed enough by relativistic time dilation for their trips towards the ground. As a result, cosmic muons are chosen to be the subject of study in this thesis.

1.2 Distribution of Cosmic Muons

Both negatively and positively charged muons can arrive at the ground surface, but their numbers differ by a ratio $N_{\mu+}/N_{\mu-} \approx 1.27$ for the momentum range below 300 GeV/c [18]. The difference arises from the fact that the primary cosmic rays are dominated by protons. The initial condition biases towards positively charged muon generation. Nonetheless without a B-field, our detector is insensitive to the muon charge. In the following discussion, the on muon flux refers to the combined flux of positively and negatively charged muons.

1.2.1 Energy and Zenith Angle Dependences

The first two dependences of cosmic muon distribution is the zenith angle (θ) of the celestial sphere and muon energy (E). The (I, θ, E) -distribution can be described by the modified Gaisser parameterization [20], a slightly simplified version of which is

$$I(E, \theta) = \frac{dN}{dE d\cos\theta} = \frac{0.14}{\text{cm}^2 \text{sr s GeV}} \left[\frac{E}{\text{GeV}} \left(1 + \frac{3.64 \text{ GeV}}{E(\cos\theta^*)^{1.29}} \right) \right]^{-2.7} \times \left(\frac{1}{1 + \frac{1.1E \cos\theta^*}{115 \text{ GeV}}} + \frac{0.054}{1 + \frac{1.1E \cos\theta^*}{850 \text{ GeV}}} \right), \quad (1.4)$$

where

$$\cos\theta^* = \sqrt{\frac{0.010521 + \cos^2\theta - 0.068287 \cos^{0.958633}\theta + 0.0407253 \cos^{0.817285}\theta}{1 + 0.010521 - 0.068287 + 0.0407253}}. \quad (1.5)$$

There are several physics principles behind this distribution. The power law dependence on the muon energy $E^{-2.7}$ follows from that in Eq. (1.1) of the primary cosmic rays, since cosmic muons are secondaries originated from the primary rays.

The rightmost multiplication factor represents the QCD muon production factor shown in Eq. (1.2) and (1.3). The ratio 1 to 0.054 is the atmosphere

pion-kaon number ratio determined by the primary proton scattering branching ratio [19]. The 115 GeV and 850 GeV are the critical energies for pions and kaons at which their interaction lengths are equal to their decay lengths [21], hence their contributions to the surface muons are suppressed.

The $\cos \theta^*$ is the atmospheric attenuation factor at different incident zenith angles. It is a fitted function inversely proportional to the track length, while taking into account the curvature of the Earth. If the Earth is flat, $\cos \theta^*$ is reduced to $\cos \theta$. Muons coming from a large zenith angle have to travel a longer path length of air from their production height to the ground, which implies a greater number density attenuation by scattering, energy dissipation and decay. Hence, the cosmic muon flux decreases as the observation zenith angle (θ) increases.

Since our detector is insensitive to the muon energy, we are more interested in the energy-integrated flux as a function of the zenith angle in Fig. 1.3. It is

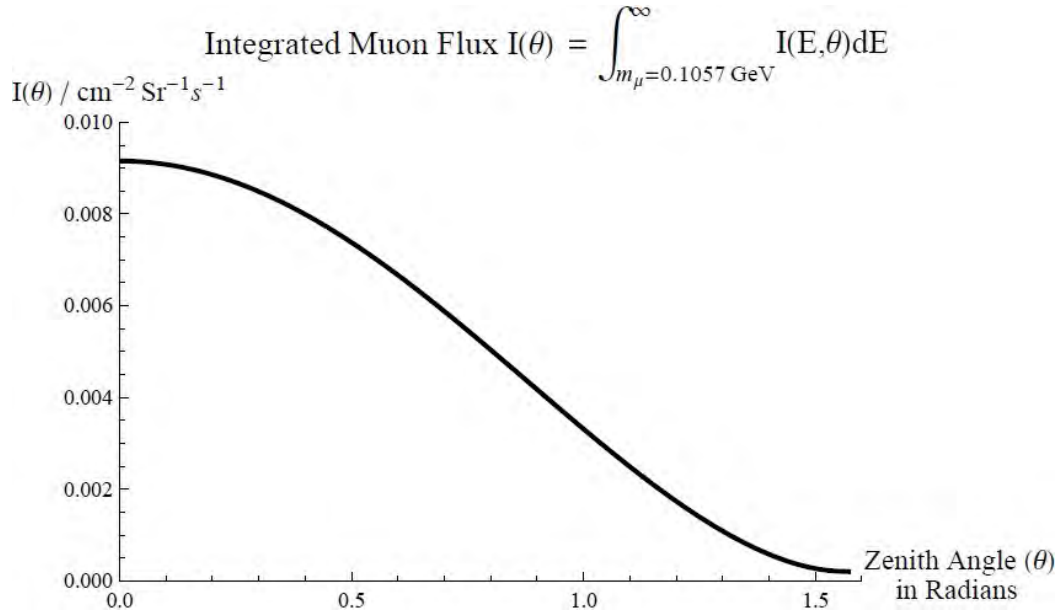


Figure 1.3: The surface cosmic muon flux by integrating over the muon energy in the modified Gaisser parameterization in Eq. (1.4) as a function of zenith angle.

important to understand the physics behind this distribution, as this zenith angle dependence will be convolved in the cosmic muon east-west ratio that we wish to

simulate and measure in the next section.

1.2.2 Cosmic Muon East-to-West Ratio

Apart from the zenith angle dependence, there is also a high order azimuthal angle (ϕ) dependence on the surface observation of the cosmic muon flux distribution in the celestial sphere. The cosmic muon flux varies at about 10% in different directions, with the greatest difference between the east and west. In general, the cosmic muon flux coming from the west is greater than that coming from the east. It is thus called the east-west (E/W) effect.

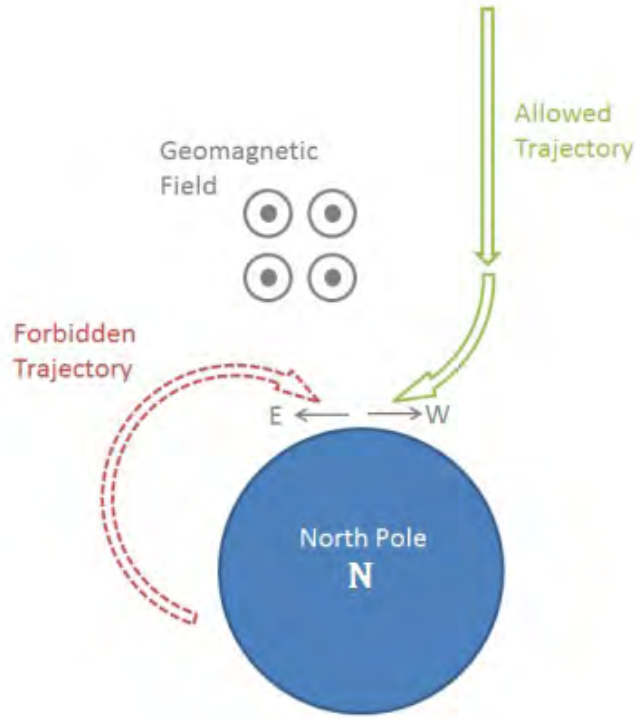


Figure 1.4: An illustration of the east-west effect seen from above Earth's north pole. More eastward tracks of the primary cosmic rays are allowed than westward tracks. The graph is taken from [22].

The east-west asymmetry is due to the positive charged primary cosmic rays propagating through the geomagnetic field. Some originally westward muon

tracks are bent to become eastward tracks, while some originally eastward tracks become forbidden. The net effect is a greater muon flux coming from the west than that coming from the east.

We expect the east-west flux ratio to be a function of muon energies and zenith angles. Higher energy primary rays have larger radii of curvature in the geomagnetic field and are less subjected to the E/W effect. However, low energy muons are stopped by atmospheric attenuation at large zenith angles. Therefore, the two effects combined makes the E/W effect less apparent for large zenith angles. In Section 1.4, we use a Monte-Carlo (MC) simulation to produce muon samples for our detector simulation.

1.3 The CUHK Muon Telescope

In this experiment, we determine the east-west cosmic muon asymmetry ratio of the cosmic muon flux. We verify that the asymmetric of cosmic muon flux is primarily due to the magnetic field above the Earth by confirming our measurement result with a computer simulation. We also want to probe the magnitude variation of the east-west asymmetric effects in different zenith angle of the incoming cosmic muons.

We have assembled a detector, the CUHK Muon Telescope, or the muon telescope, to measure the various aspects of cosmic muons. It is a plastic scintillator-based detector. It has 12 scintillation strips organized in 4 hodoscopic layers. It is also capable of telescope-like locomotion. The 3-scintillators-per-layer configuration and tunable separation between the layers allows the muon telescope to measure the cosmic muons with variable angular resolution.

The muon telescope was operational since the year 2010. It has been taking cosmic muon data in different locations since. In the sets of runs from February 2013 to Summer 2014, the muon telescope was placed in a room on the roof of the Science Center North Block of the Chinese University of Hong Kong. One and a

half years of continuous data were taken to measure the cosmic muon east-west ratio.

The muon telescope is briefly introduced in the following sections. A more detailed description of the CUHK Muon Telescope hardware can be found in Tam's thesis [23].

1.3.1 Detection Mechanism

We use twelve 1-cm thick, $19.5\text{ cm} \times 60\text{ cm}$ by area, plastic scintillators to detect cosmic muons. The fast response of the plastic scintillators and PMTs provide an excellent timing resolution for muon tagging.

Hamamatsu H7826 [26] PMTs are connected to the plastic scintillators for photons collection. The anodes of the PMTs provide an over 10^6 multiplication factor for the signal photons. Light guides are used to connect the the scintillators to the 15 mm diameter PMT light windows. All the components are glued together with epoxy.

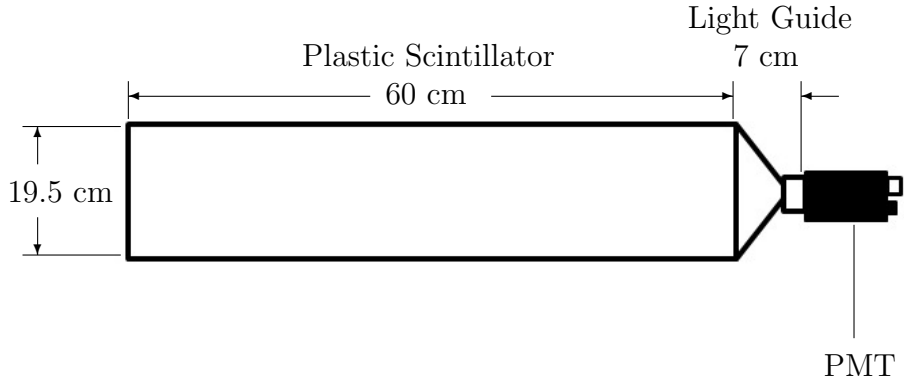


Figure 1.5: Diagram of a scintillation strip

The whole scintillator strip, except for the electrical input and signal output of the PMT, is wrapped to achieve light-tightness. The innermost layer of the wrapping is a piece of aluminum foil. The reflectivity of aluminum enhances the efficiency of light trapping. The second layer wrapping is black electrical tape to

absorb the light from the external environment. The third layer repeats the first layer wrapping using aluminum foil and the forth layer, with black electrical tape again. The four-layer wrappings ensure that no external light can leak into the PMT.

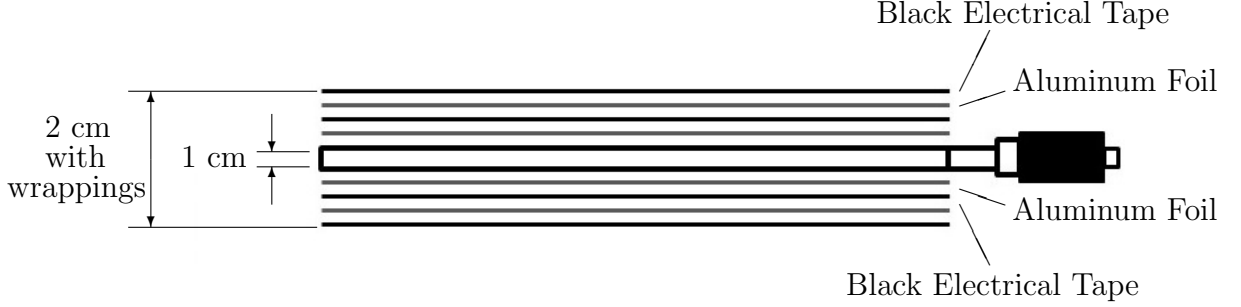


Figure 1.6: Another projection view of a scintillation strip showing the wrappings.

Custom-made front-ends are used to read out the PMT signals and set the PMT biases. Tasks such as threshold settings, front-end signals readings, coincidence and event packet forming, etc. are performed in a data acquisition system (DAQ) with a Spartan 3E XC3S1200E-FGG320D [24] Field Programmable Gate Array (FPGA) on a Digilent Nexys-2 board [25]. The DAQ supports at most 16 PMT channels, which means there are 4 spare channels given the 12 scintillation strips setup. The FPGA outputs data through an RS232 serial port to a Scientific Linux computer for data analysis.

1.3.2 Angular Resolution

The 12 scintillation strips are organized in 4 hodoscopic layers. On each layer, the 3 scintillator strips are put side-by-side parallelly. The 3 scintillator strips cover an area of $60 \text{ cm} \times 60 \text{ cm}$. The layer thickness including the wrappings is 2 cm. Each layer gives a coordinate along an axis on the x - y plane. The scintillation strips on two adjacent layers are perpendicular to each other. Two hodoscopic layers are put together to give a 3-by-3 (x, y) -coordinates, as in Fig. 1.7a. The

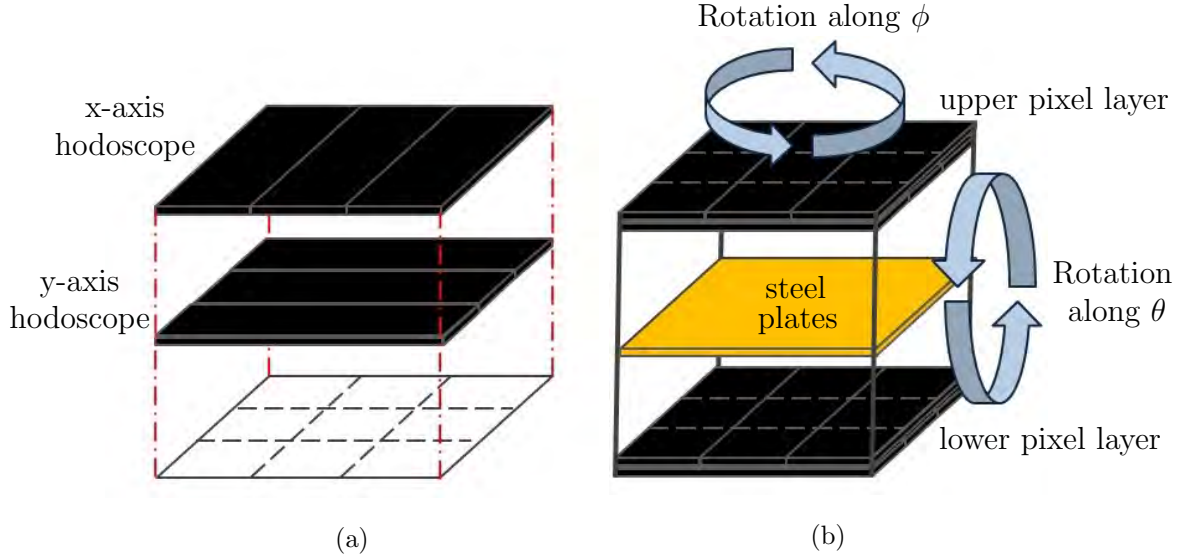


Figure 1.7: (a) demonstrates how two hodoscopes combined to one pixel layer. (b) shows the locomotion along the azimuthal and zenith angles.

9 (x, y) -pixels are grouped together as a single pixel layer. The muon telescope thus has two pixel layers in total.

A muon is recognized by a 4-fold coincidence of the 4 hodoscopic layers. The two pixel layers allow us to have an angular resolution of the muon flux on the θ - ϕ plane of the celestial sphere. The two pixel layers are separated by four steel plates, each 0.5 cm thick, for shielding background radiations. The separation between the two pixels layers are adjustable within a range from 24 cm to 150 cm. It assists the muon telescope to look at different patches of the sky. Adjusting the separation also gives additional muon angular resolution through looking at the same patch of sky with different angular differential acceptances.

The muon telescope detects muon fluxes from different patches of the sky by using different “combos” of pixels, shown in Fig. 1.8. The combos are formed by the 4-fold coincidences of the 2 pixel layers. Classified by the regions the combos looks at in the θ - ϕ plane, there are 25 types of distinct combos among the 81 two-pixel combinations. Except for the vertical combos (Fig. 1.8a), all the other 24 types of combos have four-fold ϕ -rotational symmetry. We factor out the four

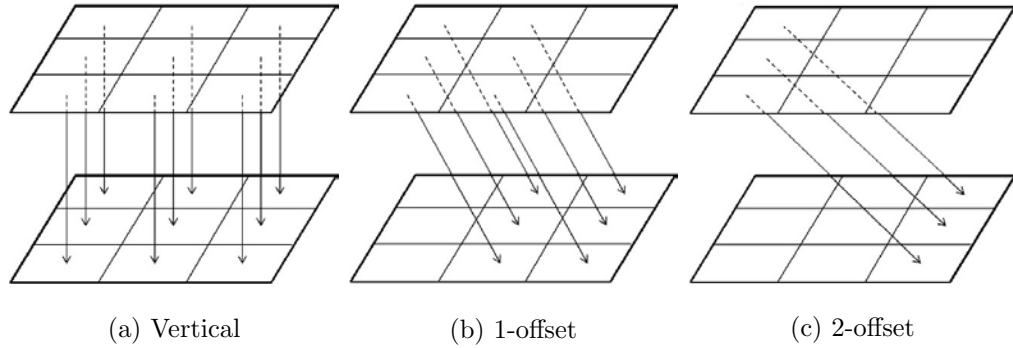
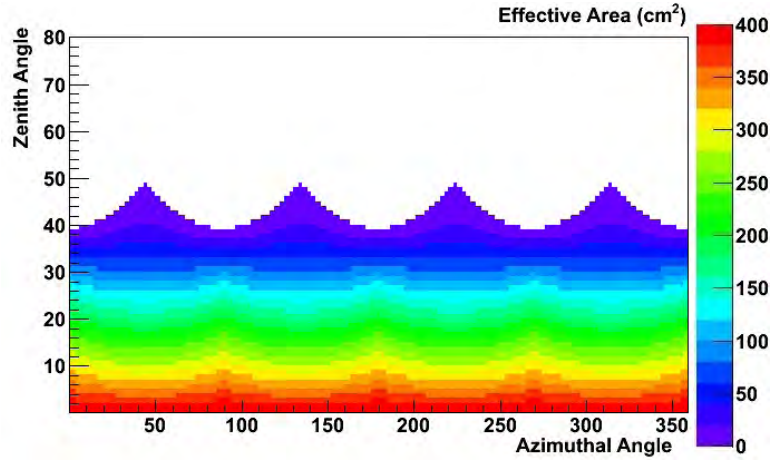


Figure 1.8: The three classes of combos used in the analysis. Figures taken from Ref. [23].

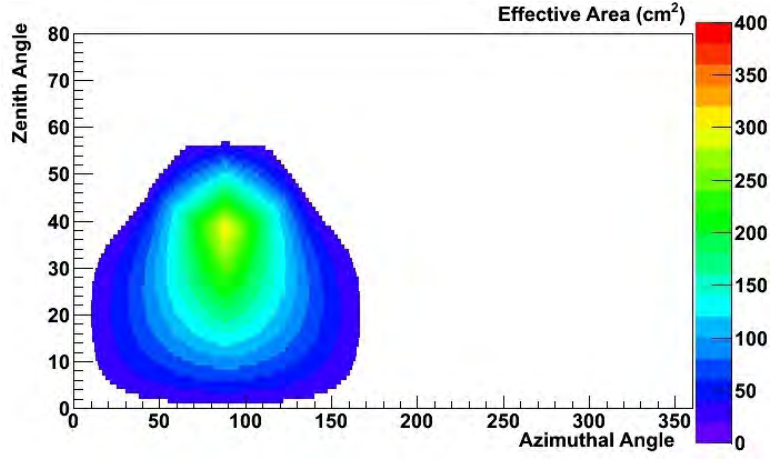
rotational symmetries (the north, east, south and west) to define 6 classes of combos, among which the 1-offset combos (Fig. 1.8b) and 2-offset combos are used (Fig. 1.8c) to measure the E/W effect. In short, three classes of combos are used: 9 vertical combos, 4×6 1-offset combos and 4×3 2-offset combos.

In the (θ, ϕ) regions of finite acceptance seen by the combos, the detector's effective areas are the overlapping areas of the two pixels (in different layers) seen from a certain coordinates θ and ϕ . The effective area function $A(\theta, \phi)$ can be calculated analytically by trigonometric projection. The results for the vertical and east combos are drawn in Fig. 1.9 for 24 cm separation and Fig. 1.10 for 40 cm separation. The effective areas of the corresponding south, west and north can be acquired by simply right-translating the east combo patterns along ϕ by 90° , 180° and 270° respectively. Obviously, all combos of the same type (e.g. each of the 9 vertical combos) have exactly the same effective area functions.

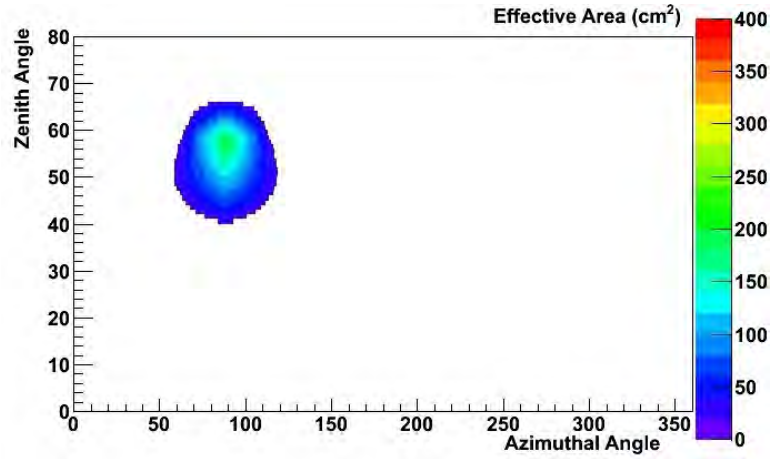
In general, the effective areas of the combos cluster towards small zenith angle θ when the pixel layers separation is large. They cluster towards large θ when the separation is small. This means that we can measure the cosmic muon flux, thus the E/W effect, as a function of θ by tuning the separation. It should be noted that a large separation also means small integrated effective areas of the combos, which implies a lower count, thus a longer data-taking period for the same statistics as those in a small separation configuration.



(a) Vertical

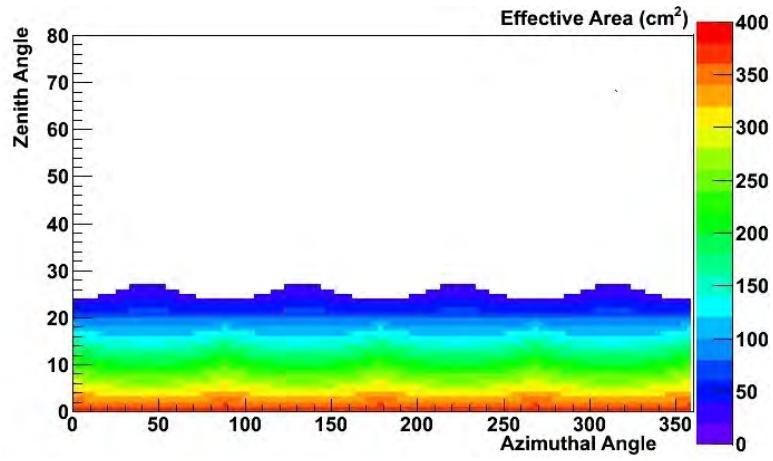


(b) East 1-offset

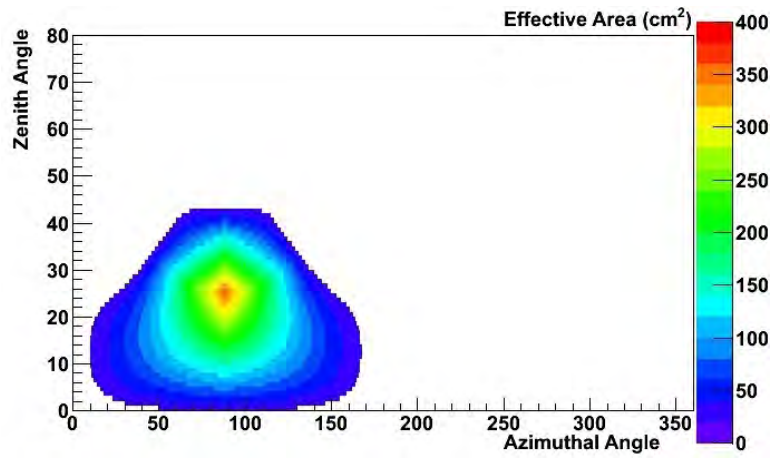


(c) East 2-offset

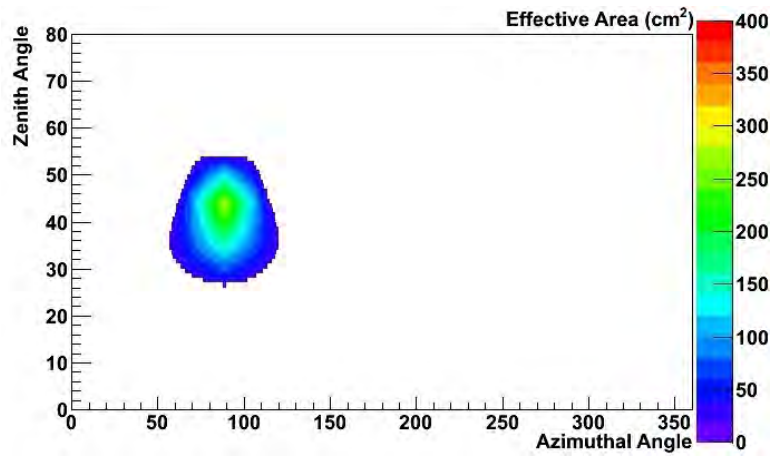
Figure 1.9: The effective areas $A(\theta, \phi)$ of the vertical and east combos with 24 cm pixel layer separation.



(a) Vertical



(b) East 1-offset



(c) East 2-offset

Figure 1.10: Same as Fig. 1.9, but for 40 cm pixel layer separation.

Apart from the separation tuning, another way to look into the different patches of the sky is to point the whole muon telescope into those directions. Two stepping motors controlled by the DAQ can turn the muon telescope in the zenith angle and azimuthal angle (Fig. 1.7b). The zenith turning measurement is not used in the analysis of this thesis, but the azimuthal turning is essential for the measurement of the E/W effect.

1.3.3 Detector Location

The muon telescope is located on the roof of the Science Center North Block of the CUHK, which is at 22.42°N , 114.21°E and 120 m above the sea level. A small building on the roof provides the muon telescope with a location of small overhead shielding and a relatively stable environment against wind, rain and sunlight.

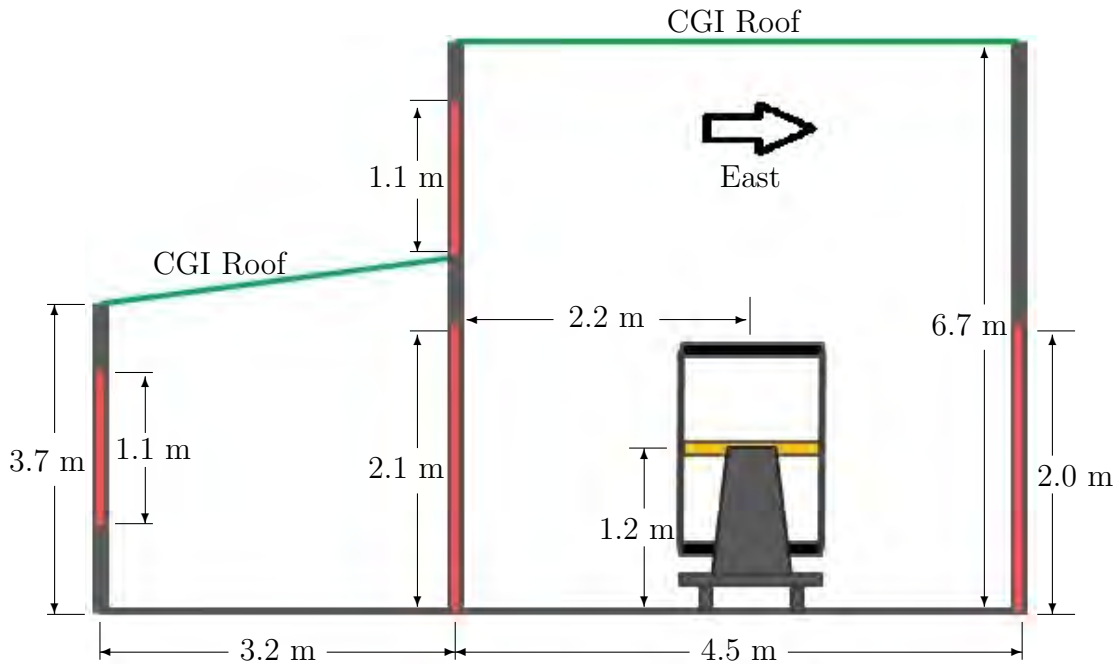


Figure 1.11: A view of the roof building from the south. The width dimension not shown in this figure is 4.5 m for the big room and 3.0 m for the small room.

Although the building is a place with the minimum shielding, some concrete structures may still block some of the cosmic muons. The building is surrounded by 15 cm thick concrete walls. There are two rooms in the building (Fig. 1.11). The muon telescope is located in the bigger room. There is one window in the small room and one sky window near the roof of the big room, and two doors, one connecting the big room to the outside and one connecting the big room to

the small room. The ceiling is made of corrugated galvanized iron (CGI), which has negligible effect on cosmic muons.

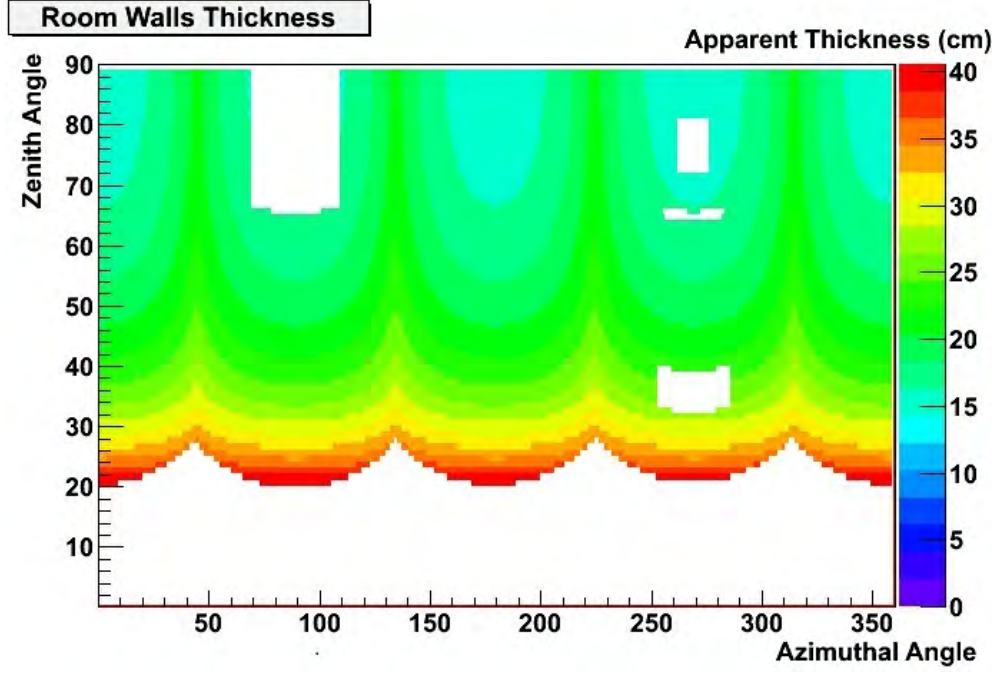


Figure 1.12: The concrete structure thickness map seen by the muon telescope in the θ - ϕ plane.

The concrete structures seen by the muon telescope can be projected onto the θ - ϕ plane in Fig. 1.12. The apparent wall is thicker at a large inclination view point due to a $(\cos \theta)^{-1}$ factor. We can estimate the effect of the shielding by applying this wall map to the simulated cosmic muon map.

1.4 Cosmic Muon Simulation

1.4.1 Cosmic Muon Data Set

We want to verify that a computer model with two elements: the magnetic field map above the Earth and the Earth's atmosphere, can adequately explain the cosmic muon east-west asymmetry.

We want a realistic description of the E/W effect in Hong Kong. Therefore, we use a cosmic ray Monte-Carlo (MC) data set produced by Yat Long Chan, the simulation detail can be found in his thesis [22]. The data set contains 10^6 surface cosmic ray particles, among those 7.6×10^5 are muons. The distribution of cosmic muons in the sample is plotted in Fig. 1.13.

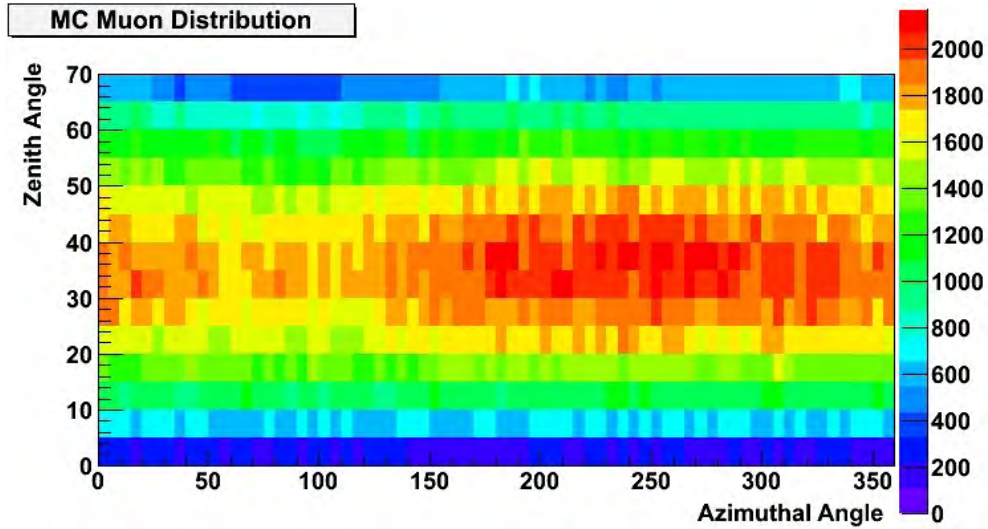


Figure 1.13: Cosmic muon MC sample distribution on θ - ϕ plane of the celestial sphere in degrees by Chan [22].

The cosmic ray simulation is carried out in two steps. The first step is to simulate the primary cosmic ray particle arrival at Earth's upper atmosphere. The primary particles, defined to be protons isotropically distributed according to Eq. (1.1), are propagated from 100 km above the Earth surface away from the Earth. The magnetic field model used in the simulation are the combination of the IGRF-11 geomagnetic field model [27] and Tsyganenko-02 model [28] on the interplanetary magnetic field. Particle tracks that can reach 25 Earth radii away from the Earth surface are tagged as possible incoming cosmic ray tracks by time-reversal symmetry. This simulation produces a detailed muon map that includes the cutoff rigidity effect in Fig. 1.2.

The possible incoming tracks in the above simulation are the input primary

particles for the second simulation step, which is to simulate the cosmic muon production and propagation in Earth's atmosphere. Geant4 [29] is used to simulate the interactions between the cosmic rays and air molecules. The air density is crucial to the interaction rate of the cosmic ray. The Earth's atmospheric density is modeled in two parts. The 0 km - 47 km air column is modeled using the European Centre for Medium-Range Weather Forecasts' ERA interim data [30], while the 47 km - 100 km air column uses the NRLMSISE00 model [31].

After the second step, the muon map generated (Fig. 1.13) is the surface cosmic muon we want to investigate. The muon map can be subjected to the acceptance simulation of the muon telescope. The result is used to predict the E/W effect.

1.4.2 East-west Muon Flux Asymmetry Simulation

We consider a muon flux I of energy E on the position (x,y) from the direction (θ,ϕ) . The energy-independent acceptance of a certain combo c of the muon telescope is $a_c(\theta, \phi, x, y)$. The muon counts can be represented by

$$\begin{aligned} \int dN &= \int_{\Omega} \int_{\text{area}} \int_E I(\theta, \phi, x, y, E) a_c(\theta, \phi, x, y) d\theta d\phi dy dx dE \\ &= \int_{\Omega} \left[\int_0^{\infty} I(\theta, \phi, E) dE \right] A_c(\theta, \phi) d\theta d\phi . \end{aligned} \quad (1.6)$$

The integral over the pixel area is carried out if we assume that the muon flux is homogeneous at different points of space. The area of our muon telescope pixels is small enough for this assumption to hold true. A_c is the effective area we calculated for different combos in Fig. 1.9 and Fig. 1.10.

If Earth and its surroundings are without magnetic field, the flux I can be approximated by Eq. 1.4, and its energy integral is in Fig. 1.3. For the actual flux distribution used in the following simulation, we take Chan's muon map in Fig. 1.13, which includes the effects of the magnetic field .

We take care of the attenuation effect of the concrete walls surrounding the muon telescope by setting an energy cut at the corresponding θ - ϕ region. We cal-

culate the stopping energy for each effective wall thickness using the continuous-slowing-down-approximation (CSDA) stopping distances in Ref. [32]. The stopping energy map is in Fig. 1.14.

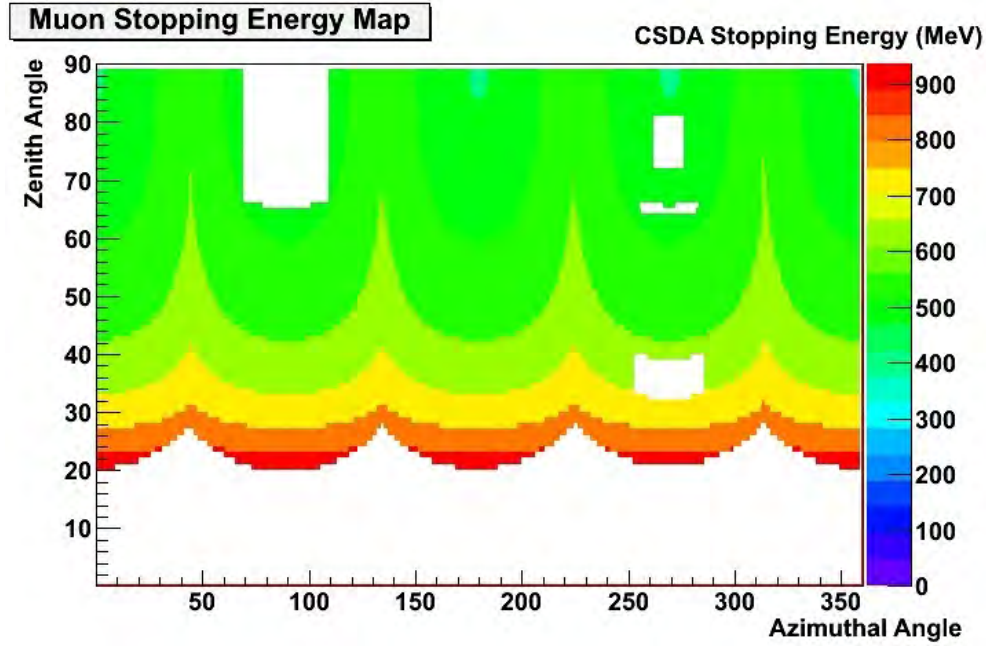


Figure 1.14: The muon stopping energy map translated from the concrete wall map in Fig. 1.12.

The east combo counts and the west combo counts can be determined by multiplying the muon map (Fig. 1.13) to the acceptance (Fig. 1.9, Fig. 1.10) and applying the walls energy cut (Fig. 1.14). By dividing the east counts by the west counts, the E/W effect measured by each combo can be determined. We have done the calculation for 24 cm, 32 cm and 40 cm pixel layers separations. The results for the E/W effect of 1-offset combos and 2-offset combos are shown in Fig. 1.15. The E/W ratios are approximately 10% for 1-offset and 14% for 2-offset.

The error bars of the simulation data points are set by the statistics of the detector accepted MC muon numbers and a ± 2 cm systematic uncertainty of the pixel layers separation due to the thickness of the scintillation strips. Between the two, the statistics dominate the errors.

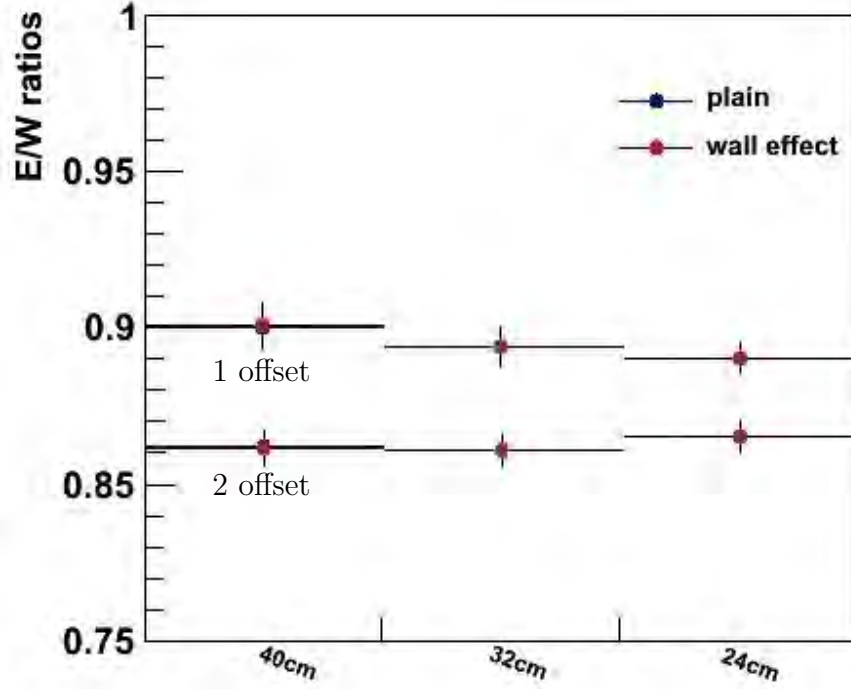
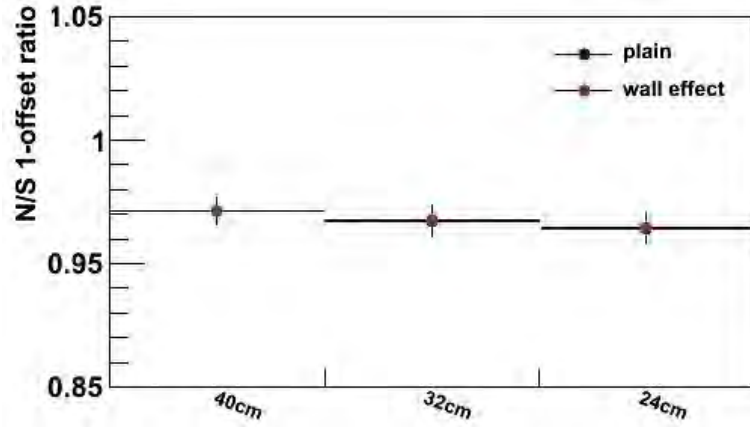


Figure 1.15: The predicted east-west ratio seen by the muon telescope. The blue dots are calculated assuming no surrounding walls, whereas the red dots simulate also the walls.

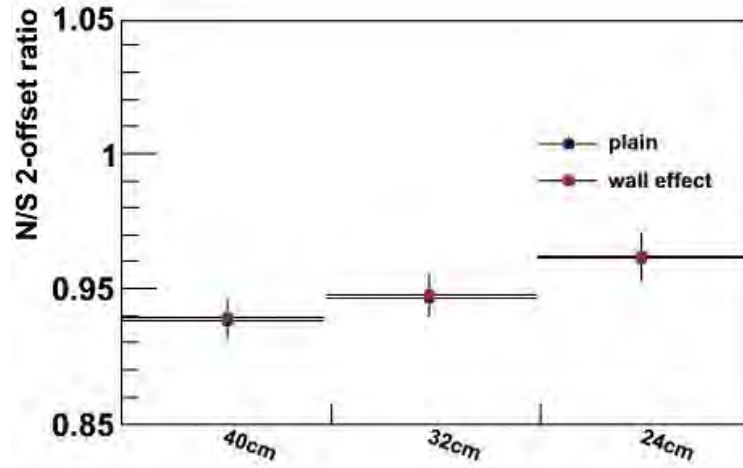
We also compare the result with the concrete wall cutoff effect (red dots) and without the concrete wall cutoff effect (blue dots) in Fig. 1.15. It is demonstrated that the walls surrounding the muon telescope have insignificant effects on the east-west ratio measurements.

The low energy muons can be ill-defined due to the uncertainties of the exact atmosphere column height and the low-energy scattering processes. We vary the low energy muon numbers to test the E/W effect dependence on the low energy counts. We apply a weight w to muons with energy $< E_{\text{cut}}$ and re-simulate the muon counts.

For $E_{\text{cut}} = 500$ MeV and $w = 1.2$ and 0.8 , the changes of the E/W ratio are $\delta(N_E/N_W) = 2.5\%$ and 3.3% respectively. Similarly for $E_{\text{cut}} = 200$ MeV and $w = 1.5$ and 0.5 , $\delta(N_E/N_W) = 1.6\%$ and 0.7% respectively. The E/W effect is



(a) 1-offset N/S effect



(b) 2-offset N/S effect

Figure 1.16: Same as Fig. 1.15, but for the north-south muon flux ratio.

not very sensitive to the low energy muon counts.

We also study the north-to-south muon flux ratio with the same method. We expect that there is a north-south effect, just like the east-west effect, except with a smaller magnitude. It is because the higher multipole moments of the magnetic field break the north-south symmetry. The effect enters the simulation through the non-dipolar geomagnetic field model and the external magnetic field.

The N/S ratio is shown in Fig. 1.16. We have simulated the results both with and without the concrete wall cutoff energy. Their differences are insignificant,

like the E/W effect. The N/S effects are about 97% for 1-offset and range from 94% to 96% for 2-offset.

To test for the statistical robustness of the E/W and N/S effects from the Monte-Carlo generator, we employ the Jackknife statistical test on the MC cosmic ray data set containing $N = 10^6$ cosmic ray particles. We have divided the data into n parts such that each data part contains $N \times (n-1)/n$ cosmic ray particles. In the k th part of data, we have left out N/n particles labeled from $N - kN/n$ to $N - (k+1)N/n$, where k runs from 0 to $n-1$.

		n = 10		n = 100	
Combos		$\bar{\theta}_J$	σ_J/N	$\bar{\theta}_J$	σ_J/N
s = 24 cm	EW 1-offset	0.891	5.3×10^{-3}	0.891	5.3×10^{-3}
	EW 2-offset	0.86	1.0×10^{-2}	0.85	1.1×10^{-2}
	NS 1-offset	0.964	3.4×10^{-3}	0.964	4.7×10^{-3}
	NS 2-offset	0.959	8.6×10^{-3}	0.95	1.0×10^{-2}
s = 32 cm	EW 1-offset	0.895	6.1×10^{-3}	0.894	6.1×10^{-3}
	EW 2-offset	0.86	1.1×10^{-2}	0.86	1.0×10^{-2}
	NS 1-offset	0.967	4.0×10^{-3}	0.967	5.7×10^{-3}
	NS 2-offset	0.946	8.1×10^{-3}	0.952	9.1×10^{-3}
s = 40 cm	EW 1-offset	0.902	6.8×10^{-3}	0.902	6.9×10^{-3}
	EW 2-offset	0.86	1.1×10^{-2}	0.86	1.1×10^{-2}
	NS 1-offset	0.971	4.6×10^{-3}	0.971	6.7×10^{-3}
	NS 2-offset	0.940	7.6×10^{-3}	0.937	9.4×10^{-3}

Table 1.1: A comparison, as a function of the layer separation (s) and combos, of the Jackknife mean $\bar{\theta}_J$ and error σ_J with re-samplings $n = 10$ against those of $n = 100$.

Suppose $\bar{\theta}$ is the average value of an observable (e.g. the E/W ratio) of the

whole data set of N particles, the k th data part has an average value θ_k for that observable. We evaluate the Jackknife re-sampling variance

$$\sigma_J^2 = \frac{n-1}{n} \sum_{k=0}^{n-1} (\theta_i - \bar{\theta}_J)^2 \quad (1.7)$$

and the Jackknife bias

$$B_J = (n-1)(\bar{\theta}_J - \bar{\theta}) , \quad (1.8)$$

where $\bar{\theta}_J$ is the Jackknife average

$$\bar{\theta}_J = \frac{1}{n} \sum_{k=0}^{n-1} \theta_k , \quad (1.9)$$

for the MC data distribution to see if the result agrees with the simplest and most natural model: the normal distribution.

We carry out two re-sampling with $n = 10$ and $n = 100$ respectively. The result is shown in Table 1.1. The Jackknife averages $\bar{\theta}_J$ and the Jackknife errors σ_J are with both resampling sizes, which implies that the fluctuations of the E/W and N/S effects from our MC muon data are well-described by the normal distribution.

We have also calculated the Jackknife estimator biases (B_J) for the MC data distribution. The biases for the 1-offset ratios are 7×10^{-6} and those for the 2-offset ratios are 1.5×10^{-5} . The estimator biases are negligible compared to the statistical error bars.

The Jackknife analysis demonstrates the random nature of the Monte-Carlo generator and the physics simulation. The fluctuations of the resulting observables can be modeled by normal distribution. The result rules out any statistical quaintness of the cosmic ray MC data set.

Chapter 2

Measurement-Simulation Comparison

2.1 Methods

We measure the cosmic ray muons using the CUHK Muon Telescope. Our cosmic muon selection criteria are a 4-fold coincidence among the 12 PMTs of the detector, of which each hodoscopic layer must have at least 1 signal.

The 4-fold coincidence provides a basic background rejection. The average singles rate of the PMTs is 1 kHz. Within a coincidence time window of 100 ns, the rate of 4-fold chance coincidences is $\sim 4^{-11}$ Hz (or once every 790 years). Hence, our main background is ambient radiation. We have put 2 cm of steel between the two pixel layers to further reduce the beta and gamma radiation coincidence rates.

Moreover, the 4-fold coincidence setting implies at least one pixel from each of the 2 pixel layers must light up in a muon event. The two-pixel coincidences enable us to fit simple straight muon tracks. Depending on the types of pixel coincidences, i.e. combos in Fig. 1.8, we can identify the patch of the sky from which the muon comes.

We use the vertical, 1-offset and 2-offset combos of the 12 PMTs to measure

the E/W effects at different zenith angles. For example, the vertical combo is pointing towards $\theta = 0^\circ$. The 1-offset combos are roughly pointing at $\theta = 40^\circ$, 32° and 26° for pixel layer separations $s = 24$ cm, 32 cm and 40 cm respectively. Similarly for 2-offset, $\theta = 60^\circ$, 51° and 45° for $s = 24$ cm, 32 cm and 40 cm.

Because of the large pixel size, each combo does not sharply represent a particular angular direction. In fact, every combo subtends a large solid angle spanning over dozens degrees of zenith angle, with an effective weight at each (θ, ϕ) -coordinates described by Fig. 1.9, Fig. 1.10, etc. The weighted coverage map is called the acceptance $A_c(\theta, \phi)$ of a particular combo c .

Another factor to consider is the efficiency of each scintillation strip. Even for the same type of combos, the event rates can vary hugely because of the ranging efficiencies of the plastic scintillators and PMTs. Some factors which contribute to the efficiencies are, for instance, the distance between the pixel and the PMTs, the clarity of the plastic scintillator and the properties of the PMT electronics. We assign the efficiency of combo c to be ϵ_c .

We can express the c combo count N_c , under a cosmic muon flux $I(\theta, \phi, E)$, as

$$N_c = \int_{\Omega} \epsilon_c A_c(\theta, \phi) \left[\int_0^\infty I(\theta, \phi, E) dE \right] d\theta d\phi . \quad (2.1)$$

The equation is very similar to Eq. (1.6), except that there is an unknown efficiency factor ϵ_c for each combo c .

While the acceptance is studied well enough in the simulation, the efficiencies of the combos are not easily deducible. Since the E/W effect is a relative measurement, we hope to cancel out the efficiency factors in

$$\text{E/W ratio} = \frac{\epsilon_i N_E}{\epsilon_j N_W} . \quad (2.2)$$

The efficiency factor ϵ_i/ϵ_j is guaranteed to be unity if $i = j$ exactly. This may be achievable by some combination of measurements with a total efficiencies $\sum_c \epsilon_c = \epsilon_i = \epsilon_j$. We show that this can be done by rotating the muon telescope along the azimuthal axis during data-taking.

In each measurement run, we take a total of 4 sets of data. We measure the directional muon flux using the 1-offset and 2-offset combos in the sets of measurement. Between two sets of data, the muon telescope is rotated 90° along azimuthal axis in a clockwise or anticlockwise direction. The east combos in the previous set become the south combos of the new set, and similarly for the other 3 directional combos. A new set of data is taken in this configuration.

In the whole run, the muon telescope rotates 3 times in a consistent direction such that every directional combo samples all 4 geographical directions for a constant period of time. The results of the 4 sets of data are sorted by their geographical directions and are summed together to get the E/W and N/S ratios of the entire run.

We write the combined efficiency for the set 1 east combos (the sum of either 1-offset or 2-offset combo efficiencies) as ϵ_E , and similarly for the other three directions ϵ_W , ϵ_S and ϵ_N . The combined E/W effect of the whole run is

$$\begin{aligned} \text{E/W ratio} &= \frac{(\epsilon_E + \epsilon_S + \epsilon_W + \epsilon_N)N_E}{(\epsilon_W + \epsilon_N + \epsilon_E + \epsilon_S)N_W} \\ &= \frac{N_E}{N_W}. \end{aligned} \tag{2.3}$$

The detector efficiencies cancel out each other. The remaining counts N_E and N_S only include factors from the calculable combo acceptances and the physical muon flux distribution. All instrumentation effects are removed from the ratio result. The same cancellation also takes place in the N/S ratio measurements.

In the actual measurements, the time duration of each run ranges from at most 2 weeks to at least 4 days. We choose a short time duration for each run because the cosmic muon asymmetric effects can be time-dependent and the instrumentation quality can also shift over time. A statistical significant time-dependence of any of the factors in Eq. (2.1) will destroy the exact cancellation in Eq. (2.3). Nonetheless, we expect that the muon flux asymmetry and instrumentation time-dependences have long time scale. A run of 2-week timescale should satisfy the criteria for Eq. (2.3) to hold true.

We also normalize the combo count rates with respect to the total 4-fold count rates to further reduce any time-dependence. We expect the muon flux to fluctuate in time due to the solar, geomagnetic and atmospheric conditions. To avoid the fluctuations of the total flux affecting the result, we divide the directional combo count rates by the total 4-fold count rates to remove this time-dependence. Hence, the count rates N_{dir} in Eq. (2.2) and Eq. (2.3) are actually

$$\bar{N}_{\text{dir}} = \sum_i \frac{N_{\text{dir}}(t_i)}{N_{\text{4-fold}}(t_i)} . \quad (2.4)$$

The E/W effect and N/S effect calculated from \bar{N}_{dir} should approximately be constants of time, unless there is some hidden physics that makes the asymmetric effects themselves depending heavily on time.

A detailed analysis of the statistical methods and data quality monitoring can be found in Kwok's thesis.

2.2 Measurement Results

The measurement is carried out on the roof building of the Science Center North of the Chinese University of Hong Kong. Throughout the period from February 2013 to May 2014, we have taken 16 runs. There are 2 runs with 40 cm separation, 3 runs with 24 cm separation and 11 runs with 32 cm separation. The time-series of the 4-fold coincidence counts in Fig. 2.1 demonstrates the run history of the E/W effect measurement.

We have detected over 4.5×10^7 candidate cosmic muons in the whole experiment. We have an approximately continuous 4-fold count time-series, except for two shutdown periods, when maintenance and detector tests are carried out, and a PMT front-end biases tuning, which causes the data to drop at that point.

11 of the 12 PMTs perform properly throughout the whole measurement. Their count rates drop slowly over the 1.5 years due to the aging of epoxy glue on the scintillators. The epoxy degrades from transparent to yellowish. Thus the

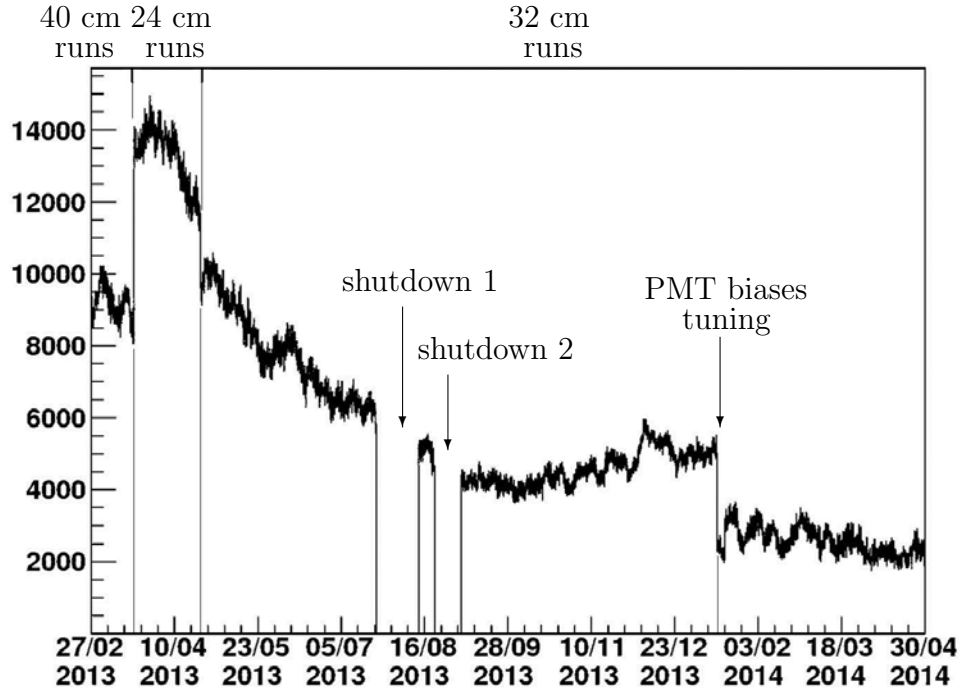
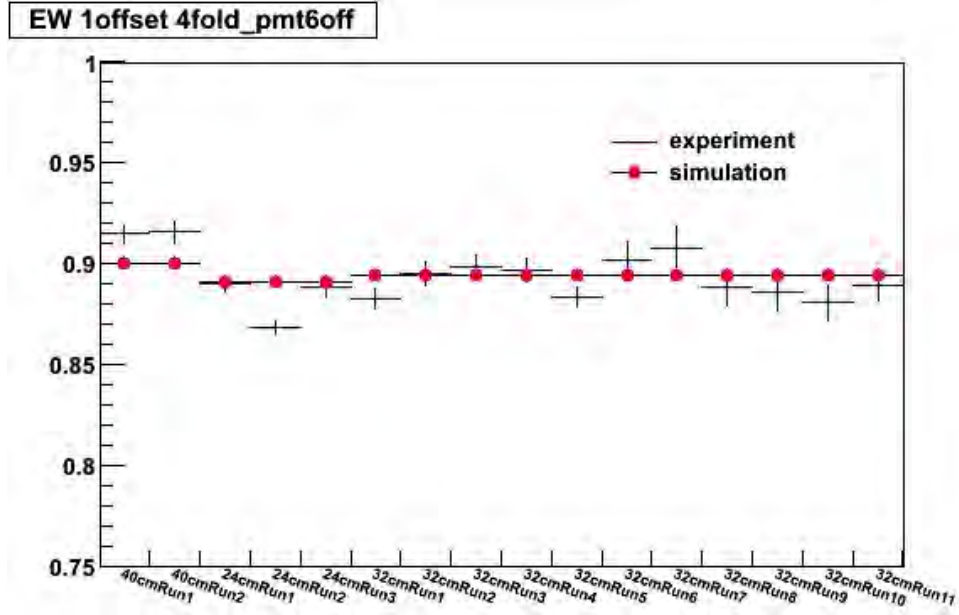


Figure 2.1: Cosmic muon 4-fold counts time-series over the data-taking period.

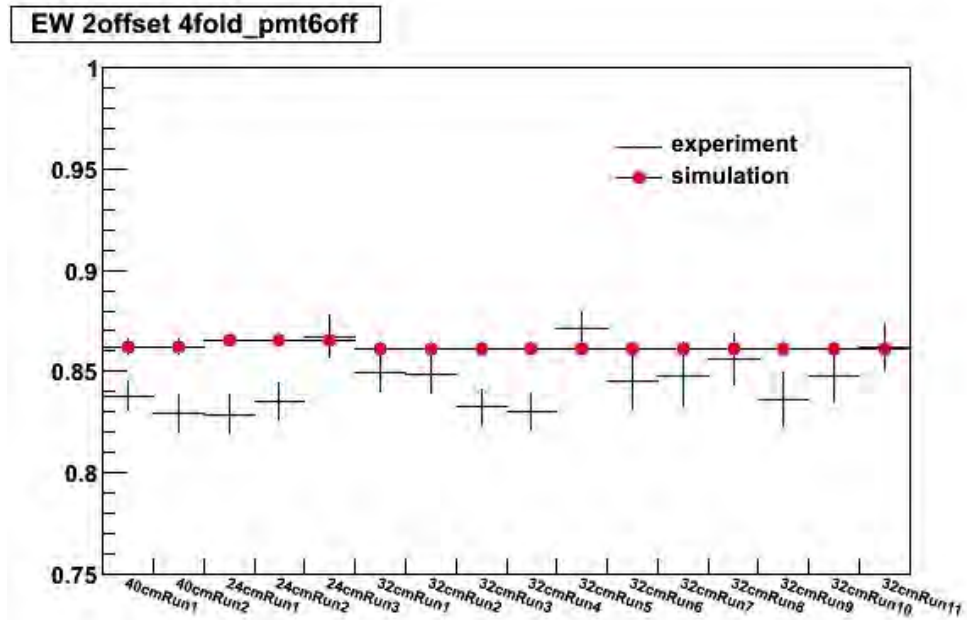
light transmittance from the scintillator to the PMT decreases, and the count rate decreases. The drop of count rates does not contribute to the E/W effect as our experiment method has eliminated the long-term efficiency dependence.

PMT 6, located at the third hodoscope counting from the muon telescope's top, has a very significant count rate fluctuations compared to the other PMTs in the 32 cm runs. We identify it as an internal failure of the PMT electronics. Therefore, PMT 6 is removed from the analysis in the 32 cm runs.

The results for the E/W effect compared to the simulation are shown in Fig. 2.2. The same for the N/S effect is in Fig. 2.3.

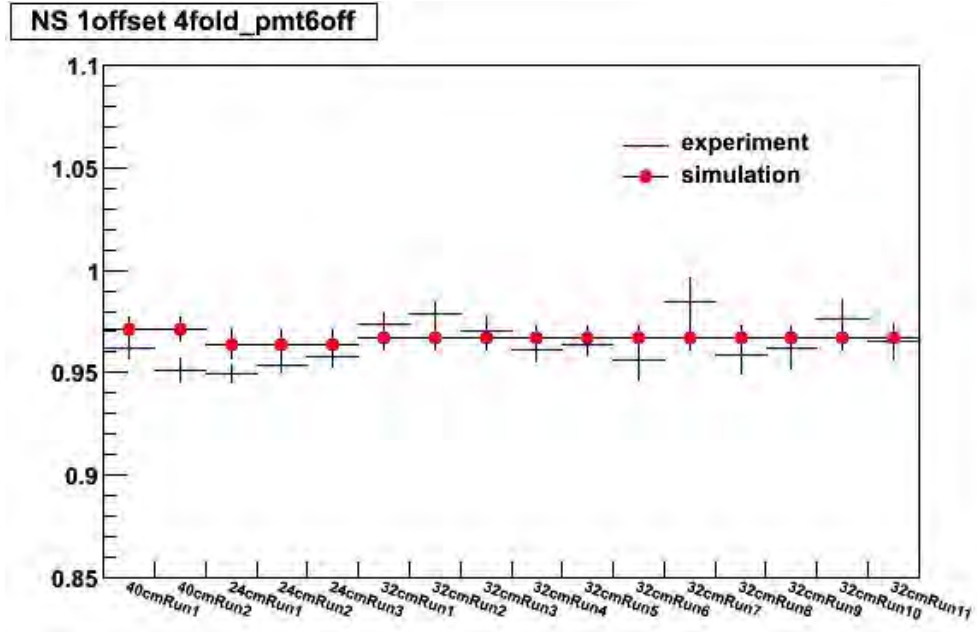


(a) 1-offset E/W effect result

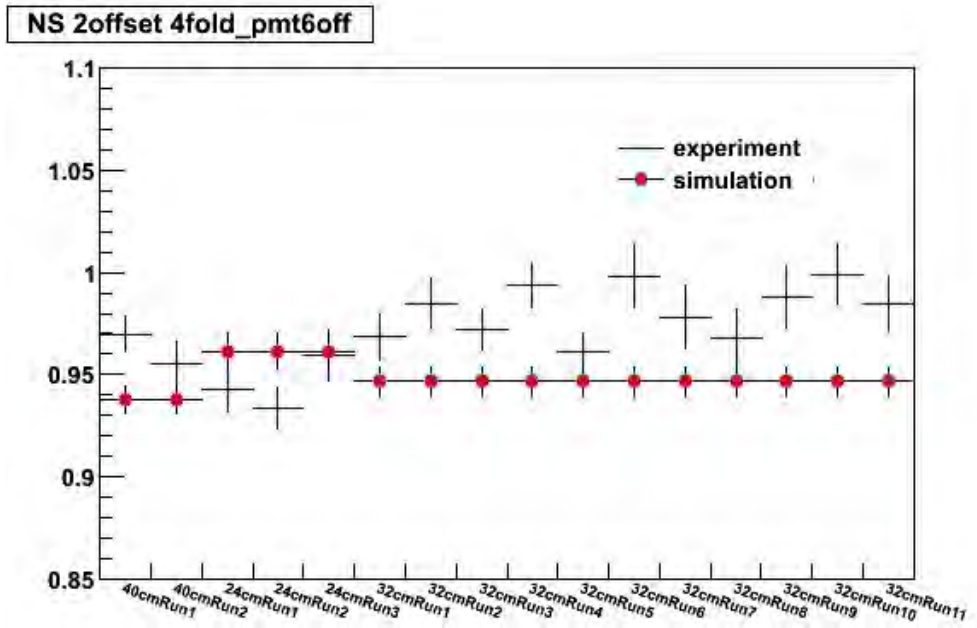


(b) 2-offset E/W effect result

Figure 2.2: Prediction-measurement comparison of the E/W effect.



(a) 1-offset N/S effect result



(b) 2-offset N/S effect result

Figure 2.3: Prediction-measurement comparison of the N/S effect.

2.3 Conclusion

The measurement data are self-consistent as most of the data points in one separation setting lie within 1σ of their mean values. The data points that lie farther away from the mean values can be postulated as a physical fluctuation of the directional asymmetric effects. One explanation is that there is a time-dependent change of the muon flux that is not entirely canceled out when we rotate the muon telescope.

We have taken average for the runs with the same layer separation in Appendix A. All of the ratio measurement data points are consistent with those of the simulation within 1.5σ . The measurements that deviate more than 1σ from the simulation are the east-west 24 cm 2-offset, north-south 24 cm 1-offset, the north-south 32 cm 2-offset and all of the 40 cm results.

The 40 cm measurement does not agree with the simulation data very well. This encourages us to consider a more detailed model on the primary cosmic rays particle distributions and magnetic field models. For example, a model that incorporates real-time solar wind and magnetic field data from the NASA Solar and Heliospheric Observatory (SOHO) can be a neat addition.

Yet, it should be noted that our understandings of the surface cosmic ray distribution are limited by our coarse-grained understandings of the atmospheric column and geomagnetic field above us. These two factors, which often vary with time and are hard to monitor in great detail, may hamper further efforts to model and simulate the surface cosmic ray distribution that fits the data better.

Lastly, the pixel layer separation method is not sensitive enough for distinguishing E/W effect at different zenith angles of the sky. We need to enhance the muon telescope spatial resolution to effectively measure small muon flux differences as a function of the zenith angles. This requirement motivates us to develop a multiwire proportional chamber to measure cosmic muons. Wire chambers are known for their high efficiency at detecting charged particles at high angular-

spatial resolution. With them mounted onto the muon telescope, we hope to produce a detailed muon sky map in the future.

Chapter 3

Wire Chamber Design

3.1 Introduction

We want to improve the measurement of cosmic muon with a new detector of high detection efficiency and background rejection ability. We also want to increase the detector's spatial resolution by one order-of-magnitude (from ~ 10 cm to ~ 1 cm), which is to improve the ability of the muon telescope to map out the muon flux from the sky.

The CUHK multi-wire proportional chamber (or CUHK wire chamber) is a detector that detects charged particles with ~ 1 cm spatial resolution. We have designed the wire chamber with the considerations of high and homogeneous efficiencies, cost, scalability and operation robustness. I will outline the chamber design and the detection mechanism in this introduction.

The basic design of a wire chamber is a row of charged anode sensing wires enclosed between two cathode planes. The sensing wires are connected to the front-ends. The wires are charged to 1.6 kV and the cathode planes are grounded. The potential difference sets up an electrostatic field within the wire chamber.

The chamber volume is gas-tight and is filled with P10 gas (90% argon, 10% methane). When a charged particle, such as a cosmic ray muon, traverses through the wire chamber, it deposits some energy in the P10 gas. The amount of energy

deposited in the gas per unit length is tabulated in Table 3.1.

$$\rho_{\text{Ar}} = 1.662 \times 10^{-3} \text{ g cm}^{-3}$$

Kinetic Energy (GeV)	Ionization (keV cm ⁻¹)	Total $\left \frac{dE}{dx} \right $ (keV cm ⁻¹)	CSDA stopping distance (km)
0.1	2.77	2.77	0.256
1	2.85	2.85	3.632
10	3.78	3.82	29.46
100	4.45	5.12	226.2

Table 3.1: Muon $\frac{dE}{dx}$ in gaseous argon at 1 atm, 20 °C. [32]

Typical cosmic muons easily pass through an 8 mm wire chamber, at the same time depositing enough energy to ionize many argon atoms. The electrons stripped off from the argon atoms rapidly drift towards the positively charged sensing wires, while the argon ions drift slowly towards the cathode panels.

As the electrons come close to a few diameters away from the wire, the drifting electrons gain enough kinetic energy to further ionize new argon atoms. An avalanche of secondary electrons produce a macroscopic currents of a few mA on the sensing wire. The current is then read out electronically by the front-ends.

The argon ions drift to the cathode panels and are neutralized by the electrons supplied from the cathode ground. In the first version of the CUHK wire chamber, we do not read out the signals from the positive ions. Nevertheless, we have left space in our design for the future implementation of ion signal read-out.

3.2 Structural Design

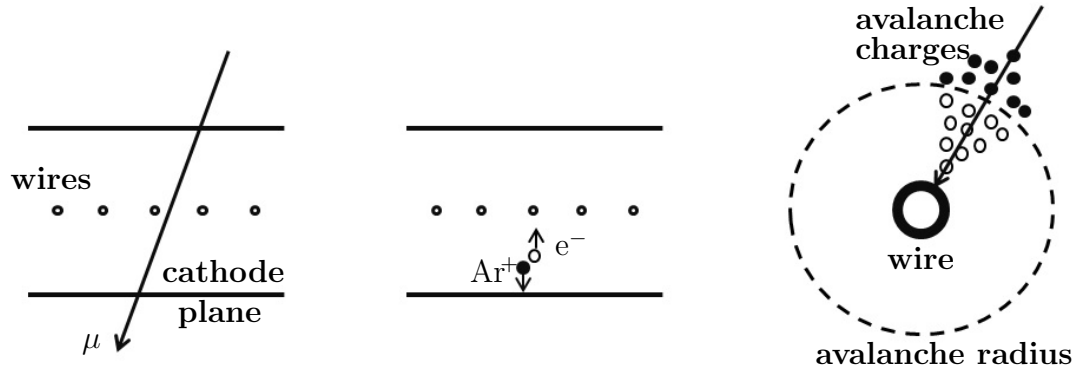


Figure 3.1: Detection mechanism is shown in sequence from left to right. 1.) A muon traverses the wire chamber. 2.) A pair of argon-electron ions is produced and drifts. 3.) When the electron closes in the sensing wire, charges avalanche and are picked up by the wire.

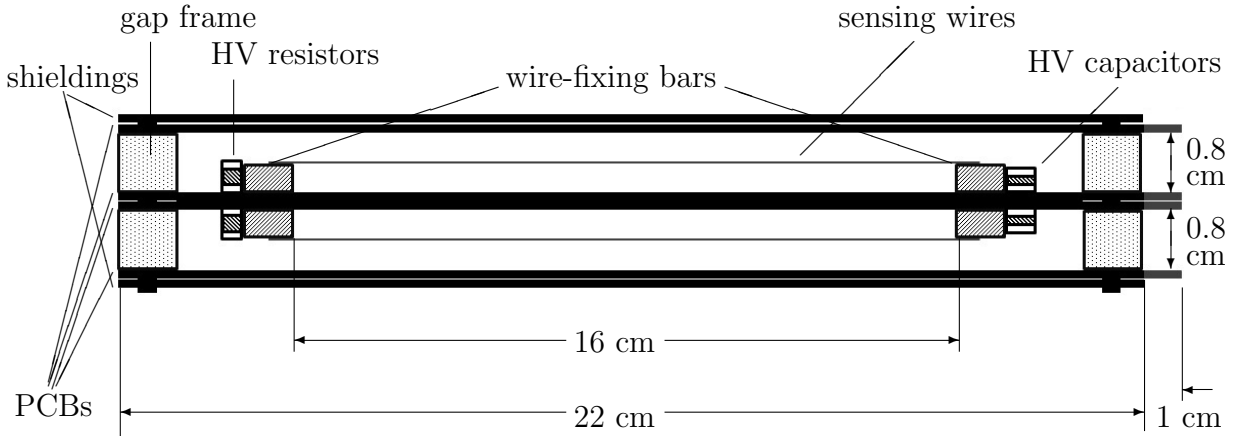


Figure 3.2: A cross-sectional diagram of the wire chamber with the view plane parallel to the sensing wires.

The dimension of the wire is $20 \text{ cm} \times 22 \text{ cm} \times 0.28 \text{ cm}$ (width \times length \times thickness). There are two gas gaps of volume $18 \text{ cm} \times 20 \text{ cm} \times 0.8 \text{ cm}$ defined by four identical FR-4 printed circuit boards (PCBs). Each of the two gas gaps is covered on its 4 sides by an acrylic gap frame, and its bottom and top by two cathode panels. Then the two gas gaps are stacked up and are glued together by conducting epoxy to form a single unit of wire chamber. 48 anode sensing wires are aligned in parallel to the length of the chamber. The wires are mounted onto the middle

panels.

The topmost and bottommost layers of the chamber are two 2-mm copper shielding. The copper thickness corresponds to the skin depth of an 1 kHz electromagnetic wave. It provides a basic shielding for the detection area against high frequency noises such as the 38 kHz noise from the fluorescent light tubes.

The cathode panel PCBs in Fig. 3.3 are of the same area as the chamber ($18\text{ cm} \times 20\text{ cm}$) and of a thickness 2 mm. Two protruded sockets of $1\text{ cm} \times 9.5\text{ cm}$ are located at one of the width-side and one of the length-side of the panels. They are for the mounting of the connector sockets connecting to the front-end system. Each socket has 22 metal pads. 16 of the 22 metal pads are for read-out of either the sensing wires or cathode strips. The remaining 6 metal pads are for grounding the cathode planes. Four 1-mm gas holes are drilled on the panels to allow gas flowing between the two gas gaps. In operation, all but two gas holes on one end of the middle two panels are sealed to control the P10 gas flow.

The panel PCBs are laminated with $15\text{ }\mu\text{m}$ gold-plated copper on the conducting areas. An isolated high voltage strip is printed on the panels. It is connected to the HV source to deliver electrical potential to the sensing wires. All high voltage areas are isolated at least 2 mm from the grounded conductors.

Sixteen $16\text{ mm} \times 0.95\text{ mm}$ cathode strips are milled on the cathode plane. The strips are 0.5 mm separated from each other and are aligned perpendicularly to the sensing wires. In the first version of the wire chamber front-end design, only the anode sensing wires are read-out while all the cathode strips are grounded. In the future, the wire chamber can be upgraded to a cathode strip chamber (CSC). The cathode strips will be grounded virtually and will be connected to another dedicated front-end. The strip front-end will read-out positive argon ion signals, which are complementary to the electron signals from the sensing wires. The strip signals will provide an extra coordinate of the ionization vertex, such that a single gas gap can give the information on both the x - and the y -coordinates of an incoming muon. Also, the ion signals can give a muon track resolution < 1

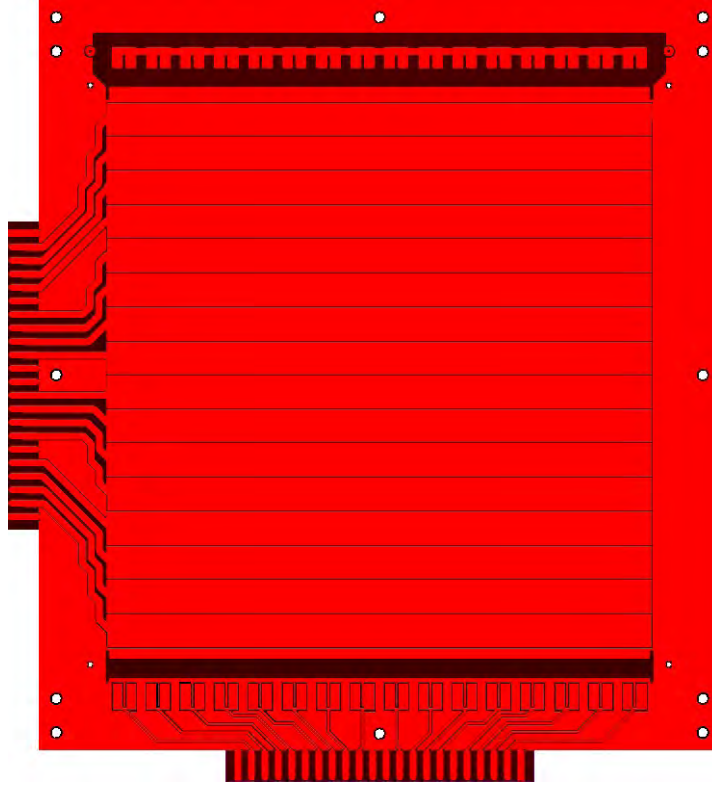


Figure 3.3: PCB layout of the cathode plane. The HV area is on the top and the signal read-out is at the bottom. The sensing wires (not shown) lie vertically.

cm if the signals are properly digitized.

Two 8 mm-thick transparent acrylic gap frames are used to define the thickness of the two gas gaps. The gap frames are bolted together with the panels with 12 screws. There are three holes in total on the two gap frames, two 4-mm holes for the gas inlet and outlet and one 2-mm hole for the high voltage (HV) wire. The contact edges of the panels and the gap frames are sealed tight by room temperature vulcanizing silicone (RTV). O-rings are placed at the screw locations to improve gas-tightness.

We glued two 4-mm thick PCB wire-fixing bars on the PCBs with the constructional epoxy adhesive 2216. The wire-fixing bars are for the mechanical mounting of the sensing wires onto the panels. The wires are held on the middle of the gas gap by the wire-fixing bars, such that the distance between the wires

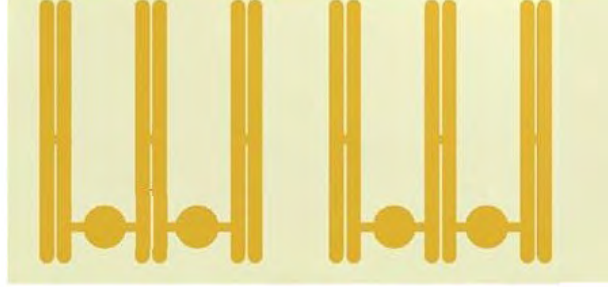


Figure 3.4: A part of the wire-fixing bar showing the wire-soldering pads of two channels (six sensing wires).

and the top cathode panel is 4 mm, the same as that between the wires and the bottom cathode panel. There are gold-plated copper pads on the wire-fixing bars (shown in Fig. 3.4) onto which the sensing wires are soldered. The metal pads group every three wires in parallel, into a single channel. The total 48 sensing wires are therefore grouped into 16 channels for read-out. The wire separation within a group is 3.3 mm, while the separation between two adjacent groups is 3.4 mm. Therefore each channel occupies an area of $1 \text{ cm} \times 16 \text{ cm}$.

Troughs are milled onto the wire-soldering pads such that the wires are easily aligned with $\sim 100 \text{ }\mu\text{m}$ precision during hand-soldering. The troughs are occupied by the wires and solder after mounting. Hence, discharges due to the sharp edges of the troughs are not a concern.

The anode sensing wires are $20 \text{ }\mu\text{m}$ -diameter gold-plated tungsten made by Luma Metall. We use tungsten for its tensile strength, which provides the mechanical robustness during the routine operation. In particular, there is a minimal tension requirement for a wire chamber [36]. For the wires to be in a symmetric electrostatic equilibrium configuration, the minimum tension is

$$T_{\min} > \frac{1}{4\pi\epsilon} \left(\frac{cVL}{s} \right)^2, \quad (3.1)$$

where the length of the wire is $L = 16 \text{ cm}$, the operating voltage is $V = 1600 \text{ V}$ and the wire separation is $s = 3.3 \text{ mm}$. The cathode-anode capacitance c per

unit length [37] is given by

$$c = \frac{2\pi\epsilon}{\frac{\pi h}{s} - \ln\left(\frac{\pi a}{s}\right)} = 7.2 \text{ pFm}^{-1} , \quad (3.2)$$

where the thickness of half the gas gap is $h = 4$ mm and the wire diameter is $a = 20$ microns. A simulation by GARFIELD-9 with the same geometric settings shows that the linear charge density on each wire is 115 pC/cm. It translates to a capacitance of 7.2 pF/m, in agreement with our calculation.

The tensile strength of the sensing wire is 2400 Nmm^{-2} [35], which gives a breaking tension of 0.75 N. If we define 75% of the tensile strength as the maximum safety tension, the wire tension range is

$$0.29 \text{ N} = T_{\min} < T < T_{\max} = 0.56 \text{ N} .$$

We mount the sensing wires with a 0.39 N tension (half of the tensile strength) set by a 40 grams weight. The two anode wires on both ends of the chamber are replaced by two $200 \mu\text{m}$ steel wires. The use of thicker wires reduces the E-field at the asymmetric edges. This prevents the last wires from spontaneous discharges.

The sensing wires of each channel are connected to the cathode panel high voltage strip through a $10 \text{ M}\Omega$, 0.5 W thick film surface mount resistor. The resistor dissipates the power of the HV power supply when the sensing wires charge, discharge or accidentally spark. It also blocks the fast signal current from exiting through the HV end. On the signal end, the sensing wires of each channel are connected to the cathode panel, then to the front-end, through a 1 nF , 4 kV ceramic surface mount capacitor. The capacitor effectively isolates the HV area from the dedicated front-end electronics. The large capacitance also means that the signal current can easily pass through the capacitor and reaches the front-end.

3.3 Operation Specification

The gas gaps are pumped with the P10 fill gas (90% Ar - 10% CH₄) at 1 atmospheric pressure and room temperature. We have chosen inexpensive argon gas as it requires relatively low electric field intensity to avalanche. The 10% of methane is added as a quench gas. It absorbs positive charges from the avalanching argons atoms near the wires to prevent the gas from continuous discharging. It also de-excites the argon atoms, such that the excited argon atoms do not de-excite itself through the emission of UV photons, which may trigger ionization elsewhere in the chamber.

The gas is filled into the chamber from a P10 gas cylinder through a regulator and a flow-meter, which control the flow rate of the gas. The gas enters the chamber through the front side of the top gas gap of the chamber. It passes through the two gas holes at the middle panels located at the back of the gas gaps and enters the bottom gas gap. The gas outlet is located at the front side of the bottom gas gap. This configuration ensures a proper circulation of the P10 gas inside the wire chamber. The gas lastly passes through a bubbler before being released into the atmosphere.

The wire chamber is flooded with a large flow of P10 gas before operation starts. This procedure purges the atmospheric gas, which contains harmful contaminants such as oxygen and water vapor. During operation, a continuous gas flow is set to $\sim 0.1 \text{ cm}^3\text{s}^{-1}$. The equivalent gas rate is $3.2 \text{ m}^3/\text{year}$.

An 1.6kV high voltage charges all the anode sensing wires. The wire chamber operates in the proportional region at this voltage. The electrostatic field strength [39] is given by

$$\begin{aligned} |\mathbf{E}| &= \frac{\pi V_0}{s(\pi h/s - \ln(\pi a/s))} |\cot(\pi \zeta/s)| \quad \text{where } \zeta = x + iy, \\ &\approx \frac{V_0}{(\pi h/s - \ln(\pi a/s))} \frac{1}{r} \quad \text{close to a sensing wire.} \end{aligned} \quad (3.3)$$

Note that the E-field equation is in unison with the capacitance equation Eq. (3.2).

The signal strength on the sensing wire is characterized by the multiplication factor M . Assume a single cosmic muon has ionized N_0 electrons in the gas. After the arrival at a sensing wire, the electrons have undergone avalanche and have multiplied to a number N . The ratio N to N_0 is given by

$$\frac{N}{N_0} = M = \exp \left(\int_{x_i}^{x_f} \alpha(x) dx \right) , \quad (3.4)$$

where $\alpha(x)$ is the Townsend coefficient.

The typical number of primary ionization electrons N_0 due to a 1 GeV cosmic ray muon is $\approx 25 \text{ cm}^{-1}$. Nonetheless, a small fraction of high momentum exchange collisions can knock out an electron with a high momentum from an argon ion. This kind of electron, known as the delta electron or delta ray, is itself ionizing and can produce more ionization pairs. The delta electrons boost N_0 to $\approx 100 \text{ cm}^{-1}$ [33].

We approximate the Townsend coefficient to be proportional to the E-field $\alpha(x) = kE(x)$ for some constant k . At a region close to the sensing wire, the E-field pattern is similar to that in a drift tube. We can express the multiplication factor by the Diethorn formula [40], by replacing the linear charge density of the drift tube with that of the wire chamber,

$$\ln M = \frac{V}{\pi h/s - \ln(\pi a/s)} \frac{\ln 2}{\Delta V} \left(\ln \frac{V}{(\pi h/s - \ln(\pi a/s))a/2} - \ln pK \right) , \quad (3.5)$$

where $p = 1 \text{ atm}$ is the fill gas pressure. $\Delta V = 23.6 \pm 5.4 \text{ V}$ and $K = 48 \pm 3 \text{ kV/cm}\cdot\text{atm}$ are two P10-specific constants measured by another experiment [41]. They correspond to the effective energy per unit charge required to ionize an electron from the gas and the minimum field required for ionization respectively.

The numerical value of the multiplication factor for the CUHK wire chamber geometry is

$$M = 6700 , \quad (3.6)$$

$$Q_{\text{signal}} = Ne = N_0 Me \sim 0.1 \text{ pC} .$$

which is an acceptable charge signal for the front-end.

In general, we expect a deviation from the linear E dependence approximation of the Townsend coefficient. The deviation includes low energy deviation such as gas attachment effect, and high energy deviation such as a non-linear dependence on E-field. Nonetheless, the deviation due to the space charge effect should be small as the chamber's voltage is in the proportional region.

We will carry out a detailed simulation on all the charge dynamics by a CERN program called “GARFIELD-9”, from which we can acquire a more realistic multiplication factor. Yet, we expect Eq. 3.6 to be a good order-of-magnitude estimation of the true M .

Chapter 4

Wire Chamber Simulation by GARFIELD-9

4.1 Introduction

We want to optimize the wire chamber design by simulating the chamber's operation. In particular, we simulate the chamber mechanical and electrical properties to ensure the robustness of the chamber. We also simulate the signals to facilitate our front-end circuit design. Lastly, we simulate for the possible effects from the imperfections (during assembly or operation) in the wire chamber.

We simulate the wire chamber using GARFIELD-9 [42], a drift chamber simulation program developed by Rob Veenhof. Drift chambers are modeled as being made up of thin wires and plates. GARFIELD calculates the electric fields of the wire chamber and the electromagnetic interactions of the charges in an E-field with gas. It supports 3D configuration simulations, but we only need the 2D field simulation (along the cross-sectional plane of the wire chamber) for our propose.

GARFIELD also interfaces with two Monte Carlo programs which impart the P10 gas properties to our simulation. MAGBOLTZ simulates the drift behaviors of electrons and ions in gas, and HEED simulates the ionization behaviors.

The aims of our simulation are to verify and study

- the physical locations of the sensing wires,
- the electric field and the drift lines in the wire chamber,
- the charge arrival time, the avalanche multiplication factor and the signal pulse shape due to the wire chamber gas and geometry,
- the deviation of the above from the nominal values as a function of the deviation of the gas and geometry settings from the nominal ones.

4.2 Wire Chamber Modeling

We simulate a 2D cross-sectional plane of the wire chamber which cuts through the row of sensing wires. The underlying assumption is that the wire chamber is infinitely long along the length of the sensing wires. We divide the wire chamber geometry into the central and the edge parts.

For the central part of the chamber, we have assigned a few sensing wire channels in the region of simulation. The wire geometry is then repeated on the both sides to make an infinite periodic row of anode wires. Above and below the row of wires are two infinite grounded cathode planes. The information about the wires, the boundary potentials and the gas content are put in according to the wire chamber descriptions.

We have plotted a drift line graph and an electric potential contour graph to demonstrate the geometry of the central part of the chamber. The positions of the anode wires and the cathode planes can be seen clearly in the two figures. The drift lines in Fig. 4.1 indicate the drifting paths along which the free charges in the chamber will move. They are approximately along the directions of the electric fields. The potential plot in Fig. 4.2 shows the property of a typical multiwire chamber electric field. The field is capacitor-like in the regions farther than 1 mm away from the anode wires. Near the anode wires, the field changes into wire-like.

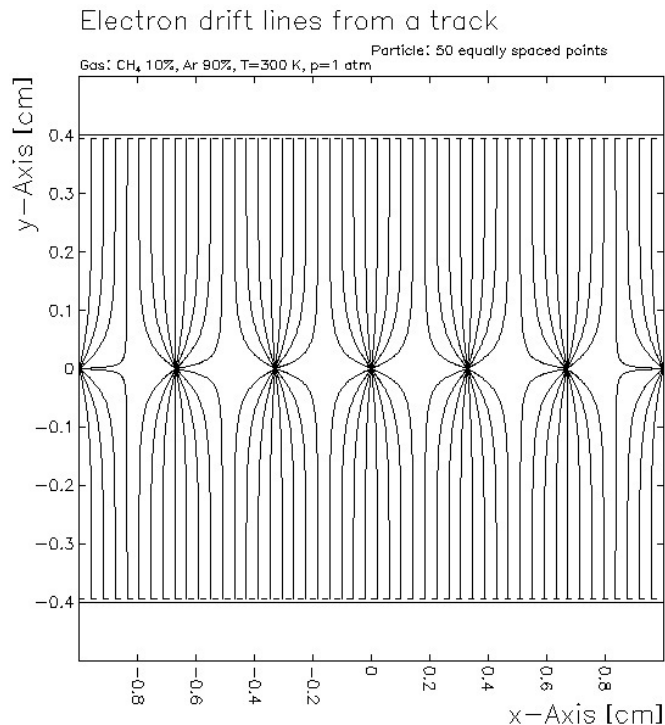


Figure 4.1: A drift line plot in the central region of the wire chamber, calculated by GARFIELD.

The edge part of the chamber is almost identical to the central part simulation, except that we have lifted the periodicity requirement. We still place an infinite row of wires on the one side of the chamber, but we leave the other side empty. We identify the wire at the end of the row as the guard wire, on which we impose a different diameter and material. We still use the two infinite planes as the cathode planes. This is justified since the cathode planes extend for 2 cm on both sides beyond the guard wires, while the maximum inter-wire separation is just 0.34 cm. The cathode planes look locally like two infinite planes even at the edge.

Similarly, we look into the drift line graph in Fig. 4.3 and the potential contour graph in Fig. 4.2 of the edge part of the chamber.

While the drift line graph is what we have expected, the potential contour graph has demonstrated our infinite cathode planes assumption. The electric field

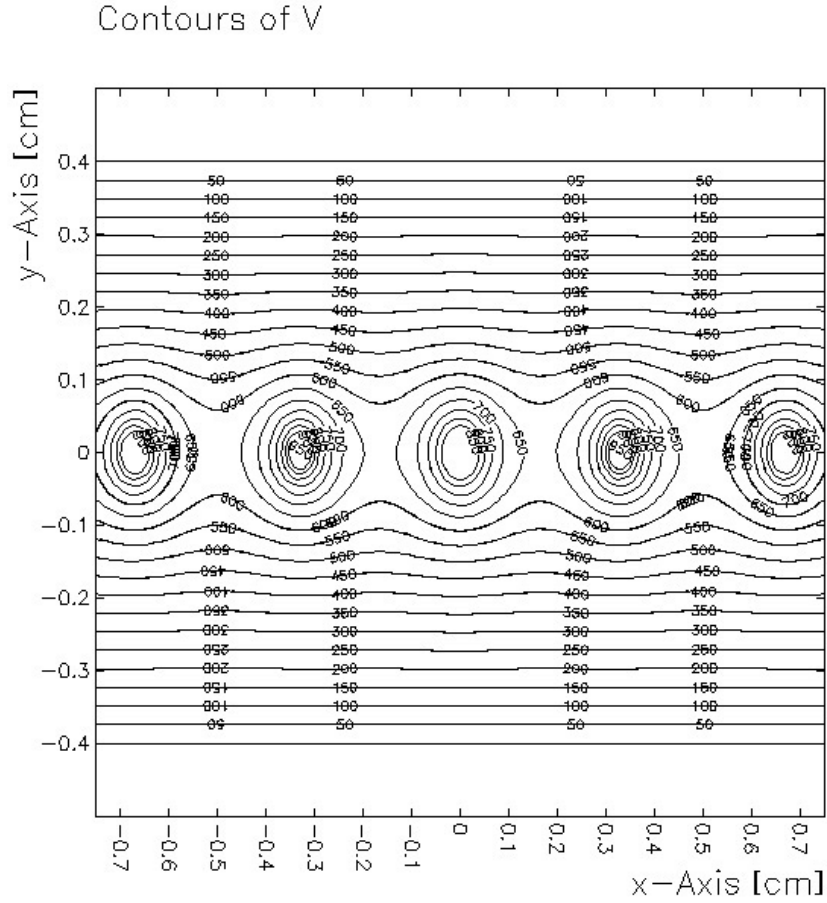


Figure 4.2: Same as Fig. 4.1, but for equipotential contours.

decays fast enough outside the guard wire such that the field in the region 1 cm away from the guard wire is already negligible.

The use of the guard wires is to prevent an unwanted discharge on the edge of the chamber due to the loss of the translational symmetry, when the chamber operates at a voltage very close to the breakdown voltage of the P10 gas. From the simulation, the E-field at the edge wires is increased by 12% compared to the central region if the thicker guard wires are not used.

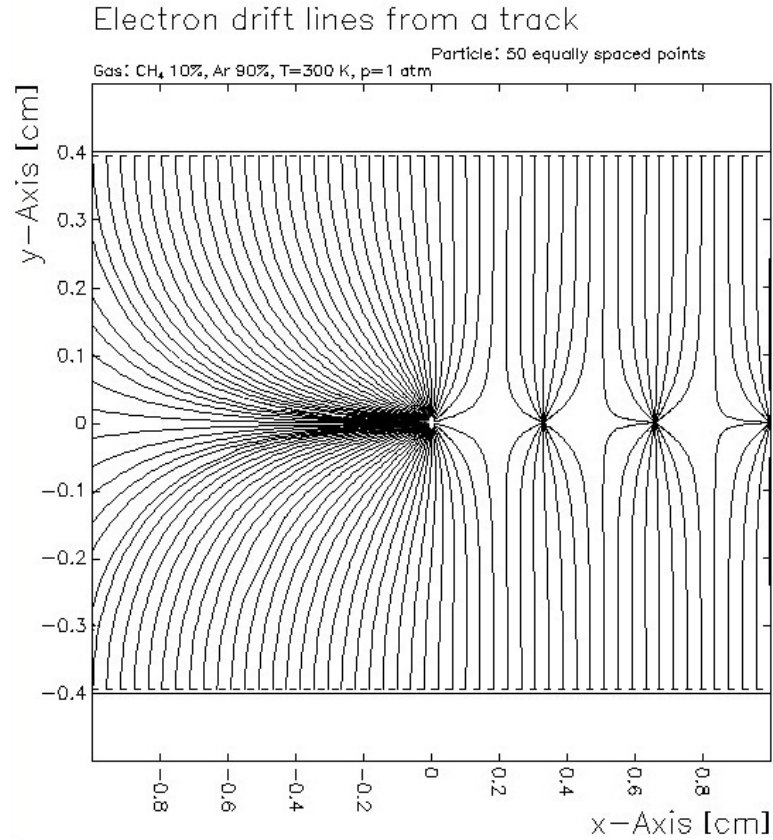


Figure 4.3: Same as Fig. 4.1, but for the edge part of the wire chamber.

4.3 Mechanical Equilibrium of the Sensing Wires

GARFIELD can be used to simulate the anode wire sag due to the external forces. The external forces include the gravity, the electrostatic repulsion and the wire tension. We have put in the nominal tension 40 grams and the tungsten density 19.17 g/cm^3 . We are especially interested in whether the wires stay near the nominal position or they shift to a new equilibrium due to the electrostatic repulsion effect.

When all the wires are in symmetric positions, the wires should be near their nominal positions as the electrostatic repulsion cancel out each other, if the calculation in Eq. (3.1) of section 3.3 is correct. We expect that the main contribution to the wire sag is due to the downward gravity. This is verified in Fig. 4.5. The maximum downward sag is of $0.5 \text{ } \mu\text{m}$, which is much less than a wire diameter

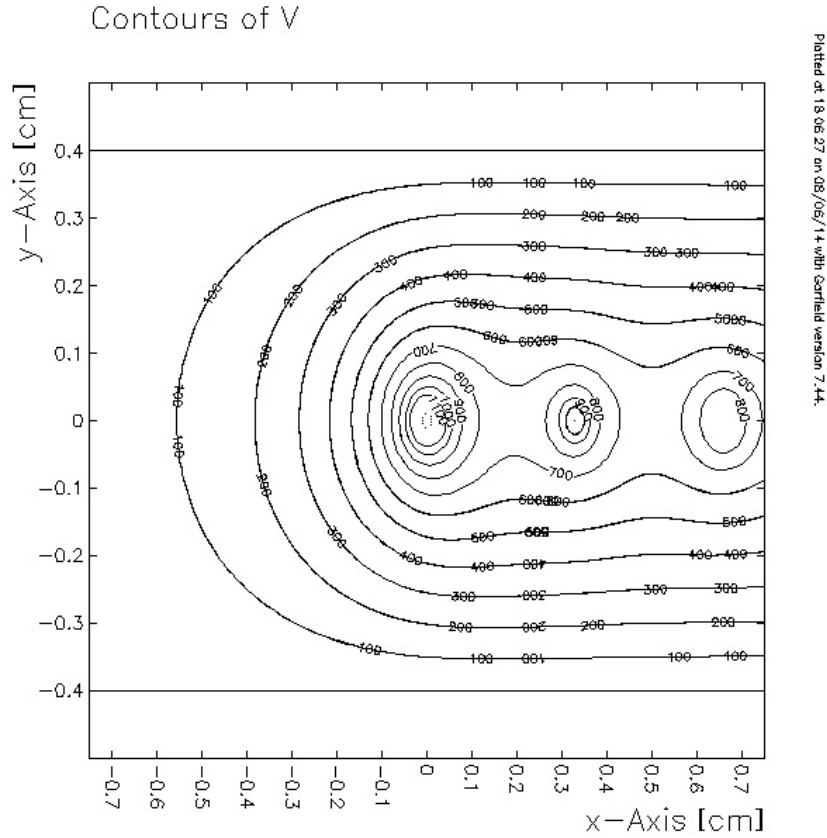


Figure 4.4: Same as Fig. 4.2, but for the edge part of the wire chamber.

and is negligible.

In addition, we introduce a relative vertical displacement between the wires, such that the central wire is $20 \mu\text{m}$ either below (Fig. 4.6a) or above (Fig. 4.6b) its two adjacent wires. The magnitude of the relative displacement ($= 1$ wire diameter) is physical. It could be introduced during wire soldering. Such displacement will enhance the electrostatic repulsion effect and can cause a mechanical equilibrium shift.

The simulated wire position shows an enhanced sag when the wire is displaced downward. The maximum vertical sag is $0.9 \mu\text{m}$, still less than 1% of the wire diameter. The sag is relieved when the wire is displaced upward. The maximum vertical sag is only $0.04 \mu\text{m}$.

The simulation is consistent with the electrostatic repulsion model. The wires

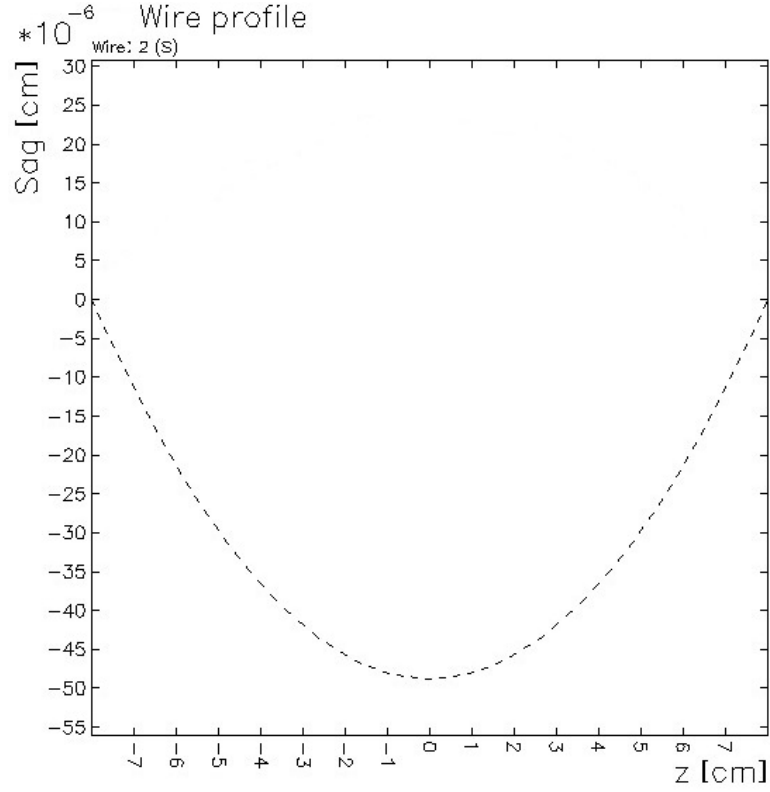


Figure 4.5: A plot of wire vertical sag against the length of the wire.

are similarly charged and they repel each other. In Fig. 4.6a the electrostatic repulsion of the adjacent wire adds onto the gravitational bending. Thus the wire sag increases compared to Fig. 4.5. In Fig. 4.6b, the electrostatic force counteracts the gravity on the wire. The sag is reduced as the two forces cancel out each other partially.

In both cases, the shifts of the anode wire position are negligible as they both are much less than a wire diameter. This simulation verifies the robustness of the wire positions against the external forces. Hence, wire mechanical equilibrium position shift is not a concern under the 40 grams wire tension.

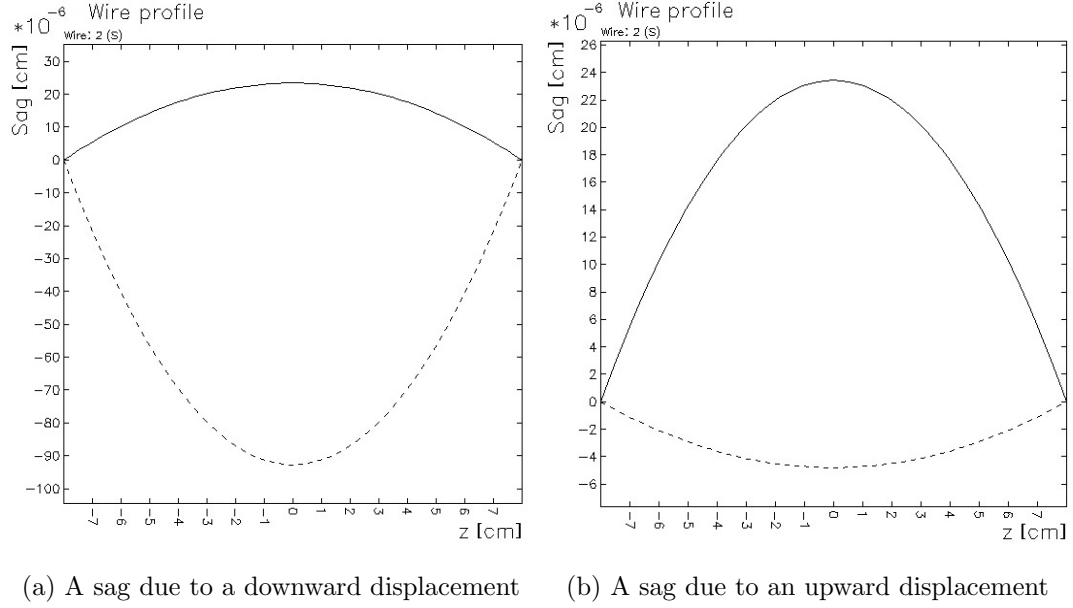


Figure 4.6: Simulated wire displacement. The solid lines are the horizontal sags along the wire-plane. The dashed lines are the vertical sags along the force of gravity.

4.4 Signal Response

4.4.1 Event Settings and the Multiplication Factor

We simulate an event of a \sim GeV cosmic muon passing through the wire chamber at a small inclination angle. The cosmic muon ionizes the P10 gas atoms/molecules in the wire chamber. The ionization electrons drift to the sensing wires to produce a current signal through avalanche. A 3D display of a typical event is in Fig. 4.7.

Through this simulation, we want to study the avalanche multiplication factor, the drift timings and the signal features. These values are critical to the chamber geometry, the front-end electronics and the data acquisition system designs.

We can identify the main features of a cosmic muon event. A muon passes through the chamber in a straight line. It produces $\gtrsim 10$ clusters of primary ionization along its way. The argon ions drift to the cathode planes and the

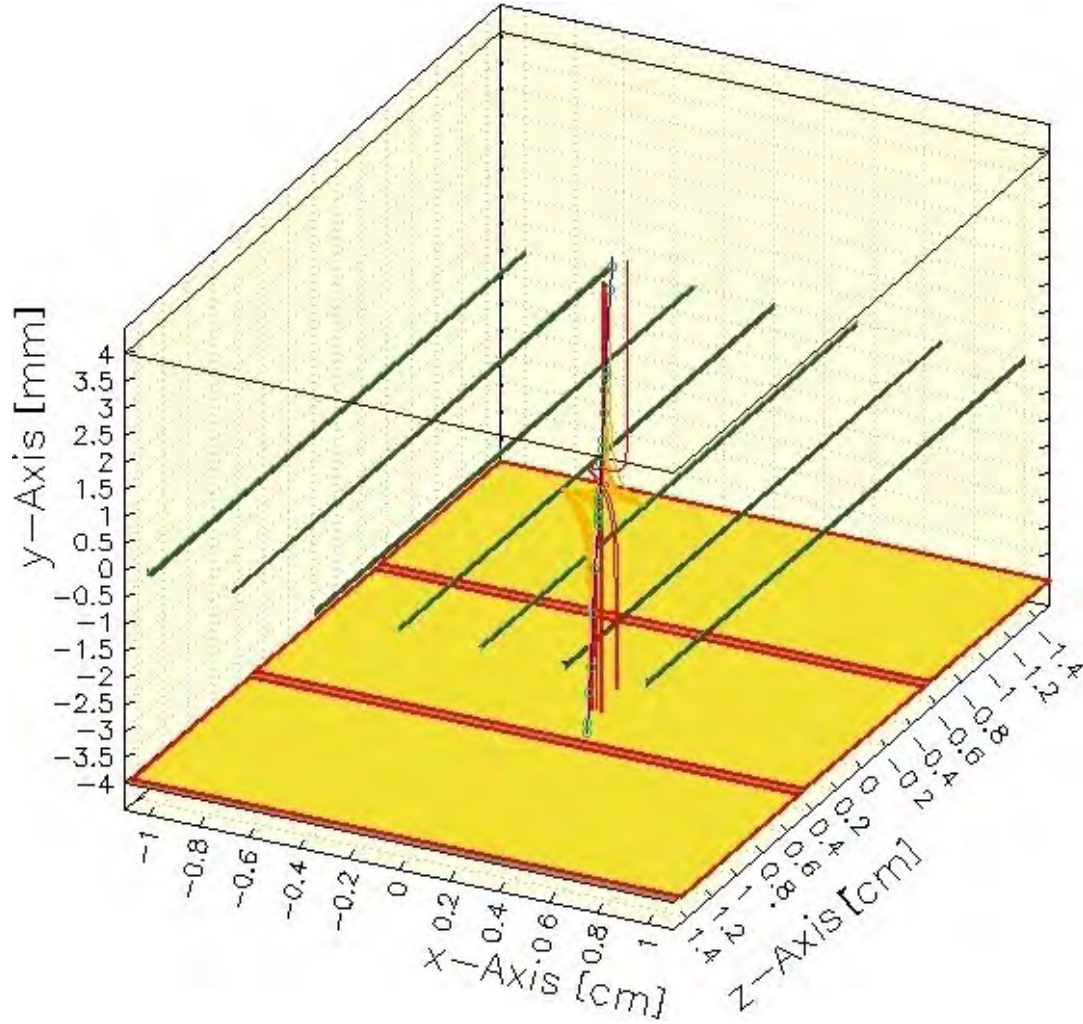


Figure 4.7: A 4 GeV cosmic muon event in a segment of the wire chamber showing the muon (blue), the drift ions (red) and the drift electrons (orange).

electrons drift to the anode wires. The charge avalanche at the anode wires can be inferred from the argon ions originated from the wires (the red tracks overlaid by the orange electron tracks in Fig. 4.8), which drift towards the cathode planes. The drift paths approximate those in Fig. 4.1.

The simulated multiplication factor is $M \approx 12000$. The multiplication number is, to 1%, independent of the primary ionization cluster location, unless the track and the ionization cluster are chosen to be very close to the wire. If a cluster is very close to the wire, the electron gains less kinetic energy before hitting the

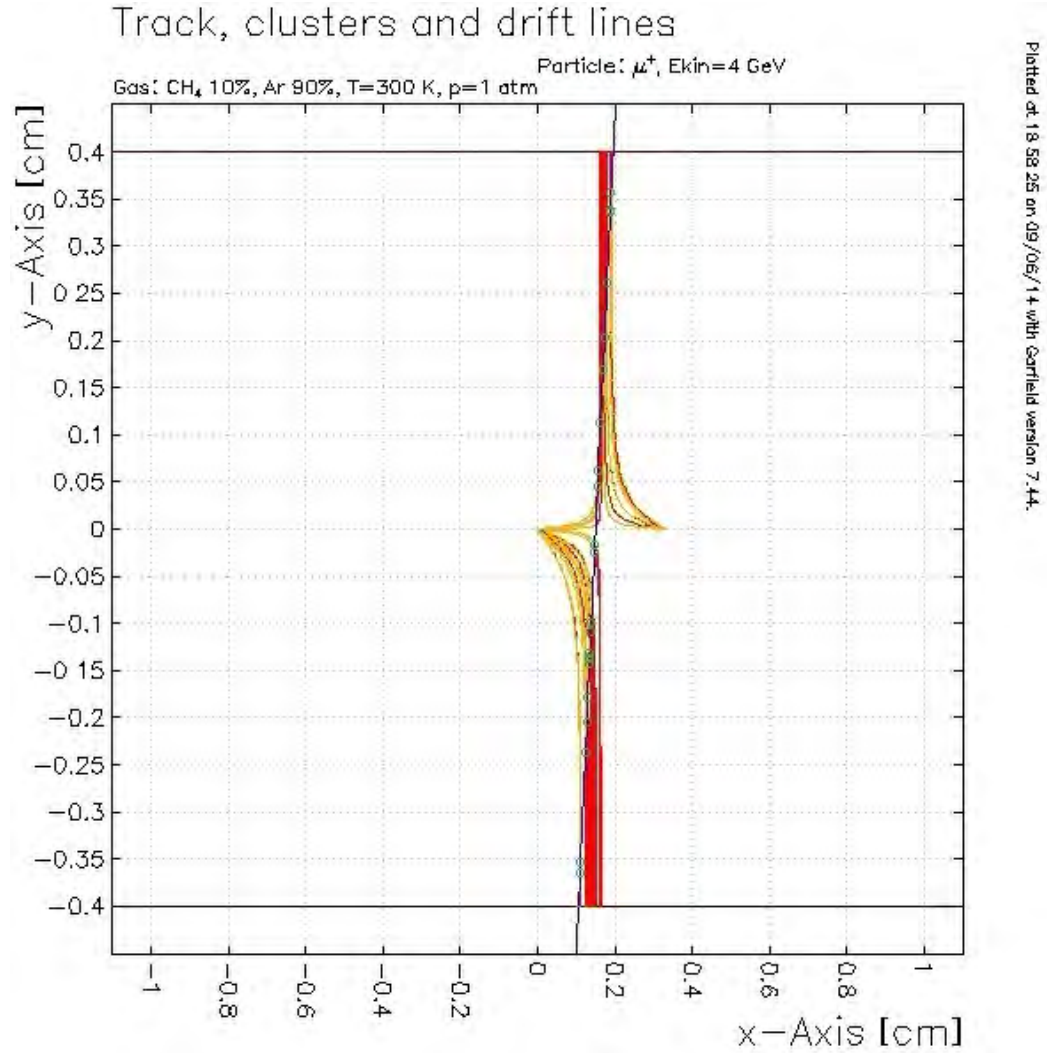


Figure 4.8: The same event in Fig. 4.7 in the 2D cross-section of the wire chamber.

wire, which results in a smaller M .

The simulated M value is about a factor of two greater than that estimated in Eq. (3.6). The order of magnitude of the estimation and that of the simulation agrees with each other. The track-integrated Townsend coefficient α (the physical parameter) in the simulation deviates by $\ln 2 \approx 0.69$ from the theoretical prediction. The error of the Townsend coefficient is roughly 8%. We can say that the theoretical estimation already captures the important physics in the avalanche process.

4.4.2 Electron Arrival Timings

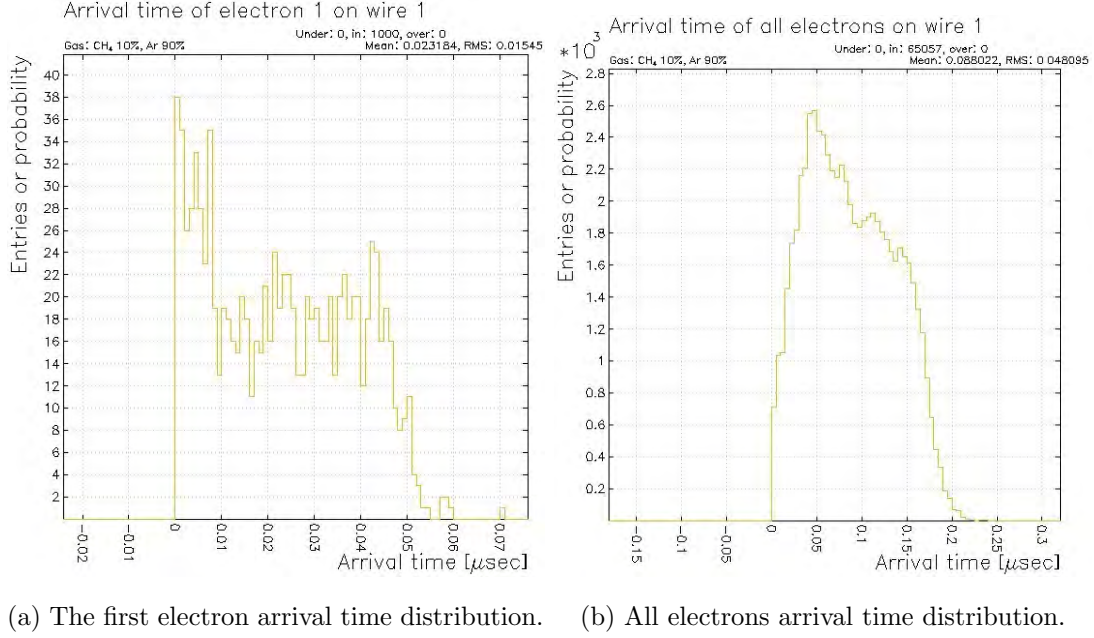


Figure 4.9: Arrival time distribution in one set of Monte Carlo track sample.

We have run 10 sets of Monte Carlo tracks for the arrival time distributions and the signals. Each set contains ~ 1000 track samples.

The electron arrival timings are critical for setting the n -fold coincident window between the different gas gaps. Coincidence is our main strategy against the backgrounds, such as the gamma rays and the beta radiations.

The mean arrival time of the first electron is 23 ns. At 50 ns, the probability that the first electron has already arrived at the anode is above 0.9.

As a sanity check, we compare the simulation result with the result of another experiment [44] aiming to measure the electron mobility, which is the terminal velocity of an electron in the P10 gas per electric field. The first electron arrival

time corresponds to an electron drift mobility of

$$\begin{aligned}
 \mu_e &= \frac{d_{\text{gap}}}{\tau_{\text{arrival}} \cdot |\vec{E}|}, \\
 &\approx \frac{4 \text{ mm}}{50 \text{ ns} \times 400 \text{ V/mm}} \quad \text{assuming parallel plate capacitor,} \\
 &= 2 \text{ cm}^2\text{kV}^{-1}\mu\text{s}^{-1}.
 \end{aligned} \tag{4.1}$$

The order of magnitude of the electron mobility agrees with that in the experiment ($\approx 5.5 \text{ cm}^2\text{kV}^{-1}\mu\text{s}^{-1}$ in 1 atm). The difference is due to the extrapolation of E-field at 4000 V/cm^{-1} and the simplification of the row of wires into a conducting plate in the calculation.

We expect the signal time-separation from two separated gas gaps due to a single cosmic muon should be around 20 - 50 ns. This sets the time scale of a 2-fold coincidence in the back end DAQ for the cosmic muon detection.

In general, a time window of the first electron arrival time may not be sufficient for a signal to rise above the front-end threshold. A way to maximize the efficiency is to consider the arrival time of all the electrons. From Fig. 4.9b, 90% of the avalanche electrons arrive at the sensing wires within 180 ns. This defines the coincidence time window between the two gas gaps of a wire chamber unit, because any ionization electron due to a single cosmic muon must arrive at the anode wire from its primary cluster within this 180 ns. Otherwise the two signals are uncorrelated.

4.4.3 Current Signals

Finally, we look at the current signal on the sensing wires. The signal is negative since it is due to the electron drift towards the wire. The signal peaks at multiple positions over a duration of ~ 200 ns. The separated peaks correspond to the primary clusters at different positions along the cosmic muon track. The amplitudes of the peaks vary from a few 100 nA to a few μA , depending on the primary ionization cluster size.

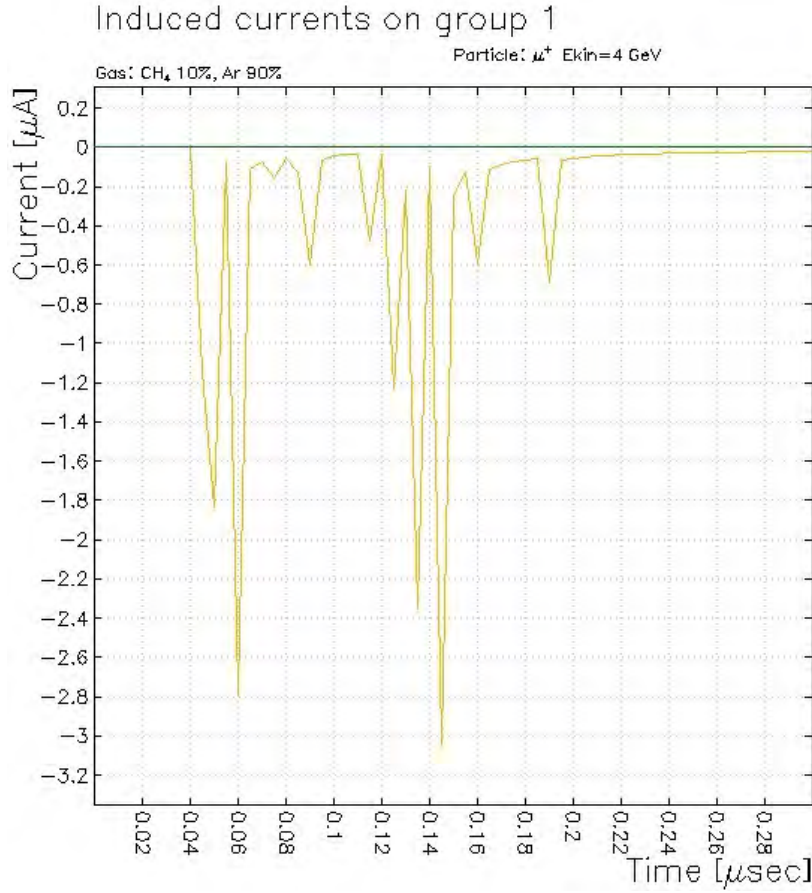


Figure 4.10: A plot of the current against the time on the signal wire.

We employ a charge amplifier at the front-end. The amplifier is only sensitive to the total charge (i.e. time-integrated current) of the signal. Therefore we need to calculate the signal pulse area to estimate the voltage response of the amplifier. During integration, we may assume that the signal to be purely due to the electron drift signal shown in the Fig 4.10, since the ion movements are very slow (over 10 - 100 μs) such that the argon ions seem to be frozen at the electron drift time scale. The front-end is not responsive to the slow ion tails.

Under the above assumption, we integrate the signal current. Since we employ a resistor to discharge the charge-amplifier, we need to include an exponential convolution $e^{-t/\tau}$ of a time constant $\tau = C_1 R_1 = 1 \mu\text{s}$ in the signal integration. The details can be found in the section 5.1.3. The voltage response of the charge-

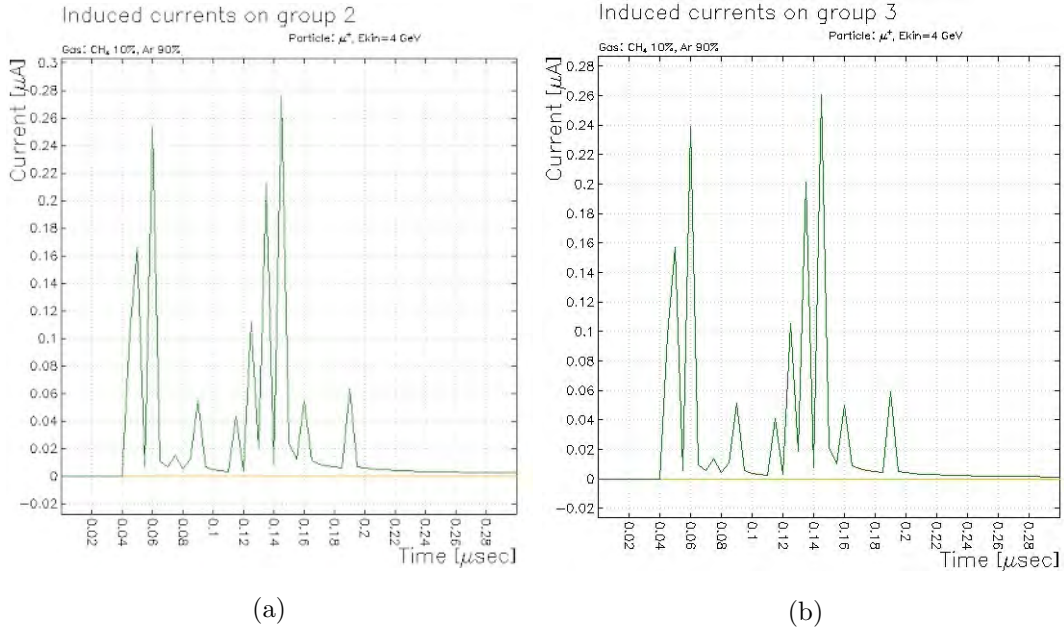


Figure 4.11: The current against the time of the wire (a) to the left of the signal wire and (b) to the right of the signal wire. The positive sign of the current indicates that the main contribution of the current is the cross-talk.

amplifier is

$$\Delta V_o = V_o - V_{\text{offset}} \approx -\frac{1}{C_1} \int_{-\infty}^t I_i(t') e^{-(t-t')/\tau} dt' . \quad (4.2)$$

The integrated signal pulse is shown in Fig. 4.12a. The curve roughly represents the output voltage shape V_o , aside from a small op-amp offset voltage V_{offset} . The pulse height represents the total charge of the original signal. The integrated signal carries a charge of ~ 0.1 pC on average. This signal size requires an amplifier with a charge amplification ratio ~ 1 V/pC for a proper signal pick-up on the front-end.

When the electrons drift towards a sensing wire, positive charges are induced on the closest wire (the one which the electrons are drifting towards). However, the positive charges on the wire will induce negative charges on the neighboring sensing wires. Therefore, weak and opposite-signed signals are induced on the channels adjacent to the signal channel. This is known as the cross-talks. In our wire chamber, the cross-talks are positive currents.

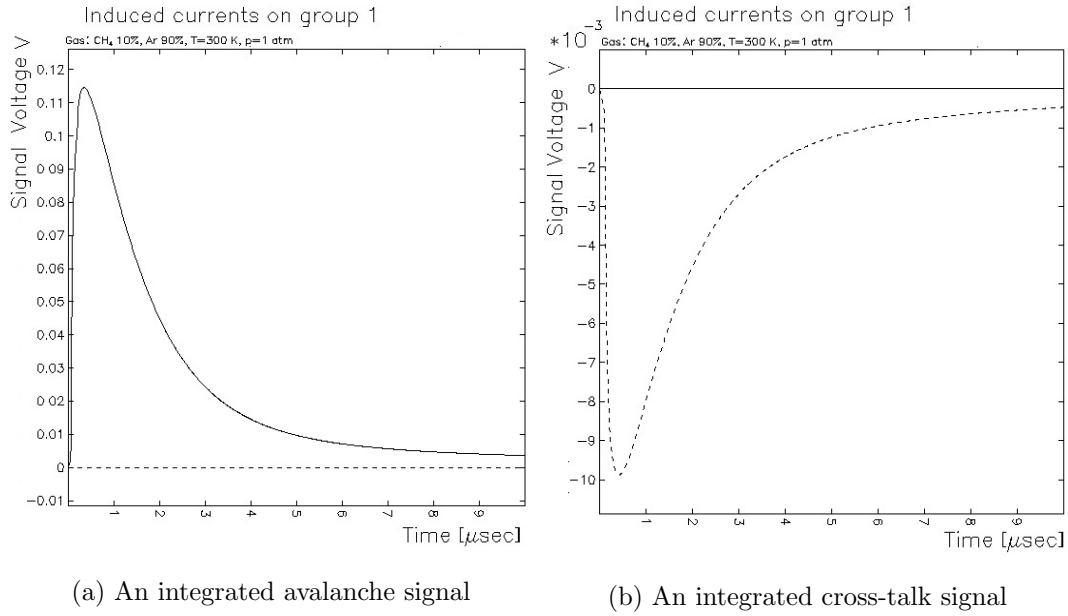


Figure 4.12: The simulated voltage signals ΔV_o after a charge-amplification, described by the Eq. 4.2.

It is important to understand the cross-talks between the channels to ensure that the idle channels do not pick up noises as fake signals. We examine the features of the cross-talk currents in the two wires neighboring to the signal wire. Due to the cross-talk mechanism, the shape of cross-talk currents should be very similar to the signal current except for a change of sign and the overall amplitude. In Fig. 4.11, the cross-talk peak locations and the relative pulse heights are indeed very similar to those of the signal in the Fig. 4.10. The amplitudes of the cross-talks are only 1/10 of that of the signal current. The small cross-talk currents and the positiveness of the cross-talk sign mean that the cross-talks on the sensing wire level can be easily filtered by the front-end discriminator. The cross-talk pulse shape after passing through a charge-amplifier is shown in the Fig. 4.12b.

4.5 Response to Gas or Geometry Deviation

We investigate how the deviations of the wire chamber settings can affect the cosmic muon signal. We simulate the change of the multiplication factor by changing some parameters of the wire chamber. The multiplication factor depends exponentially on the Townsend coefficient, which in turn depends heavily on the geometric and operational variables of the chamber. Hence, the multiplication factor is an observable very sensitive to perturbations. At the same time, the multiplication factor is directly related to the signal strength, which is critical to the whole chamber design. Understanding the relations between various variables and the multiplication factor can help us set the tolerances of the errors during the wire chamber assembly and operation processes.

The physical quantity that determines the multiplication factor is the integrated Townsend coefficient defined in Eq. (3.4). We assume that there is a small deviation δs of a certain parameter affecting the Townsend coefficient, which can be a quantity about the gas or the geometry, from the nominal value s_0 . We can expand the integrated Townsend coefficient by a Taylor series,

$$\int dx \alpha(s_0 + \delta s, x) = \tilde{\alpha}(s_0 + \delta s) = \tilde{\alpha}(s_0) + \tilde{\alpha}'(s_0) \cdot \delta s + \dots$$

This expansion results in an exponential dependent of the multiplication factor M on the deviation parameter δs . i.e. for small δs ,

$$M \approx M_0 e^{B_s \delta s}, \quad (4.3)$$

where $M_0 = \exp(\tilde{\alpha})$ is our original multiplication factor. The constant $B_s = \tilde{\alpha}'$ is acquired for different parameters s using an exponential fitting function on the simulation data points. The equation helps us calculate locally the maximum deviations allowed given a multiplication tolerance.

We study the deviations of the two geometric variables from their nominal values. They are the gas gap thickness and the sensing wire horizontal position. A deviation of the gas gap thickness from the nominal 8 mm can be due to the

mechanical stress on the wire chamber, such as a weight on the top of the cathode panel or the panel bending stress by the combined tension of the sensing wires. A horizontal displacement of a sensing wire can be the error of the hand soldering process.

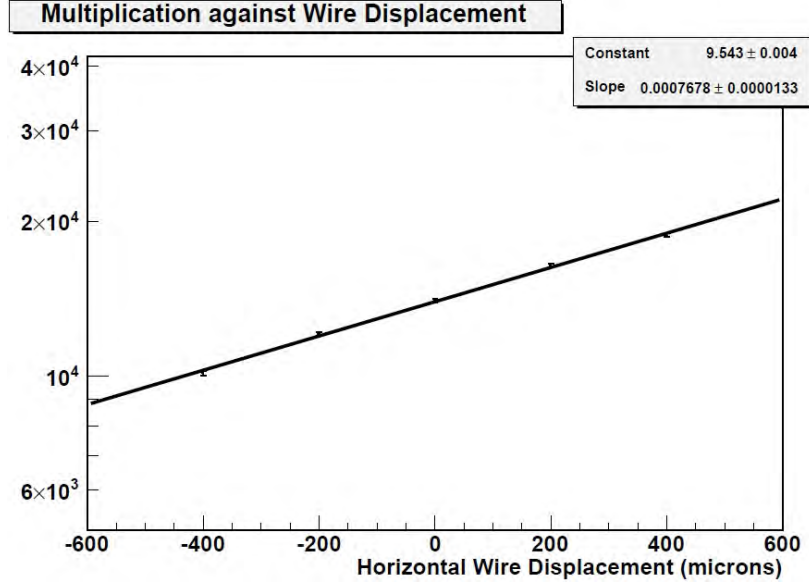


Figure 4.13: A plot of the multiplication factor against the horizontal wire displacement (+ve towards the muon track).

First we take the wire displacement as an example and we simulate 5 data points with a muon passing through the chamber vertically, 1 mm away from the sensing wire. The horizontal wire displacement is the deviation in the discussion, with $\delta s_{\text{wire}} = 0$ as the nominal value. In each step the wire is either moved towards or away the muon track by 200 μm . A set of 5 multiplication factors are to be fitted by Eq. (4.3). The “constant” displayed in the top-right fitting box in Fig. 4.13 is the unperturbed integrated Townsend coefficient $\tilde{\alpha}(s_0) \approx \ln M_0$ while the “slope” is the B_s in Eq. (4.3).

Similarly, the respective fitting parameters can be extracted in the gas gap thickness simulation in Fig. 4.14. Note that since the “constant” $\tilde{\alpha}(s_0)$ is just the log of the nominal multiplication factor. The fitting constants should be very close to each other in the different deviation parameter simulations, i.e.

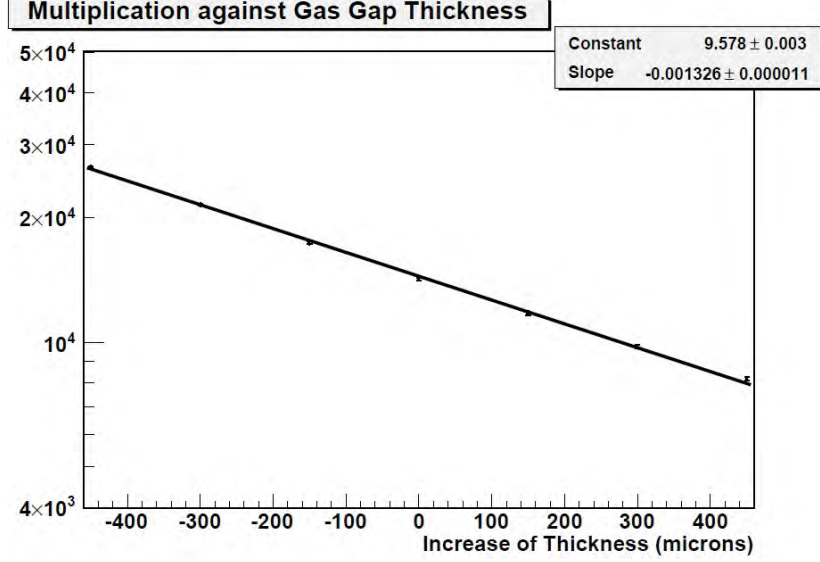


Figure 4.14: Multiplication factor vs. the gas gap thickness deviation.

$M_0 \sim e^{9.5} \approx 14000$, up to a fitting error. The fitting slope, B_s , varies greatly for different types of the deviation variable. It is the parameter B_s we want to acquire.

We also simulated the change of the multiplication factor by varying the high voltage and the gas content. For the high voltage, we inspect the value from 1.5 kV to 1.8 kV. The result is shown in the Fig. 4.15. As for the gas content, we simulate the scenario in which there is a gas leak in the wire chamber. The two molecules that we are the most concerned with are oxygen and water, both are known for their high electron attachment cross-sections [45]. They tend to absorb the drift electrons and reduce, if not totally eliminate, the final signals.

We introduce 3%, 5% and 10% (by molar fractions) of atmospheric air respectively to identify the multiplication factor variation tendency. We also simulate a dry air scenario and a wet air scenario respectively. We introduce no water vapor in the dry air simulation and 5% of water vapor in the wet air simulation. The wetness of the air represents the worst case scenario which is possible in Hong Kong, i.e. 100% relative humidity at 35°C. This setting helps tighten the minimum moisture constraints on the wire chamber. Similar to the geometric

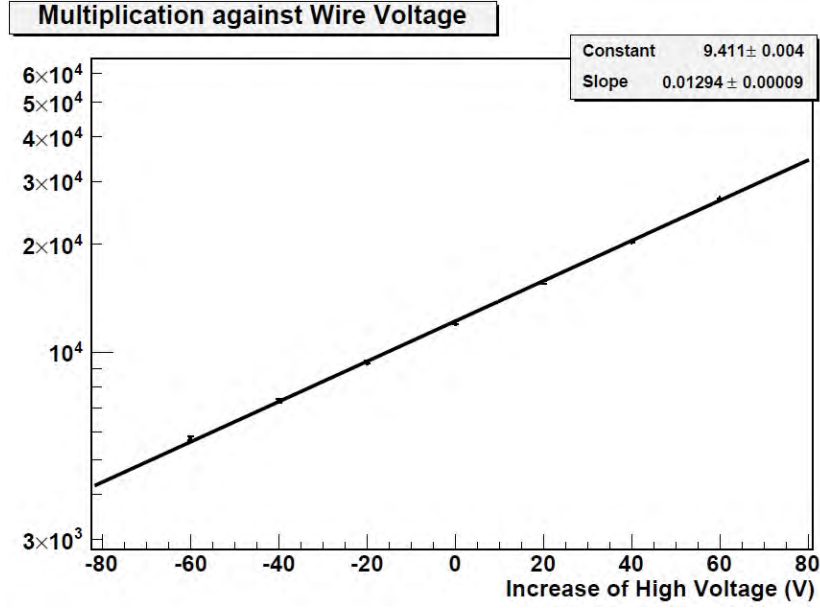


Figure 4.15: Multiplication factor against the increase of high voltage.

variables, we have extracted the “slope” fitting parameters from the high voltage and gas simulations.

We combine the full simulation results in this section and their implications on the deviation bounds in Table 4.1. The table displays the bounds of the geometry and gas variables under three $\pm N\%$ ranges of multiplication factor (gain) tolerance.

Variable	Slope (B_s)	$\pm 10\%$ gain	$\pm 25\%$ gain	$\pm 50\%$ gain
Wire displacement	$0.000767 \mu\text{m}^{-1}$	$+123_{-137} \mu\text{m}$	$+291_{-375} \mu\text{m}$	$+529_{-904} \mu\text{m}$
Gap thickness	$-0.00133 \mu\text{m}^{-1}$	$+40_{-137} \mu\text{m}$	$+216_{-168} \mu\text{m}$	$+521_{-305} \mu\text{m}$
High voltage	0.0129 V^{-1}	$+7.4_{-8.2} \text{ V}$	$+17.3_{-22.3} \text{ V}$	$+31.4_{-53.7} \text{ V}$
Gas leakage (Dry)	-10.4	1.01%	2.77%	6.67%
Gas leakage (Humid)	-10.1	1.04%	2.85%	6.86%

Table 4.1: The maximum deviations allowed under 10%, 25% and 50% multiplication factor tolerances.

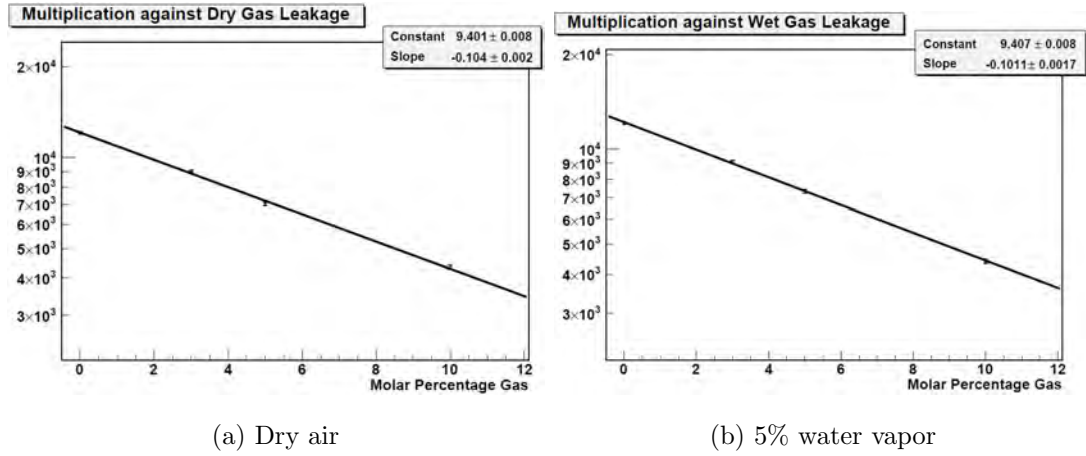


Figure 4.16: Plots of the multiplication factor against the air contamination.

We want the multiplications of the different channels, thus their signal outputs, to be approximately equal to each other, such that the efficiencies of the channels are equal given an identical front-end design among all the channels. A multiplication tolerance range of $\pm 50\%$ is reasonable for our first wire chamber prototype. We expect a tighter tolerance for future chambers after some design optimizations with our first prototype's result.

The most sensitive variable is the high voltage. At 1.6 kV, every 2% of voltage change affects the multiplication factor by 50%. Fortunately, modern high voltage supplies can easily cope with this level of stability requirement. For example, the N471 high voltage power supply from CAEN Technologies, Inc. [46] used in our setup has a maximum voltage fluctuation of mere 2 V. The effect of the voltage fluctuation on the multiplication factor is therefore not a concern.

The sensing wires are fixed to be within $\pm 100 \mu\text{m}$ from their nominal positions by the troughs milled on the soldering pads on the wire fixing bars (refer to Fig. 3.4). The wire displacement is also not a major concern. The gas contamination can also be kept within the allowed range by a proper gas-tightening and an adjustment of the flow rate.

As for the gas gap thickness, it is very susceptible to changes due to a curvature on the cathode panels. For the panels we used for our wire chamber, the PCB

production company does not specify the flatness of their PCB products. Thus, we rely heavily on the intrinsic stiffness and smoothness of the FR4 material on a $20\text{ cm} \times 20\text{ cm}$ scale.

For a future adoption of our chamber design on an even larger wire chamber, such as one of the size $60\text{ cm} \times 60\text{ cm}$, it is advisable to use some structures, like a plastic honeycomb, to support the whole cathode panel. The structure can ensure the flatness of the panels such that the gas gap thickness is equally defined for the whole detection area.

Chapter 5

CUHK Wire Chamber Front-end

5.1 Analog Front-end

5.1.1 Introduction

To pickup signals from the wire chamber, a front-end is needed to amplify and digitize the signals. The process is done by an analog front-end which has design parameters based on the previous Garfield-9 simulation. We have also added an intelligent digital front-end, described in the next section 5.2, which assists and tests various functions in the analog front-end.

The front-end of the CUHK Wire Chamber contains 16 analog channels, each of which channel is connected in parallel to 3 anode sensing wires through a capacitor. The front-end operates under three DC current input, +5V, GND and -5V. Each channel contains, in series,

- a charge amplifier for signal amplification,
- a high pass filter for noise suppression,
- and a comparator for threshold and digitization.

The GARFIELD-9 simulation we have carried out suggests that the signal pulse current due to a cosmic muon has a peak of $I_i \approx -3\mu\text{A}$ over a width

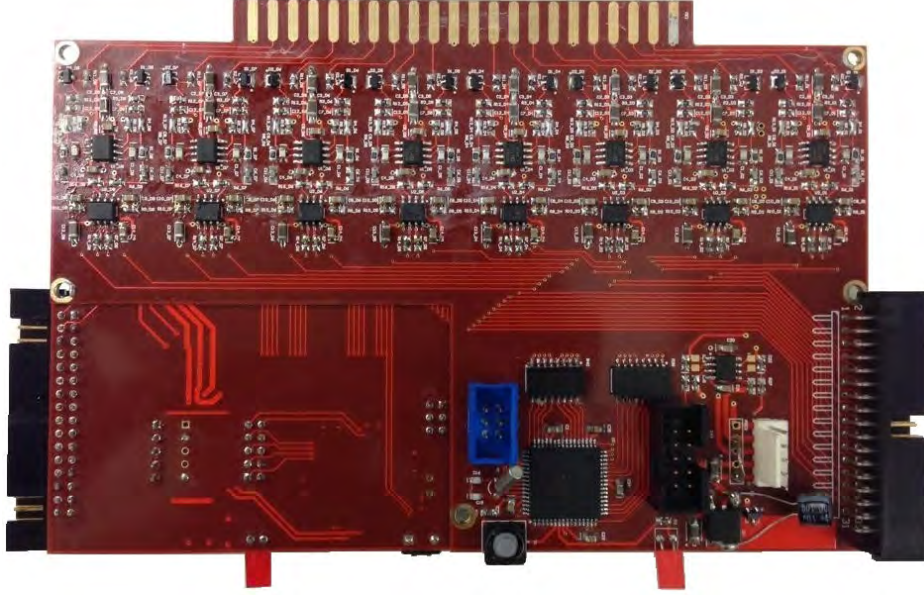


Figure 5.1: A photo of the wire chamber front-end. The upper 8 repeated circuits are the 16 analog channels. The lower-right circuit is the digital front-end.

$T_s \sim 200$ ns. This corresponds to a charge of $Q_i \approx 0.2$ pC.

We employ a charge amplifier with feedback capacitance 1 pF and resistance 1M Ω . This generates an amplified signal up to $\Delta V_o = 3 \times 0.2$ V, which then passes through a high-pass filter damping out the low frequency and DC components. The resultant pulse after filter V_o will enter the comparator. A pulse that passes through the comparator threshold is digitalized and is sent to the back end FPGA.

5.1.2 Pre-Charge Amplifier Circuit

Immediately following the 1 nF protective HV capacitor which connects the anode sensing wires, we installed a $R_2 = 10$ Ω protective resistor. The resistor protects the following diodes and operational amplifier (op-amp) against leakage current at the HV capacitor. It ensures most power is deposited at itself when there is a leakage current in the circuit.

We place a high conductance ultra-fast switching diode, with both outputs connected to ground at D_1 , to protect the analog circuit against large current of

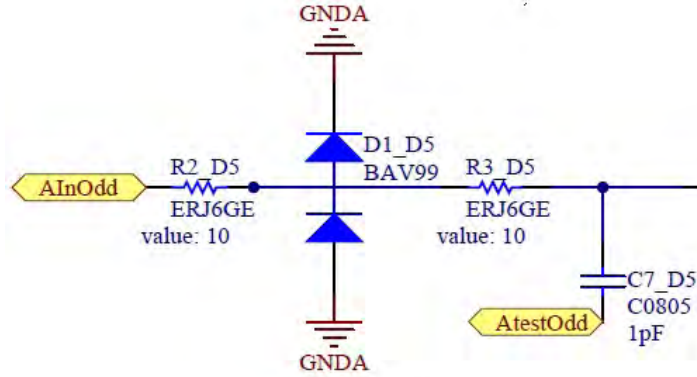


Figure 5.2: The protective circuit of at odd channels.

either directions. The diode has forward voltage ~ 1 V at a few tens of mA and a breakdown voltage of 70V. When a large current of positive or negative sign is injected to the circuit from the chamber, the current is drained to the ground through the protective switching diode.

The second $R_3 = 10\ \Omega$ resistor is a fail-safe protection for the op-amp against any leakage current when the diode and the first resistor both failed. Again, it protects the op-amp by soaking up most of the leakage current power.

Just before the op-amp, an extra test pulse line is routed to one of the two channels in the digital-to-analog converter (DAC) of the microcontroller. It is for the injection of program-defined test pulses to test the readout of each channel. Between the DAC and the Fig. 5.2, we installed an op-amp as a current buffer to provide enough charges for the pulse. The op-amp also inverts the test pulses in order to mimic the negative current signals from the anode wires.

The odd-numbered channels are parallelly connected to the DAC channel 0 while the even-numbered channels are parallelly connected to the DAC channel 1. The use of the different DAC channels in odd and even channels is for the study of the effect of cross-talks between the adjacent channels during readout. When carrying out a cross-talks scan, we turn off one set of the channels and inject test pulses on the other set. We read out the channels without injection pulses to see if they registered any hit. We quantify the level of cross-talk passes

through the threshold by counting the hits on those channels. The detail will be discussed on section 5.2.4 and 5.2.5. The application program will be discussed on section 6.3.1.

5.1.3 Charge Amplification with Operational Amplifier

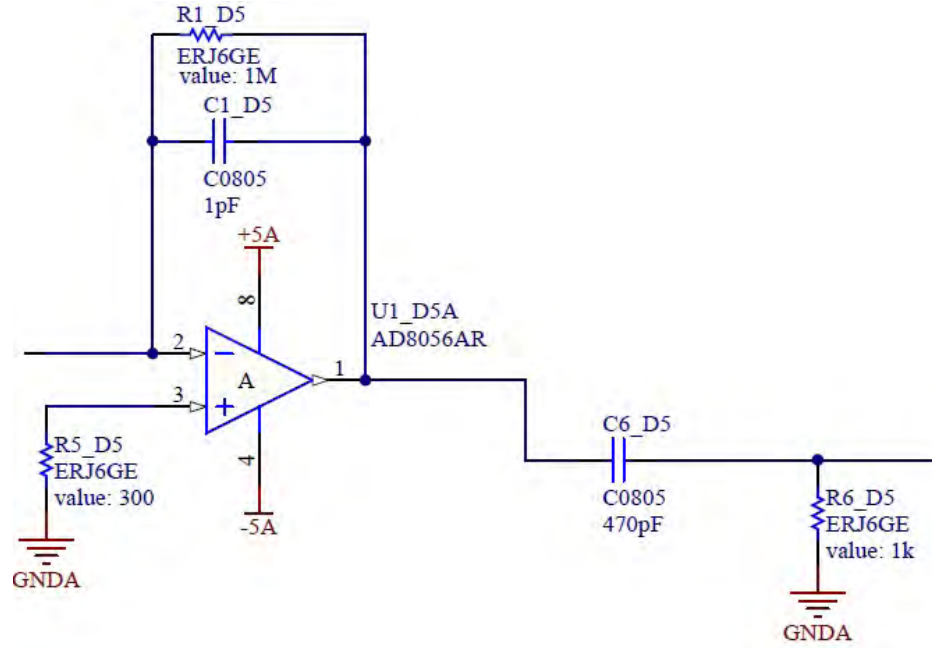


Figure 5.3: The charge amplifier circuit and high-pass filter.

The wire chamber can be viewed as a current source in the front-end design. Hence, the signal amplification can be done naturally by using a charge amplifier. We implement an inverting charge amplifier using an AD8056 dual op-amp operating at ± 5 V. The typical saturation current and voltage swing at ± 2 V are 60 mA and ± 3.1 V respectively. The typical input offset voltage is 3 mV. Each dual op-amp amplifies the charge signals of two adjacent channels. For example, the first op-amp is the amplifier for both channel 0 and channel 1.

The charge amplifier consists of the op-amp, the capacitor C_1 and the resistor R_1 . The feedback capacitor integrates the current signal from the wire to produce a voltage signal $V_s = Q_s/C_1$. At the same time, C_1 is discharged by the feedback

resistor R_1 , with a time constant $R_1C_1 = 1 \mu\text{s}$. It means that the amplifier is also a low-pass filter, which suppresses the signal Fourier components with frequencies $f \gg 1 \text{ MHz}$ (The characteristic signal frequency is 20 MHz, i.e. with a period $T_s = 50 \text{ ns}$). The filter avoids the signal from saturating the op-amp output and suppresses the high frequency noises.

For an ideal calculation, we can approximate the system as an ideal charge amplifier with output voltage described by the Eq. 4.2. The overall signal seen in Fig. 5.4 is a positive pulse with a rise time equal to the signal pulse width T_s , and a fall time with a time constant of $1 \mu\text{s}$. Note that the op-amp has a typical output DC offset of a few hundreds mV, which should be filtered by a subsequent high-pass filter. The output voltage pulse height is about 0.1 V per wire. An example of the actual signal pulse measured by an oscilloscope is shown in Fig. 5.4.

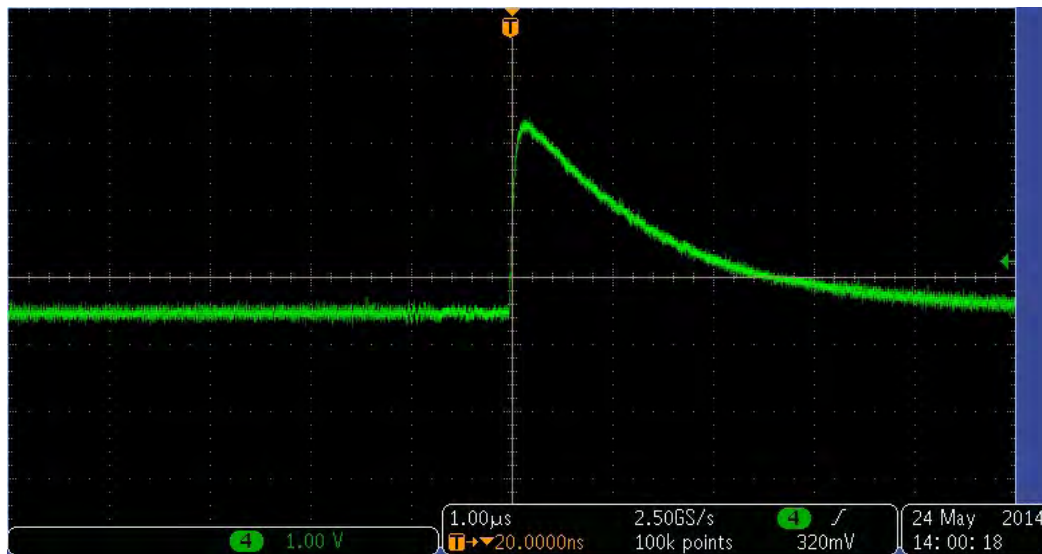


Figure 5.4: A signal pulse shape measured by an oscilloscope just after the op-amp. A -0.3 V op-amp offset and a signal $\Delta V = 3\text{V}$ can be seen.

The two major sources of electromagnetic noises are the 50 Hz noise from household mains electricity and the 38 kHz one from florescent light tubes. We introduce a high-pass filter (C_6 and R_6) with a time constant of 470 ns, which

filters noises of frequencies below 2 MHz. This suppresses the two main environmental noises. It also further shapes the signal pulse by truncating its decay tail width from 1 μs to 470 ns. A typical signal shape can be seen in Fig. 5.5. The DC component of the signal is removed. One feature as a result is that the positive signal peak is followed by a flat undershooting tail.

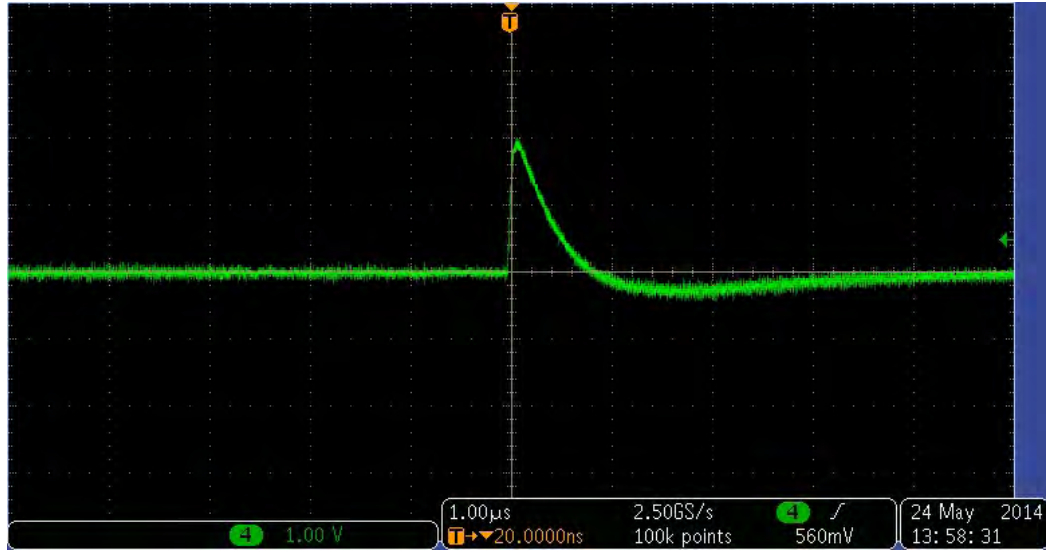


Figure 5.5: A 2V signal pulse shape after passing through the high-pass filter. It is followed by a -0.2V undershooting tail.

5.1.4 Front-end Discriminator

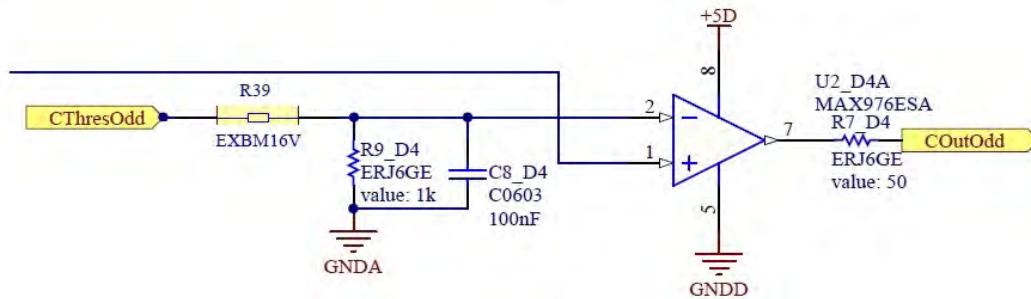


Figure 5.6: The threshold circuit

We employ a dual MAX976ESA high-speed comparator for discriminating the

signal pulses. The positive pin of the comparator is connected to Fig. 5.3 to accept filtered signals. The negative pin is connected to the microcontroller threshold through a low pass filter. The threshold of each channel is generated from a dedicated microcontroller counter channel by pulse width modulation (PWM). The PWM operates in cycles of 2 ms. The percentage of time the PWM outputs 3.3 V “high” is its duty cycle. The PWM has an adjustable duty cycle, of a 2-byte minimum resolution, set by microcontroller. The duty cycle is translated to threshold by the low-pass filter.

The low-pass filter consists of a resistor R_{39} , R_9 and C_8 . R_{39} is a resistor array that delivers 33 k Ω resistance to every channel’s threshold low pass filter. The time constant of the filter is 0.97 μ s with a maximum equivalent output voltage 97 mV. Since the PWM counter cycle is much shorter than the 1 ms time constant, the filter averages out the PWM wave pattern and outputs a time-constant voltage. The threshold is $V_{TH} = \text{duty cycle}(\%) \times 97 \text{ mV}$.

When there are no signals above the threshold, the comparator outputs the ground voltage. Once a signal pulse is above the threshold level, the comparator outputs a +5 V voltage on its output pin until the pulse falls below the threshold again. The comparator digitizes the time-over-threshold (ToT) of the signal. We define a continuous ToT to one signal count in the back-end system. We extract the value of the ToT to increase the spatial resolution of the wire chamber. Since every three sensing wires are soldered together to form a channel, the resolution of the chamber is only 1 cm by just counting the triggered channels. By also reading the signal ToTs, we can interpolate the signal to acquire a spatial resolution of 0.33 mm (the wire separations).

Behind the comparator, the +5 V digital signal pulses are first reduced to +4 V by the resistor R_7 . Then all the 16 signal output channels from the front-end are collected into a 34-pin insulation-displacement connector (IDC34) and are connected to the back-end.

5.2 Digital Front-end

5.2.1 Introduction

The main duties of the digital front-end are to control the front-end signal thresholds, the test pulses and to monitor the internal status of the microcontroller on the front-end.

We installed the Atmel Xmega256A3BAU Microcontroller [34] on the digital part of the front-end. The whole digital circuit is connected to +5V and GND of DC power supply. The voltage is regulated to 3.3V by an MC33269 low dropout voltage regulator. The microcontroller operates at the regulated 3.3V for full utilization of the 32MHz operating frequency. Some of the its features relevant to the wire chamber are listed here:

- An internal 32MHz run-time calibrated and tuneable oscillator;
- Two serial peripheral interfaces (SPI) for communicating with the back-end;
- 256KBytes flash ram and 8KBytes of boot section as non-volatile memory (NVM);
- Seven 16-bit timer/counters (TC); 4 TCs with 4 compare-capture (CC) channels and 2 TCs with two CC channels;
- Two 16-channel analog-to-digital converters (ADC);
- One 2-channel digital-to-analog converter (DAC).

The thresholds are generated by pulse width modulation with the TCs. The ADCs can read back the thresholds and the internal status of the microcontroller, namely the temperature, the microchip 3.3 V input voltage (V_{cc}) and the internal 1.1 V reference bandgap voltage. The test pulses for the threshold scanning are generated by the DAC. Lastly, the communication between the front-end and the back-end is done by an SPI module in the microcontroller.

5.2.2 SPI Communication between Back-end and Front-end

To control the front-end from the back-end, we need a simple, high speed communication protocol. This communication requirements are not only for slow controls such as setting threshold or reading the microcontroller voltage. Iterative test such as the threshold scan requires both speed and robustness of the communication. We employ the Serial Peripheral Interface (SPI) as the communication standard between the back-end and front-ends. It is a standard that is compatible with our microcontroller, and also faster and simpler than other standards such as I2C.

The SPI is a synchronous serial data transmission standard operated in full duplex with master/slave mode. The back-end acts as a master and initiates the data transmission with multiple front-ends. We implemented a $(4 + 2)$ serial bus scheme in our protocol, as oppose to the standard 4-wire bus with serial clock (SCLK), slave select (SS), Master-In-Slave-Out (MISO) and Slave-In-Master-Out (MOSI). The two additional wires are a 2-bit link transmitting the address of the front-end being addressed to, in order to avoid saturating the data output available in the FPGA board of the back-end.

The 3 back-end master FPGAs communicate with the 12 front-end microcontrollers. It means each back-end has to talk to at least 4 front-ends. Each front-end is assigned to a unique front-end address (0-3) among the four front-ends. For each back-end to select which front-end is being addressed to, we deploy a two-bit Front-End Address (A_{FE}) line parallelly connected to the 4 front-ends. The back-end addresses a specific front-end by pulling the A_{FE} address line's 2 bits to the corresponding address value. The front-end microcontroller only listens the SPI MOSI record when it reads the address that matches its own front-end address stored in the NVM.

We define a data frame in Tab. 5.1, named a record, as a unit of data trans-

bit #	0	1	2	3	4	5	6	7
-------	---	---	---	---	---	---	---	---

MOSI	header (record address)							
	payload byte 1							
	payload byte 2							
	⋮							
	payload byte n							

MISO	0	0	0	0	0	0	0	0
	payload byte 1							
	payload byte 2							
	⋮							
	payload byte n							

Table 5.1: The frame structure of a record.

mission in the SPI standard. Each record starts with a 8 bits header, named record address, which describes the function of the record. Then it is followed by n-byte data payload. The record is exchanged between master and slave through MOSI and MISO in the SPI bus. Note that MOSI outputs data half a clock cycle, defined by SCLK, before MISO. Since the back-end is the master of the SPI, only the record from the master in MOSI will contain the header. The header in MISO from the slave is replaced by a dummy 8-bit zero.

The list of all records is in the Appendix B for reference.

Here we describe one SPI record exchange procedure. Originally, both the master back-end and slave front-end are idle, which means \overline{SS} is low and both MOSI and MISO output zeros. The back-end master initiates the transmission by putting the one-byte header onto MOSI and reads one byte from MISO, accompanied by pulling high \overline{SS} and setting the correct address in A_{FE} . The header instructs the front-end the type of payload in the following bytes of the record and what data it should return to the back-end. Since the front end has not yet

process any data from the back end in this clock cycle, the back-end will read a 8-bit zero from MISO.

After one transfer cycle, the back-end prepares the first payload byte in MOSI, which will deliver further instruction/data to the front-end (e.g. the PWM value of channel 0 for setting the threshold). The front-end has now processed the header in MOSI in the previous transfer cycle, and is ready to put the first byte of payload in MISO according to the header instruction (e.g. the first byte of the 11-byte microcontroller serial number if the header instruction is “to read microchip’s serial number”).

Just before the transfer cycle advances to the next one, the first byte of payload data exchange between master and slave is completed, and both master and slave prepare the second byte of payload to exchange. This continues until all payload bytes are exchanged. The number of bytes to be exchanged is also specified in the record address in the header. If either the master or the slave has no byte to deliver to the other side but the record is not yet finished, a dummy payload of 8-bits zero are put into MOSI or MISO respectively.

When the transfer is finished, the master and slave returns to idle state with both MOSI and MISO output zeros and \overline{SS} .

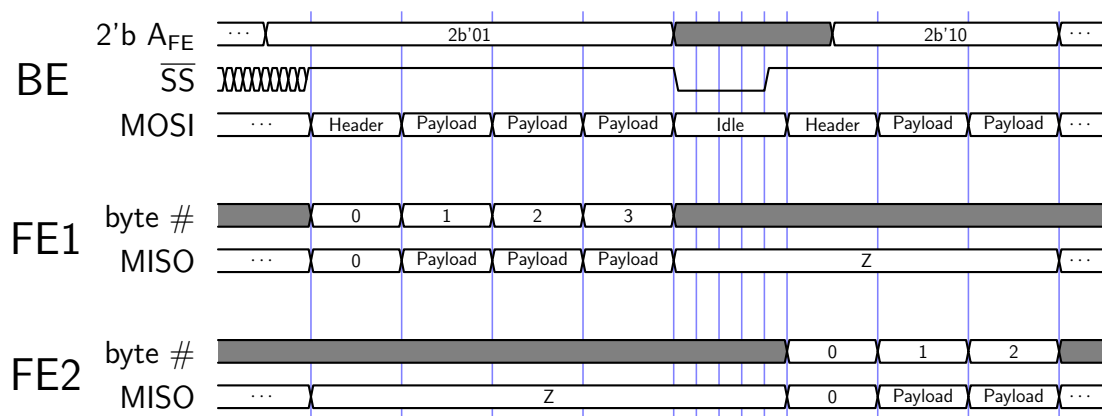


Figure 5.7: An SPI timing diagram. Example of back-end communicating with two front-ends with SPI, first FE 1 then FE 2.

5.2.3 Assignment of Front-end Address with the Action Button Code

To compensate the lack of a slave address in the SPI standard, we introduce the Action Button Code (ABC) for encoding an address into the front-end microcontroller by a single digital channel. The front-end has an LED and a button as an human interface. The user can switch the front-end between the operation mode in which the front-end takes data, and address programming mode in which the user can input the address manually.

The front-end is by default in operation mode after startup. By continuing pressing the button for approximately 2 seconds, the front-end microcontroller switches from the operation mode to address programming mode, indicated by the a change of state in the LED. In the address programming mode, the front-end translates the number of short clicks on the button as the address number of the front-end. The maximum address value is 254. The user can switch back to the operation mode by another 2-second pressing of the button. Then the address is stored into the NVM of the microcontroller. The user can review the address by short clicking the button once while the front-end is in the operation mode. The address number will be displayed as the number of LED flashes. The addressing display can be terminated by pressing the button for a moderate length of time.

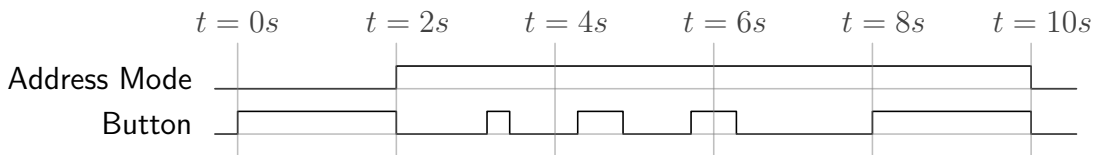


Figure 5.8: An ABC timing diagram. Address "3" is programmed into the front-end.

The front-end address is read from the flash ram every time after power start up or after address programming. The microcontroller makes use of the address to selectively listen to the SPI signals from the back-end. It listens to the SPI

channel whenever the address line A_{FE} matches the internal front-end address.

5.2.4 Threshold Generation and Scanning

The aim of a signal threshold is to reduce the noise pickup from the analog signal channels. When there are no signals on a sensing wire, the voltage level on the channel still fluctuates due to the electromagnetic and thermal noises. Nonetheless, the voltage fluctuations by the noises should be, on average, smaller than the signal (from the environmental radiations or the cosmic rays) pulse levels if the multiplication factor of the wire chamber and the front-end charge amplifiers are set right. In general, the noise levels are different from channel to channel. We need to set a threshold for each individual wire channel.

We generate the thresholds by pulse width modulation (PWM) using the comparator channels of the 16-bit TCs in the microcontroller. The TCs count from 0 to 2^{16} with a pre-scaled frequency from the internal clock. The TC channels output high and low voltage alternatively in a TC cycle. The percentage duration of outputting high in one TC cycle is the duty cycle of the PWM. Outside the duty cycle, the channels output low. Each oscillating output of a TC is passed through a low-pass filter, which filters out the AC component of the output. The remaining DC voltage is sent to a comparator as the front-end threshold. The details are discussed in the previous Section 5.1.4.

The clock pre-scalings, frequencies and the duty cycles of the PWM can be set by the microcontroller. The PWM duty cycle is stored in the microcontroller's NVM and can be updated in real-time by the back-end through an SPI transmission. The record responsible for writing the PWM duty cycle is in Table B.1. The duty cycle settings in the microcontroller RAM can also be read back by the back-end according to the SPI record in Table B.2.

The channel 14 and channel 15 thresholds are fed back to the ADC1 and the ADC2 channels respectively, such that the microcontroller can monitor the realistic threshold electrical outputs when the wire chamber is in operation (Ta-

ble B.7).

In addition, the ADC can monitor the internal status of the microcontroller (Table B.4), discussed in Section 5.2.1.

To set an appropriate threshold, we need to optimize the signal-to-noise ratio by scanning the threshold values. A threshold scan is carried out, with the wire chamber operating, by sweeping the threshold of a channel from 0 to its maximum value, recording the signal counts with each threshold value along the way. When the threshold is exactly or close to 0, the channel is dominated by the noises. The count rate is saturated since the tiniest fluctuation of the voltage is digitized by the discriminator. As we tune up the threshold, the digital output of the channel switches from noise-dominated to signal-dominated. The change happens when the threshold voltage is equal to the average voltage of the noises. This voltage level is also the target threshold voltage, since it presents a threshold of a high stochastic noise-suppression without sacrificing the signal efficiency.

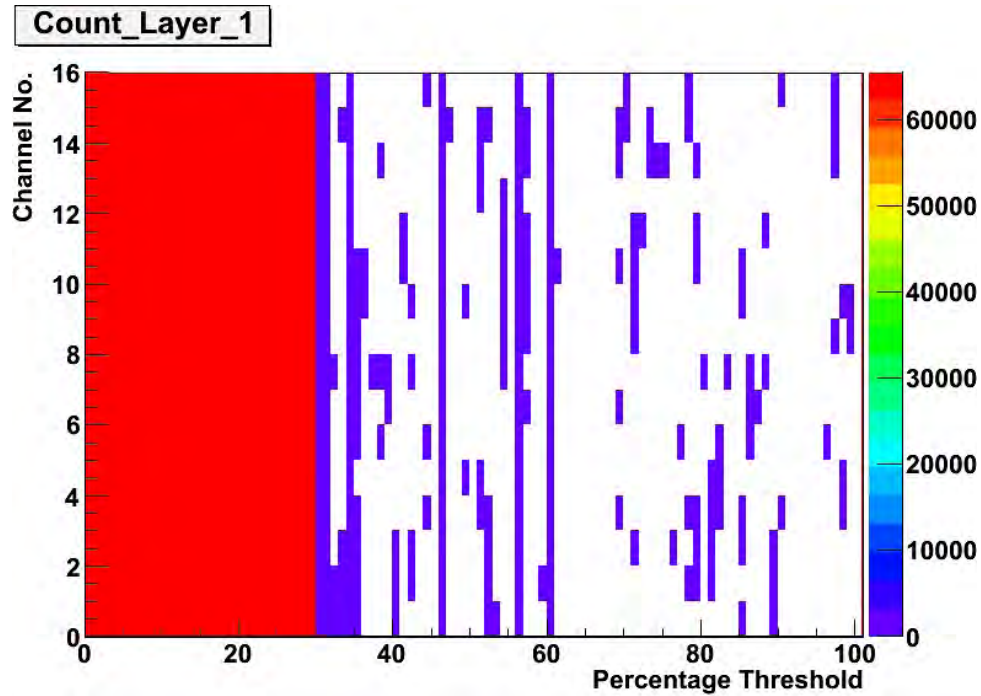


Figure 5.9: A result plot of a threshold scan on the front-end 1 showing the singles counts as a function of the channel number and threshold voltage step.

5.2.5 Analog Injection Test and Cross-talk Scan

To ensure that each channel on both the analog and digital front-end is functioning properly, we set up a way to inject voltage pulses to the pre-amplifier circuit. The idea of the analog injection test is to inject a known number of test pulses with well-defined shape into the front-end signal inputs. The front-end cannot distinguish between the test pulses and the actual signals once the test pulses are injected to the signal channels. The test pulses, like every real signal, pass through most parts of the analog circuits and all the digital circuits, including the digital front-end, back-end and DAQ software. The back-end and the DAQ software count the test pulses as if they are real signals.

Since we know the number of test pulses beforehand, we can easily know whether the whole wire chamber system has under-counted or over-counted the pulses by simply comparing the number of test pulses we set on the microcontroller with the total counts read from the software output. This way we can identify the count-related bugs in the front-end design, front-end soldering, back-end firmware programming and software programming. We can also identify the source of the problem, whether it is located inside the gas volume, electronics, or programs, when there are channels with abnormal efficiencies.

An injection pulse is generated by the DAC of the microcontroller. There are two channels in the DAC, the DAC channel 0 is connected to the odd-numbered signal channels and the DAC channel 1 is connected to the even-numbered signal channels. The DAC outputs voltages between a maximum 1 V and a minimum 0 V (usually with an offset of a few 10s mV) with a 0.244 mV (12-bit) linear resolution. The DAC can change its output voltages at a rate of ~ 1 MHz. Each test pulse is defined by 3 sampling points. For example, if the 3 sampling voltages are 0 V, 0.5 V and 0 V respectively, the output pulse shape will start with the ground voltage, followed by a voltage step of 0.5 V, and then to the ground again (shown in the Fig. 5.10). The pulse duration will be 3 μ s. The DAC pulses are

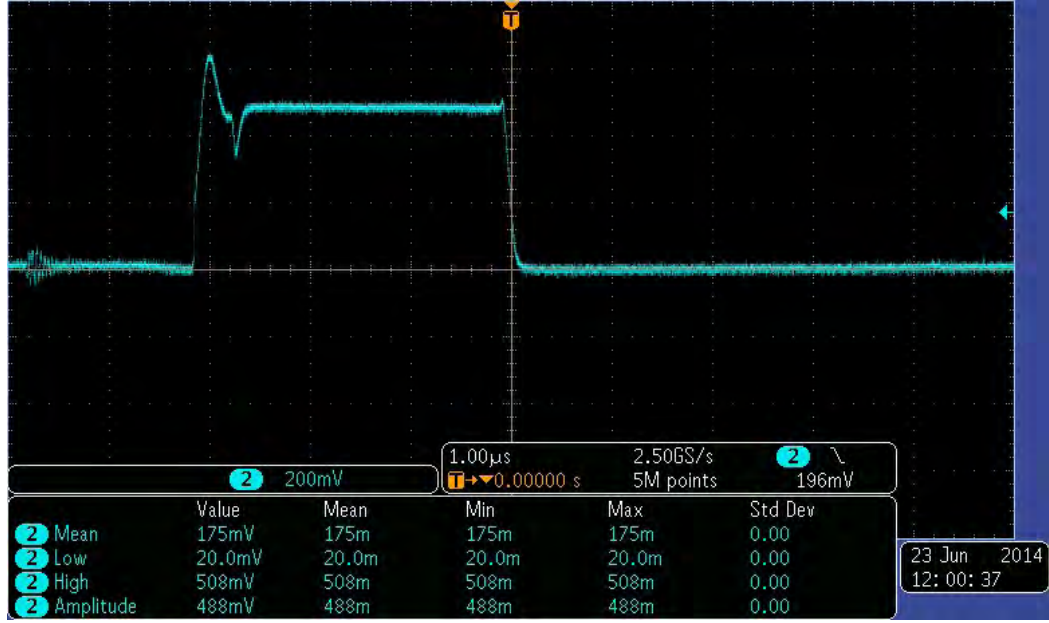


Figure 5.10: A test pulse generated by the DAC.

triggered by the SPI frames sent from the back-end, defined in the Table B.5 for the DAC channel 0 and Table B.6 for the DAC channel 1. Each of the two SPI frames contains 6-byte of payload describing the voltages of the three sampling points. We can send a fixed number of test pulses by sending an equal number of DAC SPI records to the microcontroller.

Another scan related to the test pulses is the cross-talk scan. Apart from the sensing wires cross-talks discussed in the section 4.4.3, there is also a probability that there are cross-talks between the printed circuits of the analog front-end. A front-end cross-talk can occur if the circuit separations are too small or the signal currents are exceedingly large. We examine the magnitude of the cross-talk by a test pulse-based cross-talk scan.

When we inject test pulses onto a channel, we can read out the adjacent un-injected channels. Ideally, the un-injected channels will read 0 counts since there are no signals. If there is a front-end cross-talk, the un-injected channels will read non-zero counts because of the induction by the test pulses on the adjacent channel.

The cross-talk scan is implemented on the wire chamber by the two DAC channels. We carry out the scan by injecting pulses only with the DAC channel 0 onto the odd-numbered channels, while we inspect the even-numbered channels for the cross-talk counts, and vice versa for the DAC channel 1 onto the even-numbered channels. We can study the properties of the cross-talks on every other channel as functions of the pulse height, pulse duration and threshold value by scanning through those values in the cross-talk scan.

Chapter 6

Back-end and Data Acquisition Software

6.1 Introduction

Before the analysis on the wire chamber data can be done, the last step of the data processing takes place at the back-end field-programmable gate array (FPGA) and the data acquisition (DAQ) computer software. We have to devise a DAQ chain, from the back-end to the software, that reduces the amount of data and limits them to those of user's interest.

The back-end FPGA controls the communication between the front-ends and the DAQ computer. It translates back-and-forth between the SPI data from the front-end microcontrollers and the computer USB data. The back-end also generates “events” data packets for the computer from the front-end discriminator signals.

We use a Xilinx Virtex 5 LX50T-FFG1136 [47] FPGA on a Digilent Genesys board [48] as the back-end. Some of its features are

- an 100 MHz operation frequency,
- a universal serial bus (USB) hub connected to the DAQ computer for data

transmission,

- two very-high-density cable (VHDC) connectors connected to a break-out daughter board, which in turn connects to at most 4 front-ends for picking up the digital wire signals.
- four 6×2 right-angled, 100-mil connectors linked to the 4 front-ends for the SPI communication and the front-end address transfer.

The back-end also has multiple first-in first-out (FIFO) buffers programmed to temporarily store the data and signals from both the front-ends and the computer. Logics are programmed into the back-end firmware to implement various masks and coincidence strategies.

The DAQ software is installed on a Scientific Linux machine. The DAQ computer is linked to the back-end through a USB cable. The USB data transfer format is encapsulated in a Genesys library supplied by Digilent, Inc. The software communicates with the back-end by writing and reading the different registers inside the back-end FPGA.

The DAQ software conveys slow control commands to the back-end, which either configure the back-end or the front-ends. For example, the software can order one front-end to output a certain value of thresholds and the back-end to set a specific coincidence mask. The software also accepts data from the back-end when the software demands reading certain output registers. The returned data packets, depending on the register types, can be interpreted as the singles rates, the events, etc. The software generates an output ASCII data file with these data packets. Further conversion of the data file to the ROOT format can be done with some auxiliary programs.

6.2 FPGA Back-end Module

6.2.1 Inter-module Communication

The back-end controls the communication between the DAQ computer and the front-end. The back-end FPGA provides a list of registers for the DAQ software to access through a USB link. The DAQ instructs the back-end which register it is going to access by using a list of register addresses, defined in Table C.1 and Table C.2.

For instance, when the DAQ computer writes commands onto the input registers of the FPGA, the back-end recognizes a change of the register states. It then performs the actions corresponding to the needs of the software. Similarly, when the back-end has data which are interesting to the DAQ software, it writes the data onto the respective output registers. The DAQ computer reads the output register when the software asks for the corresponding data. Since the FPGA does not know when the back-end software wants to read the output registers, the output registers with high data rates are usually buffered to prevent overwriting. This is the case for the event output register for example.

As for the front-end communication, the back-end FPGA is the master of the SPI. The FPGA only generates the required timing and logic for the SPI framing. It is ignorant of the data content of the SPI messages.

The DAQ initiates an SPI message. The SPI data payloads are composed by the DAQ software, which writes the data to the “write SPI register”. The back-end extracts the payloads from the register. It then generates the corresponding data frame and sends it to the front-end. The DAQ can also demand the front-end to return data by writing the register with some specific SPI frames, such as the one in Table B.2. This time, the front-end microcontroller generates the SPI payloads. The back-end sends the DAQ SPI frame, at the same time samples the SPI lines for the payloads from the digital front-end. The back-end then places the received front-end SPI message onto the “read SPI register”. The

DAQ computer samples the bytes on that register when the software requires it to do so.

More details on the SPI communication strategy between the front-ends and back-end can be found in section 5.2.2.

The sensing wire digital signals are routed from the analog front-end discriminators to the back-end 68-pin VHDC inputs. The back-end has two VHDC connector inputs and has to connect to 4 front-ends. Kwan has designed a break-out board which maps the 4×34 signal outputs of the front-ends (from four IDC34 sockets) to the 2×68 signal inputs of the back-end (to two VHDC connectors). The break-out board is designed to be mounted on the back-end.



Figure 6.1: The break-out daughter board that supports connection to at most 4 front-ends. Two red LCDs (DV_{CC}) are for displaying the supply voltage. The four LCDs on the right (DFE) are for displaying the signal LayerOR of their respective connectors.

The signals are then processed by the FPGA to generate either the event packets or singles rates.

6.2.2 Event Builder

The sensing wire signals from the front-end outputs are in the form of digital +4 V voltage steps. The voltage step rises when the analog signal rises above the threshold voltage set by the front-end microcontroller. Similar, the voltage of the output drops back to the ground when the analog wire signals fall below the threshold voltage. The width of the steps is called the time-over-threshold (ToT). We want to extract three pieces of information, namely, the time when the signal rises, the ToT of the signal and which of the other channels output signals at nearly the same moment (i.e. the coincidence).

The signal lines from the wire chamber are sampled every 10 ns. Once a rising edge is detected, the time is recorded by a 4-byte time stamp generated from a 32-bit counter (counter overflow period is about 42.95 seconds). The time stamp records the time since the last time the counter overflows or the back-end starts up/restarts, in units of 10 ns.

The ToT is an one byte per channel data that can range from 0 ns to 2550 ns. When the back-end detects a signal from a channel, the FPGA time is stamped and the back-end starts counting the pulse width (ToT) of the signal when the signal voltage remains high. At the same time, the back-end also waits for the outputs from the other channels.

Within a signal time window set by the DAQ software, all channels which have signals output are acknowledged as coincidence and their ToTs are also counted. After the signal time window has passed, any additional signal rising edge is neglected, but the back-end is still counting the ToTs for the signals which are acknowledged previously within the time window.

When a 2560 ns maximum ToT wait time has passed, the ToT countings are stopped and the ToTs are stored as the output signal ToTs. Then, the back-end returns to its original state and waits for a new signal to trigger the coincidence. The back-end has a FIFO to buffer at most 3 consecutive events.

The back-end reads out those channels which are not channel-masked by the DAQ. A coincidence event read-out also depends on the coincidence mask. If a set of signals have passed through both the channel mask and coincidence mask, an event packet is constructed and is output to the DAQ computer. An event is a 70 byte data packet containing the 4-byte event start time stamp, the 1-byte ToTs for each of the 16 channels of the 4 front-ends and a 2-byte footer which ensures the integrity of the data packet. The structure is shown in the Table 6.1.

The event structure contains the important information required to study various physics, such as the cosmic muon east-west effect. It is because, by proper settings, that the events are less susceptible to the background radiation signals by the virtue of a multi-layer coincidence with the coincidence mask.

bit #	0	1	2	3	4	5	6	7
-------	---	---	---	---	---	---	---	---

Time Stamp	Time Stamp Byte 0							
	Time Stamp Byte 1							
	Time Stamp Byte 2							
	Time Stamp Byte 3							
FE 0	Ch0	Ch1	Ch2	Ch3	Ch4	Ch5	Ch6	Ch7
TOT	Ch8	Ch9	Ch10	Ch11	Ch12	Ch13	Ch14	Ch15
FE 1	Ch0	Ch1	Ch2	Ch3	Ch4	Ch5	Ch6	Ch7
TOT	Ch8	Ch9	Ch10	Ch11	Ch12	Ch13	Ch14	Ch15
FE 2	Ch0	Ch1	Ch2	Ch3	Ch4	Ch5	Ch6	Ch7
TOT	Ch8	Ch9	Ch10	Ch11	Ch12	Ch13	Ch14	Ch15
FE 3	Ch0	Ch1	Ch2	Ch3	Ch4	Ch5	Ch6	Ch7
TOT	Ch8	Ch9	Ch10	Ch11	Ch12	Ch13	Ch14	Ch15
Footer	1	1	1	1	1	1	1	1
	0	0	0	0	0	0	0	0

Table 6.1: The 70-byte frame structure of an event.

We implement a coincidence mask on the event triggering. Since each front-end controls a layer of gas gap, we identify a front-end as a layer of 16 wire channels. Hence for one back-end, there are four “LayerOr” logics, or “layers”, one for each gas gap. A LayerOr logic indicates that there is a signal in any one of the 16 channels at a layer.

The coincidence mask is a 16-bit logic combination of the 4 LayerOrs. Each of the 16 bits represents a basis in the all-possible-coincidence-masks space. With 4 maximum signal layers, there are one 0-out-of-all, four 1-out-of-all, six 2-out-of-all, four 3-out-of-all and one four-out-of-all coincidence combinations. Table 6.2 is a map between the coincidence logic bases and their register bit values.

Coincidence Mask Register		LayerOR				N-out-of-four
base-16	base-2	Layer 3	Layer 2	Layer 1	Layer 0	
0x0001	0000 0000 0000 0001	0	0	0	0	0
0x0002	0000 0000 0000 0010	0	0	0	1	1
0x0004	0000 0000 0000 0100	0	0	1	0	1
0x0008	0000 0000 0000 1000	0	0	1	1	2
0x0010	0000 0000 0001 0000	0	1	0	0	1
0x0020	0000 0000 0010 0000	0	1	0	1	2
0x0040	0000 0000 0100 0000	0	1	1	0	2
0x0080	0000 0000 1000 0000	0	1	1	1	3
0x0100	0000 0001 0000 0000	1	0	0	0	1
0x0200	0000 0010 0000 0010	1	0	0	1	2
0x0400	0000 0100 0000 0000	1	0	1	0	2
0x0800	0000 1000 0000 0000	1	0	1	1	3
0x1000	0001 0000 0000 0000	1	1	0	0	2
0x2000	0010 0000 0000 0000	1	1	0	1	3
0x4000	0100 0000 0000 0000	1	1	1	0	3
0x8000	1000 0000 0000 0000	1	1	1	1	4

Table 6.2: The table of register values for the coincidence mask basis.

With the 16 LayerOr bases, we form more complicated coincidence masks by

the OR-combinations of the mask bases. For example, if we want the back-end to trigger on an event whenever exactly one layer has signals, we can join the four 1-out-of-all with the “OR” operator. Hence the 1-out-of-all coincidence mask is

$$\begin{aligned} 0x0002 \text{ or } 0x0004 \text{ or } 0x0010 \text{ or } 0x0100 &= 0x0002 + 0x0004 + 0x0010 + 0x0100 \\ &= 0x0116 , \end{aligned} \tag{6.1}$$

or equivalently in binary, 0000 0000 0001 1110.

Similarly, the 2-out-of-all coincidence mask is 0x1668. The 3-out-of-all coincidence mask is 0x6880 and 4-out-of-all is 0x8000. If we want to trigger both on 3-out-of-all events and 4-out-of-all events, the mask will be $0x6880 + 0x8000 = 0xE880$. The masks of triggering on the events that have signals from the 0/1/2/3-layer will be 0xAAAA / 0xEEEE / 0xF0F0 / 0xFF00 respectively. The value for a more exotic coincidence mask can be determined by the mask register’s boolean algebra.

6.2.3 Singles Rate

Apart from sending out the signals event by event, the back-end also outputs the total count rate of the channels by a singles rate structure. The count rate ignores the ToT and coincidence information and only stores information about the number of counts over a period of time. The singles rate frame (shown in Table 6.3) consists of the start time stamp, the end time stamp and the total count of each channel in the time during the two time stamps. The 2-byte count data corresponds to a maximum total single count of 65535 per channel. The actual count rate within the designated time span can be easily generated by the software with

$$\text{Count rate} = \frac{\text{Count}}{\text{End Time} - \text{Start Time}} . \tag{6.2}$$

If the singles rate duration is shorter than the time stamp counter overflow time, the start time and the end time are just the time stamps multiplied by the 10 ns

counter clock rate. Otherwise, the DAQ computer unix time should also be taken into account. The singles rate is helpful for estimation of both the total signal

bit #	0	1	2	3	4	5	6	7	8	9	10	11	12	13	14	15
-------	---	---	---	---	---	---	---	---	---	---	----	----	----	----	----	----

Start	Time Stamp Byte 0				Time Stamp Byte 1			
Time	Time Stamp Byte 2				Time Stamp Byte 3			
FE 0	Ch 0	Ch 1	Ch 2	Ch 3	Ch 4	Ch 5	Ch 6	Ch 7
Counts	Ch 8	Ch 9	Ch 10	Ch 11	Ch 12	Ch 13	Ch 14	Ch 15
FE 1	Ch 0	Ch 1	Ch 2	Ch 3	Ch 4	Ch 5	Ch 6	Ch 7
Counts	Ch 8	Ch 9	Ch 10	Ch 11	Ch 12	Ch 13	Ch 14	Ch 15
FE 2	Ch 0	Ch 1	Ch 2	Ch 3	Ch 4	Ch 5	Ch 6	Ch 7
Counts	Ch 8	Ch 9	Ch 10	Ch 11	Ch 12	Ch 13	Ch 14	Ch 15
FE 3	Ch 0	Ch 1	Ch 2	Ch 3	Ch 4	Ch 5	Ch 6	Ch 7
Counts	Ch 8	Ch 9	Ch 10	Ch 11	Ch 12	Ch 13	Ch 14	Ch 15
End	Time Stamp Byte 0				Time Stamp Byte 1			
Time	Time Stamp Byte 2				Time Stamp Byte 3			

Table 6.3: The 136-byte frame structure of a single rate.

rate and the total noise rate, depending on the threshold level. The signal rate can be used to monitor the background radiation level fluctuations when we carry out a long period data-taking. The noise rate is essential for the noise-related front-end scans, such as the threshold scan and the cross-talk scan.

6.3 DAQ Software

The DAQ software is a program that operates on a computer with a Scientific Linux operating system installed. The program communicates with the back-end by writing and reading the back-end registers in the Table C.1 and the Table C.2.

The purpose of the software is to, firstly, interface with the user to determine

the required data-taking strategies. Secondly, it translates the user's commands to the back-end registers' bits, and orders the back-end and front-ends to carry out the required operations by writing the bits onto the back-end input registers. After a while, the software reads the back-end output registers for the signal data. The software translates the data to a human-readable format and writes them onto a data file. Using their own strategies, the users can read the output data files directly or convert them to ROOT files to analyze the result.

We list the threshold scan and the data-taking program as two examples.

6.3.1 Threshold Scan Program

The threshold scan is a program to measure the channel singles rate against the front-end threshold value. A description for the meaning of the threshold scan can be found in 5.2.4.

The program first gets the back-end FPGA device handle using the Genesys driver, such that it can communicate with the back-end. After initializing the chamber with the appropriate input masks, the program enters a for-loop for the threshold scanning.

In each step of the for-loop, the software issues an SPI record to adjust the PWM duty cycles of the front-end threshold generators. The threshold voltages increase linearly from one step to another during the iteration cycle. The software asks for the SPI returns of the ADC thresholds read-back and the RAM PWM values in each step. This is to ensure that the thresholds are indeed set correctly. Along the way, the software reads the back-end error vector registers to identify whether there are errors during the operations. Most importantly, the software reads the back-end singles rates register near the end of each step.

The scan steps, the start time stamp, the end time stamp, the ADC values, the RAM PWM values, and the singles rates are written onto the output data file. The device handle is released once the program ends.

The user can plot the singles rates against the thresholds value to study the

noise/signal rate behavior of each channel as a function of the threshold voltages. One of the wire layer scan results can be found in Fig. 5.9.

The analog injection test and the cross-talk scan are executed in similar ways. The additional features are that in each step of the scan loop, the software also issues an SPI record to initiate the DAC test pulses. The user can set the number and the shape of the DAC pulses beforehand. After writing the output data file, the user can check whether the singles rate or the event readings are as expected given the test pulse settings.

6.3.2 Take Data Program

The scan programs mentioned above run in a small time-scale, usually in less than a few minutes or at most a few hours. When we want to measure events from the cosmic rays, the software needs a much longer time to acquire enough statistics such that physicists can extract useful physics content from the data. The data-taking period can be a few days, weeks or even months.

The data-taking program runs a long duration of time specified by the user. After an initialization with the appropriate input masks, coincidence masks and threshold values, the program spends most of the time reading out events. It can occasionally check the various front-end status, e.g. the temperature, V_{cc} , thresholds and singles rates. It keeps track of the time by reading the system unix time. The program writes the unix time, the time stamp and the ToTs of each channels to the output data file. When the unix time reaches the user designated time, the program ends and the device handle is released.

One obvious use of the data is to plot the time series of the N-out-of-all coincidence data, using the unix time output and the channel ToTs. More advanced use such as particle track-fitting can be implemented when there are multiple wire chambers. The specific uses of the data are easily elaborated based on the raw data file format.

Chapter 7

SEABAS DAQ for ATLAS Pixel Front-end Read-out

7.1 Introduction

7.1.1 Overview of the Large Hadron Collider

The Large Hadron Collider (LHC) [49] at CERN is a 27 kilometer circumference hadron-hadron collider. It is a synchrotron accelerator-collider lying on the Franco-Swiss border. As of the LHC Run 1 in 2012, its luminosity is $L \approx 7.5 \times 10^{33} \text{ cm}^{-2} \text{ s}^{-1}$ and collision rate is 20 MHz (50 ns per bunch crossing). Its proton-proton collision center-of-mass energy is $\sqrt{s} = 8 \text{ TeV}$.

The LHC is upgraded to its design operation values in the phase-0 upgrade during the long shutdown 1 (LS1) from 2013 to 2014. The target luminosity and energy are $L = 10^{34} \text{ cm}^{-2} \text{ s}^{-1}$ and $\sqrt{s} = 14 \text{ TeV}$ respectively. The bunch spacing is further reduced to 25 ns. The LHC run in 2015 steps deeper into the electroweak energy scale and is planned to deliver over 100 fb^{-1} of data, which give greater hope for discoveries beyond the Standard Model of particle physics.

There are 4 large detector experiments at the proton collision sites of the LHC. The LHCb experiment [50] investigates the CP-violation phenomena. The

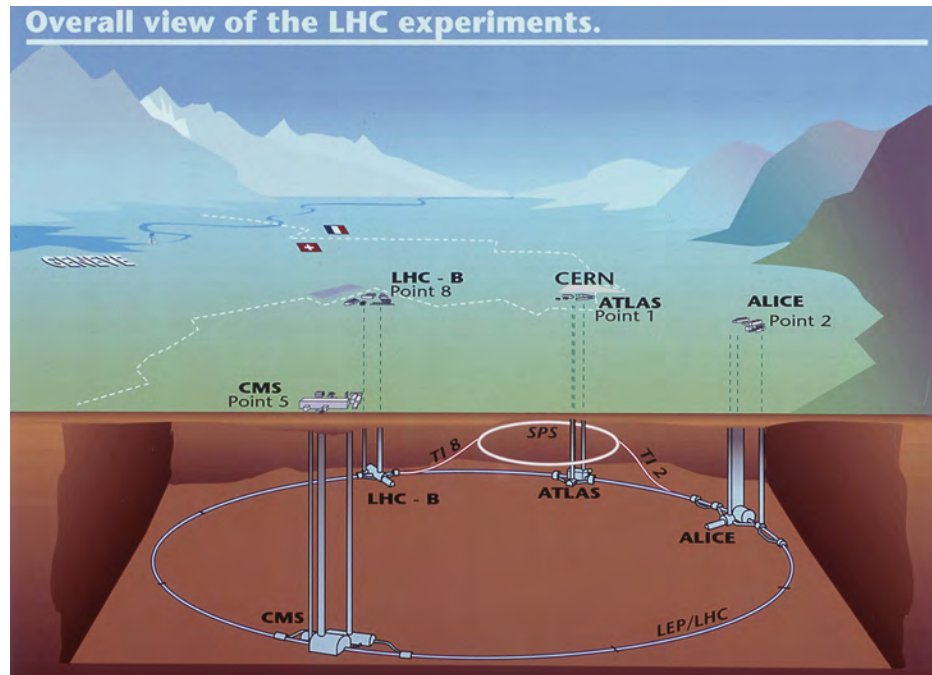


Figure 7.1: The Large Hadron Collider and the four main experiments. Picture is taken from CERN.

ALICE experiment [51] examines the QCD properties of quark-gluon plasma in heavy-ion collisions. The CMS [52] and ATLAS experiments [3] are two general purpose detectors. Their purposes include the study of the electroweak sector, precision tests of the Standard Model, searches for supersymmetry, dark matter and exotica, etc.

One of the achievements of the ATLAS and CMS experiments is the joint discovery in July 2012 [53, 54] of the long-sought elementary particle in the Standard Model - the Higgs boson. The discovery of the Higgs boson confirms the electroweak theory in the Standard Model and the Brout-Englert-Higgs spontaneous symmetry breaking mechanism [55, 56, 57]. This discovery becomes the greatest breakthrough in the particle physics community in recent decades.

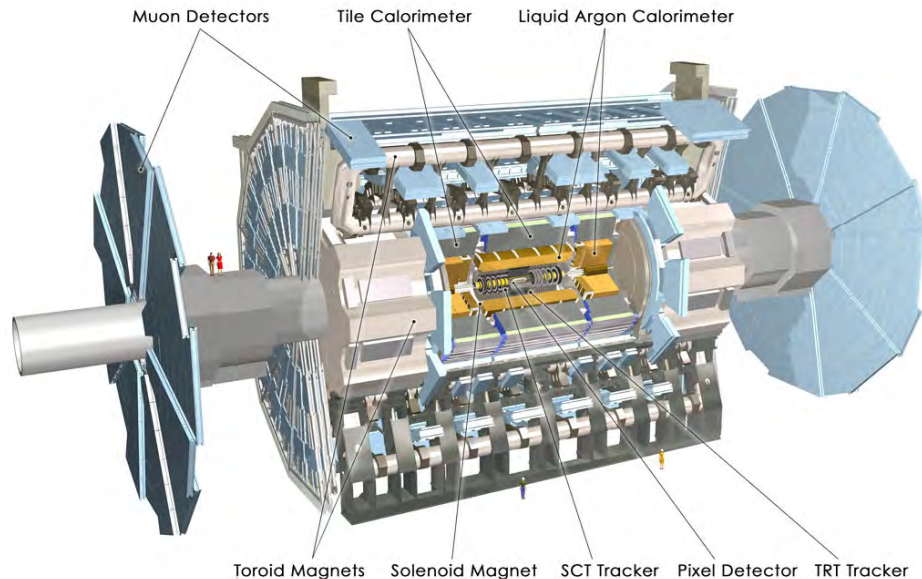


Figure 7.2: The structure of the ATLAS detector, revealing its inner detector, calorimeters, magnet system and muon spectrometer. Picture is taken from the ATLAS collaboration.

7.1.2 Overview of the ATLAS Experiment

The ATLAS (A Toroidal LHC ApparatuS) experiment is the largest detector in the LHC experiments, with length 46 m, diameter 25 m and weight over 7000 tonnes. It is located in a cavern 100 m underground near the CERN Meyrin site. From March 2010 to November 2012, it has collected over 25 fb^{-1} of pp collision data at $\sqrt{s} = 7$ and 8 TeV.

The detector consists of 4 main systems, shown in Fig. 7.2. The inner detector is the innermost system, which measures the momenta and tracks of charged particles. The calorimeters measure the energies of EM particles, hadrons and jets. The muon system identifies and measures the momenta of muons. The magnet system generates a solenoid magnetic field in the inner detector and a toroidal field in the outer detector. The multi-tesla field bends the trajectories of charged particles, and from their curvatures the particle momenta can be determined.

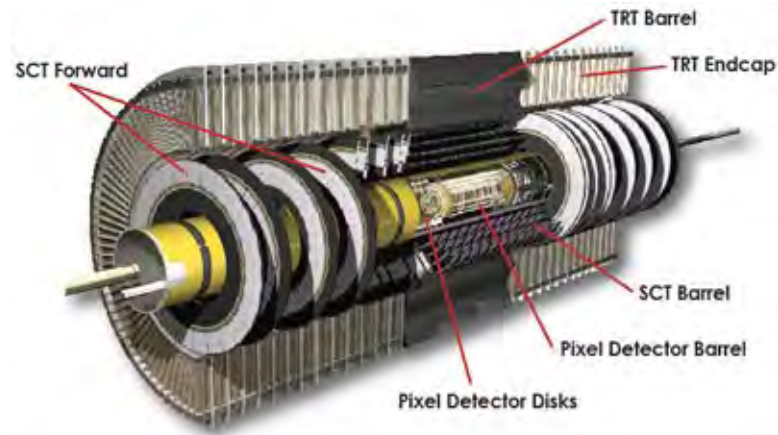


Figure 7.3: The inner detector of the ATLAS detector. Picture is taken from the ATLAS collaboration.

We focus on the inner detector of the ATLAS detector. From closest to the LHC beam pipe to the farthest, the inner detector consists of the pixel detector, the semiconductor tracker (SCT) and the transition radiation tracker (TRT). The pixel detector and SCT are silicon tracking system. The pixel detector has 80 millions silicon pixels while the SCT has 6 millions long silicon strips. They have maximum spatial resolutions of tens of μm across the cylindrical ϕ direction and hundreds of μm along the beam pipe direction. The TRT consists of long argon-filled straw detectors (drift tubes) with gold-plated tungsten sensing wires inside, which have a spatial resolution $170 \mu\text{m}$. The high overall position resolution of the inner detector is critical to tasks such as particle tracking, vertex reconstruction and bottom quark identification (b-tagging).

7.1.3 The ATLAS Pixel Detector

Among the three parts of the inner detector, the pixel detector [59] is the one with the greatest spatial resolution ($14 \times 115 \mu\text{m}^2$) and radiation hardness. It is a collection of silicon modules with $50 \times 400 \mu\text{m}^2$ sized pixels. The current pixel detector consists of 3 barrel layers and 3 end-cap disks on each end of the barrel. Until 2012, the innermost detector layer is the barrel layer 0. It is also called

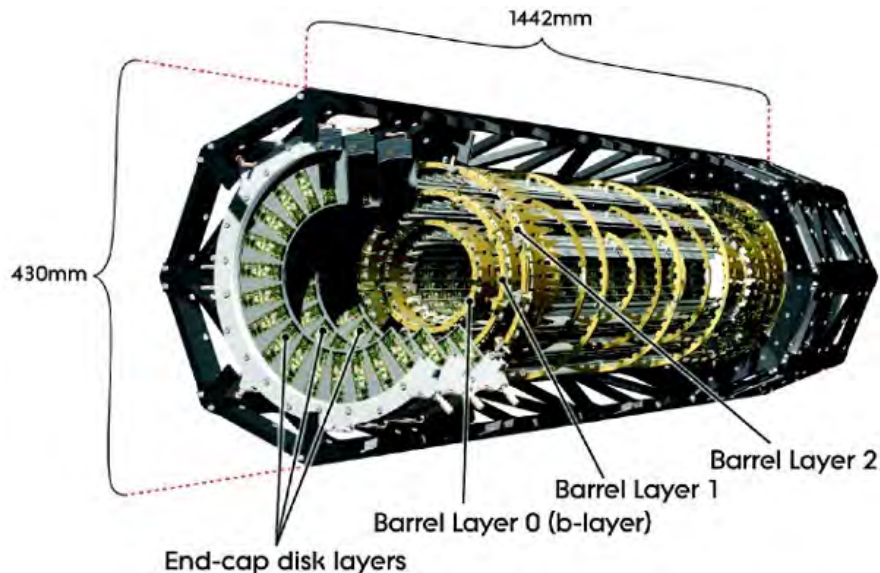


Figure 7.4: The pixel detector of the inner detector not including the insertible b-layer. Picture is taken from the ATLAS collaboration.

the b-layer for its importance in detecting the B hadrons, which decay within the tracker. The method for identifying b quarks is called b-tagging.

As the luminosity of the LHC increases, the high event pile-up makes the original b-layer incapable of b-tagging efficiently. In the phase-0 upgrade, a new Insertible B-Layer (IBL) [58] is inserted inside the b-layer. It is a layer closest to the beam pipe at a mean radius 33 mm. This additional pixel layer increases the number of pixel layers from three to four. It crucially increases the b-tagging performance, thus the physics performance, in the LHC Run 2.

Besides IBL, researches and developments are continuously carried to incorporate new ideas and technologies into the pixel system, to help the system to cope with the increasingly harsh environment in the future phases of the LHC [62].

7.1.4 FE-I4 Pixel Front-end Chip

The silicon sensors installed on the pixel detector are read out by front-end microchips which operate like the charge-coupled device (CCD) used in a digital camera. The read-out systems used in the pixel layers 0, 1 and 2 during Run

1 and 2 are the Front-End pixel Integrated circuits 3 (FE-I3) [60] fabricated with the standard complementary metal–oxide–semiconductor (CMOS) 250 nm process technology.

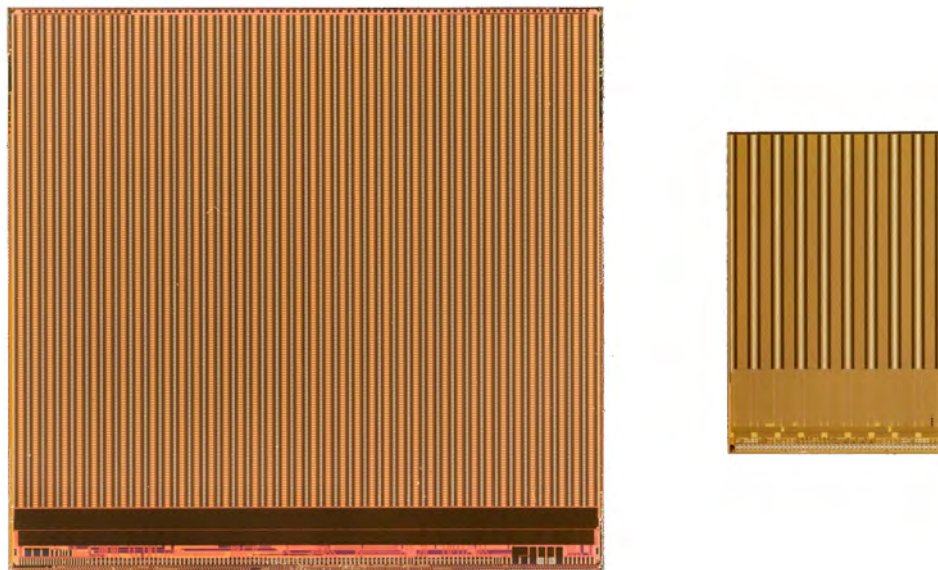


Figure 7.5: Comparison between the physical sizes of the $20 \times 18.6 \text{ mm}^2$ FE-I4 (left) and $7.6 \times 10.8 \text{ mm}^2$ FE-I3 (right). Photos are taken from Ref. [62].

The proposed phase-2 upgrade of the LHC to high-luminosity LHC (HL-LHC) increases the luminosity to $5 \times 10^{34} \text{ cm}^{-2} \text{ s}^{-1}$. The ultimate physics goal is to reach an integrated luminosity of 3000 fb^{-1} by year 2030. However, it also implies a 5-fold increase of pile-up rate from the nominal 28 events per bunch-crossing to ~ 140 events per bunch-crossing [61]. The FE-I3 pixel density and radiation tolerance are insufficient for handling such a high pixel hit rate. A new pixel chip FE-I4 [63, 65, 64] is developed to overcome these difficulties in the IBL and the future detector upgrade. The FE-I4 is currently used in the IBL, while the complete replacement of the other pixel layers front-end ICs with FE-I4s is proposed for the HL-LHC upgrade.

The FE-I4 is fabricated with the 130 nm CMOS process. It consists of a matrix of 80×336 pixels organized on a surface of size $20 \times 18.6 \text{ mm}^2$. The

FE-I4 has 89% active sensing area, an increase of 15% over its predecessor. The high active portion gives a better sensor coverage, which in turn improves the vertexing performance.

The reductions of chip operation voltage and current help reduce the power consumption and materials inside the inner detector. The introduction of pixel local buffers allows data to be stored at each pixel locally, such that a data transfer is made only when the buffers receive an L1 Trigger. This new read-out scheme lowers the bandwidth occupancy. With the increase of I/O bandwidth from 40 Mb/s to 160 Mb/s using 8b/10b encoding, the pixel detector inefficiency due to hit rate can be greatly reduced. The use of radiation-hardening techniques increase the chip's radiation tolerance at regions close to the beam pipe. All these technologies and designs combine to give FE-I4 the ability to handle the tough conditions at IBL and HL-LHC.

In the operational configuration, a silicon sensor is placed on top of the FE-I4s. Electrical connections is made onto both the top and bottom of the silicon sensor, to create a bias voltage.

When a charged particle traverses and deposits energy into the silicon sensor, electron-hole pairs are created. They drift according to the bias voltage and are read out by the FE-I4s under the sensor. Charge data (e.g. ToT) are first stored in the local buffer of each pixel in the FE-I4s. When a trigger condition from the detector is satisfied, a Level-1 (L1) trigger is sent to each pixel. Only then, the data in the pixel buffers are read out in a double-column configuration. The signals are then sent to some DAQ/read-out system outside (e.g. the end-of-stave read-out cards on each end of the pixel staves) using low-voltage differential signal (LVDS) operating at 0.6 - 3.0 mA. To reduce the current-per-pixel consumption, the LVDS voltage is much lower than the IEEE 1.2 V standard. Hence it is also called a pseudo-LVDS standard.

There are two subversions of FE-I4: The FE-I4A and FE-I4B, the detailed descriptions and specifications of which can be found in Ref [66] and [67] respec-

tively.

7.2 The SEABAS DAQ System

7.2.1 The SEABAS Boards

The new FE-I4s have to be fully tested offline before they are installed onto the pixel system. The tests are often carried out at laboratories in different universities, and sometimes in accelerator facilities when accelerator beam irradiation is required. These requirements suggest the need of portable DAQ systems that can easily connect to both the FE-I4 modules and personal computers. Therefore, the SEABAS (Soi EvAluation BoArd with Sitcp) read-out system [68] is developed as an electronic test bench for the FE-I4 and its related read-out modules (e.g. the pixel staves in Fig. 7.9b).

The SEABAS is an FPGA-based general purpose DAQ board developed by KEK in Japan. It implements a hardware-to-computer communication technology named the Silicon Transmission Control Protocol (SiTCP) [69], a hardware-based implementation of the User Datagram Protocol (UDP) and Transmission Control Protocol/Internet Protocol (TCP/IP), for the detector read-out chain. The SEABAS system is also well-proven as an offline DAQ system in the silicon strip super-module testing for the proposed SCT upgrade [70].

The SEABAS board contains two FPGAs. The SiTCP FPGA is a Xilinx Virtex-4 XC4VLX15-10FF668 [71] FPGA programmed with SiTCP communication firmware. The user FPGA, either a Virtex-4 XC4VLX25-10FF668 for SEABAS Version 1 or Virtex-5 XC5VLX50-1FFG676 [47] for SEABAS Version 2, is programmed with a user-specified firmware used to read-out a particular hardware (e.g. the FE-I4). With an FE-I4 daughter adapter board, the SEABAS DAQ board can at most connect to four FE-I4 test boards or their related modules simultaneously.

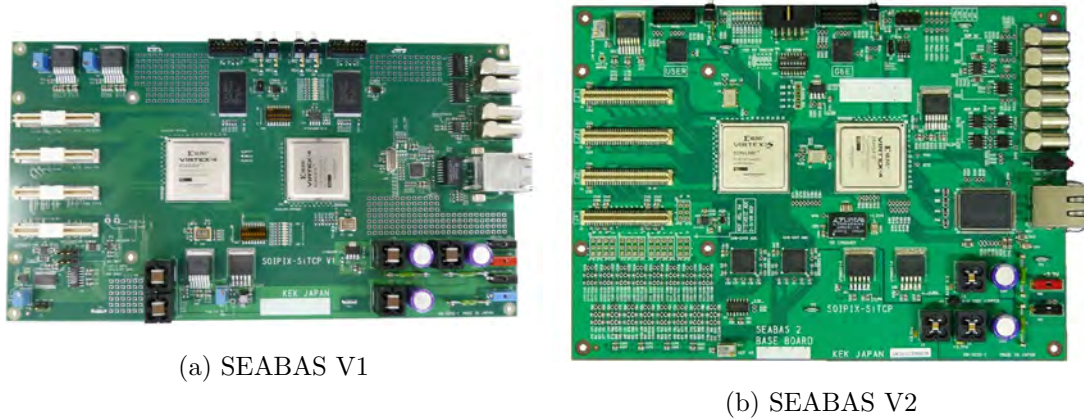


Figure 7.6: The two versions of SEABAS DAQ boards. Photos are taken from the High Energy Accelerator Research Organization (KEK) Silicon-on-insulator technology (Soi) SEABAS project webpage.

A detailed description of the SEABAS DAQ system for the FE-I4 read-out can be found in Teoh’s thesis [72].

7.2.2 SEABAS DAQ Firmware and Software

The FE-I4 tests that are available in the SEABAS system by Spring 2013 are injection tests, threshold scans, L1 trigger latency scan and ToT scans, etc. The list of tests, scans, and tunings can be found in Ref. [72]. The SEABAS firmware can also interface with four FE-I4 chips at once.

One of the aspects of the FE-I4 we are interested in is the noise occupancy. When there are no charged particles exciting the silicon sensors, the FE-I4 can still pick up non-zero signals when an L1 trigger is sent. The reading can be due to thermal noises, electromagnetic noises, circuit faults in the front-end, etc.

We have implemented the noise occupancy scan to test how many of the front-end channels are occupied by the noises. A known amount of L1 triggers are sent to the pixels. Without a sensor and a charge injection, the signals read-out from the pixels are purely noises. The read-out process is repeated with different front-end threshold levels. The noise occupancy as a function of the threshold level

can be found. Fig. 7.7 shows an example result of the noise occupancy scan.

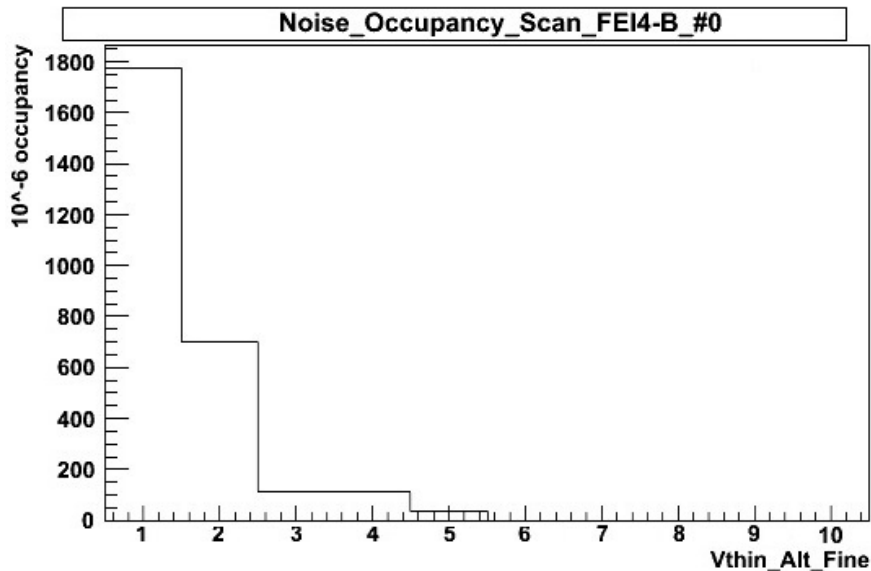


Figure 7.7: The result of a noise occupancy scan on an FE-I4 using 50 triggers. The plot shows counts per pixel per number-of-trigger versus threshold level.

Another scan of interest is the channel cross-talks scan. The cross-talk mechanism is very similar to that we discussed in the wire chamber section 5.2.5, except the channel density on the FE-I4 is much higher than that in the wire chamber. On the front-end pixels, the cross-talks are generated by the electronic signals from the local pixel read-out electronics. To investigate the magnitude of cross-talks, we analog inject charges onto some designated pixels while reading out all pixels, including those pixels without charge injection. Cross-talks noises are identified when an increased noise level in the cross-talk scan is detected compared to the noise occupancy scan.

There is a large parameter space to explore in crosstalk scans. We can investigate pixel-to-pixel, column-to-column, row-to-row and area-to-area crosstalks. In the pixel detector, four FE-I4s are packed together to read out the same silicon sensor. Therefore, FE-to-FE crosstalk is also possible.

In the crosstalk scan, we mask out some channels (pixels, rows, columns or

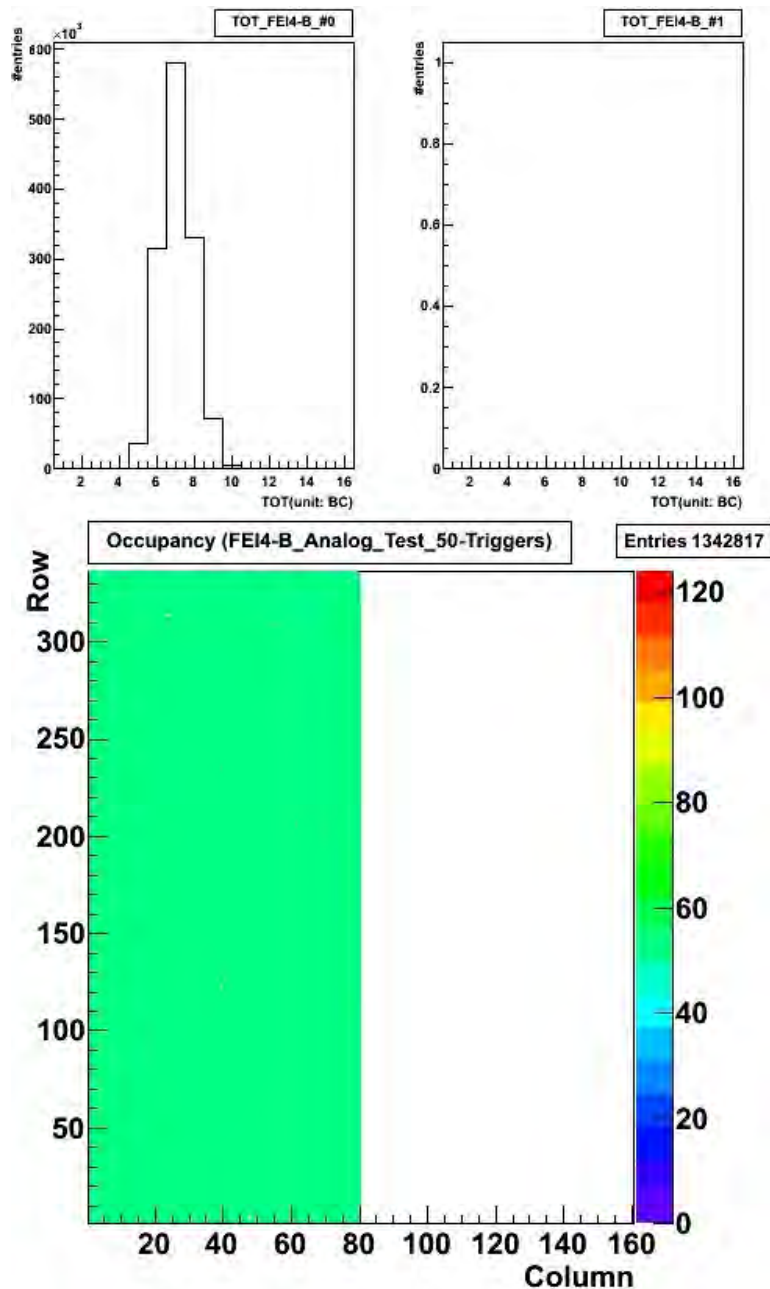


Figure 7.8: The result of a chip-to-chip crosstalk scan. 50 pulses are injected in FE 0. Then FE 0 and 1 are read out. No cross-talks are detected since we use two separate FE-I4 test boards instead of two FE-I4s on the same board.

front-ends) by turning off their injection charge capacitors. Then we send out analog injection commands, followed by L1 triggers to all channels. The signals read-out are the crosstalks plus the background noises in the masked channels.

In the unmasked channels, the signals include all the noises, the crosstalks and the injection pulses. The chip-to-chip crosstalk scan sample result is shown in Fig. 7.8.

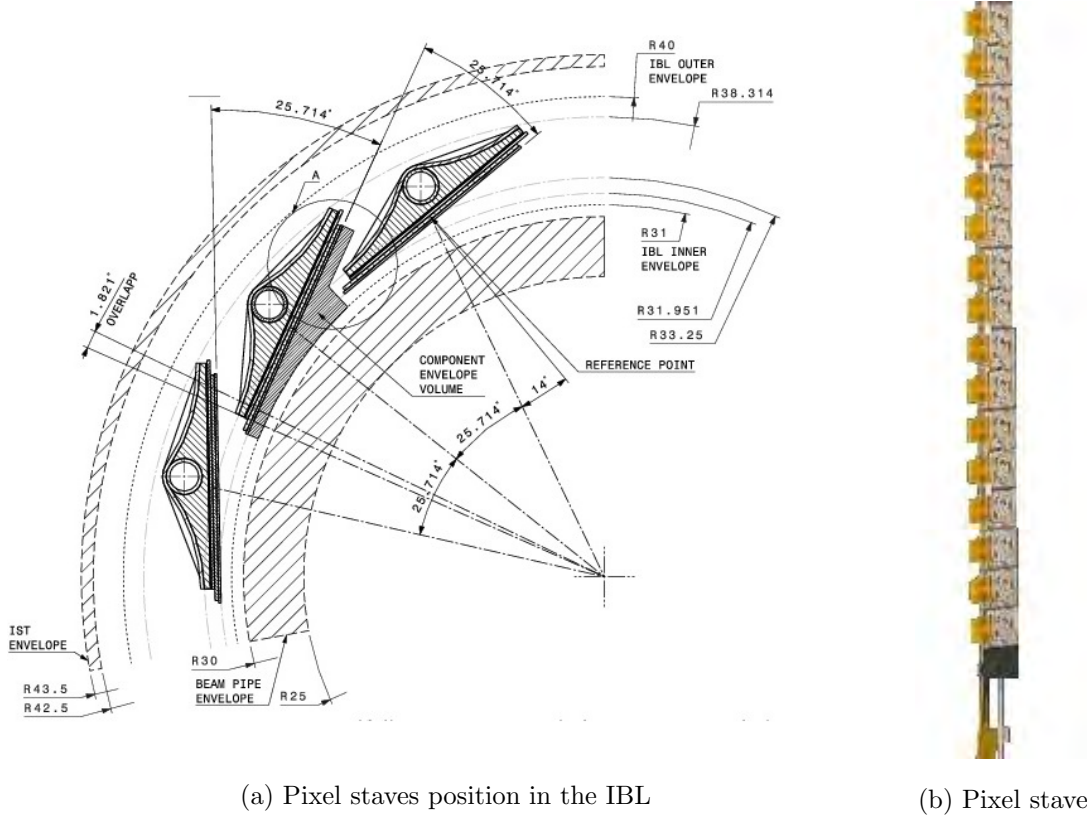


Figure 7.9: (a) $r - \phi$ plane cross-sectional schematic diagram from Ref. [73] showing the stave positions in the IBL. (b) Photo taken by Heinz Pernegger at CERN showing one stave with 16 pixel modules installed.

Moreover, we develop the framework for the FE-I4 to communicate with the pixel stave modules. The FE-I4s and silicon sensors are to be mounted on and read out by the pixel staves. One use of the pixel staves is in the IBL (Fig. 7.9a). More advanced pixel stave prototypes are being developed at the Lawrence Berkeley National Laboratory.

The pixel staves receive commands from an external DAQ through a capacitive-coupled command line. A general command signal through the line can be DC-biased. The DC-offset can charge up the capacitor, which leads to a distortion of

the digital command signal when the capacitor discharges.

Hence, we need to communicate with the stave using DC-balanced signals. We have implemented the G.E. Thomas Manchester Coding to the SEABAS-to-FE-I4 command lines. The Manchester coding scheme uses a double FPGA internal clock rate to convert an 1-bit DC signal to a 2-bit, double-rate AC signal, i.e. an “1” at 40 MHz is converted to “10” at 80 MHz, and a “0” is similarly converted to “01”.

When the FE-I4 is running at a 40 MHz clock sent by the SEABAS FPGA, it samples the command line at the rising edges of the 40 MHz clock, which is only a half of the 80 MHz Manchester-coded command line frequency. Therefore the FE-I4 samples only the first bit of every two bits of the 80 MHz command line. However, the Manchester coding only changes the second bit of the double frequency command. Meanwhile to the FE-I4, the command signals sent by the SEABAS are identical with or without Manchester coding. At the same time, DC-balance of the command signal is achieved.

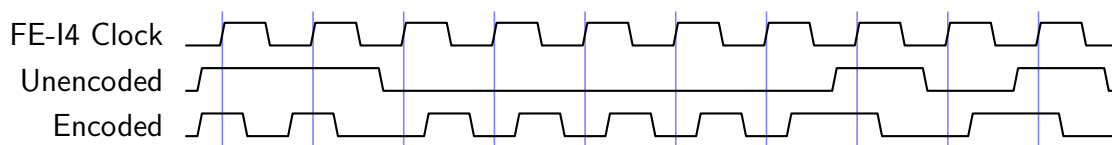


Figure 7.10: An example of the Manchester coding scheme implemented on the 10-bit End-Of-Frame command symbol “110000 0101”.

An example of the coding scheme implemented on the End-Of-Frame (EOF) command symbol is shown in Fig 7.10. The phase relation between the FE-I4 clock and the command signal is guaranteed since both signals are generated and sent by the SEABAS user FPGA.

Chapter 8

Conclusion

For the CUHK muon telescope experiment, we have simulated cosmic muon flux measured by the muon telescope. We have accounted for the interplanetary and Earth magnetic field, the Earth's atmosphere, the structure surrounding the muon telescope and the muon telescope acceptance. We read off the east-west and north-south flux asymmetries from the measured muon counts.

The simulation result is compared with the 1.5 years of cosmic muon data from the muon telescope experiment. All the 12 averaged measurement data points of the east-west and north-south effects at different zenith angles are consistent with the simulation within 1.5σ .

To get an even better angular resolution of the cosmic muon flux distribution, we have developed the CUHK multiwire chamber.

In the wire chamber development, we have designed a wire chamber geometry and simulated its operation using the Garfield-9 drift chamber simulator developed by CERN. We have also designed a front-end controlled by a digital microcontroller, an FPGA-based back-end and a set of Linux DAQ softwares. The wire chamber is ready to be tested and to take muon data.

For the ATLAS experiment at the CERN LHC, we continue the development of the SEABAS DAQ system for reading out a pixel detector front-end IC, called FE-I4. We have improved the SEABAS DAQ software to carry out noise oc-

cupancy scan and cross-talk scans. We have also introduced DC-balanced I/O for FE-I4 communication using Manchester coding. This helps the SEABAS to communicate with the FE-I4s through the pixel staves.

Appendix A

Muon Asymmetry Flux Effect Result Table

Combos	Best Fit Result	Simulation	σ agreement
E/W 1-offset	0.9153 ± 0.0050	0.9001 ± 0.0068	1.29
E/W 2-offset	0.8337 ± 0.0081	0.8622 ± 0.0110	1.49
N/S 1-offset	0.9567 ± 0.0051	0.9712 ± 0.0046	1.49
N/S 2-offset	0.9625 ± 0.0096	0.9382 ± 0.0076	1.41

Table A.1: Directional muon flux ratios at 40 cm separation result.

Combos	Best Fit Result	Simulation	σ agreement
E/W 1-offset	0.8918 ± 0.0074	0.8941 ± 0.0061	0.17
E/W 2-offset	0.844 ± 0.011	0.8611 ± 0.0110	0.78
N/S 1-offset	0.9682 ± 0.0081	0.9671 ± 0.0040	0.09
N/S 2-offset	0.982 ± 0.013	0.9468 ± 0.0081	1.67

Table A.2: Directional muon flux ratios at 32 cm separation result.

Combos	Best Fit Result	Simulation	σ agreement
E/W 1-offset	0.8821 ± 0.0041	0.8905 ± 0.0053	0.89
E/W 2-offset	0.8438 ± 0.0098	0.8651 ± 0.0100	1.08
N/S 1-offset	0.9538 ± 0.0043	0.9639 ± 0.0034	1.31
N/S 2-offset	0.945 ± 0.011	0.9615 ± 0.0086	0.84

Table A.3: Directional muon flux ratios at 24 cm separation result.

Appendix B

List of the SPI Reords for FE-BE Communication

Byte label	MOSI	MISO
header	0x01	0x00
payload 1	CH0 PWM duty cycle (0x00 - 0x64)	0x00
payload 2	CH1 PWM duty cycle (0x00 - 0x64)	0x00
	⋮	
payload 16	CH15 PWM duty cycle (0x00 - 0x64)	0x00

Table B.1: Write threshold using PWM duty cycle (max 128, min 0).

Byte label	MOSI	MISO
header	0x02	0x00
payload 1	0x00	CH0 PWM duty cycle (0x00 - 0x64)
payload 2	0x00	CH1 PWM duty cycle (0x00 - 0x64)
	⋮	
payload 16	0x00	CH15 PWM duty cycle (0x00 - 0x64)

Table B.2: Read threshold using PWM duty cycle (max 128, min 0).

Byte label	MOSI	MISO
header	0x03	0x00
payload 1	0x00	Lot Num 0
payload 2	0x00	Lot Num 1
payload 3	0x00	Lot Num 2
payload 4	0x00	Lot Num 3
payload 5	0x00	Lot Num 4
payload 6	0x00	Lot Num 5
payload 7	0x00	Wafer Num
payload 8	0x00	Wafer Coordinate X 1
payload 9	0x00	Wafer Coordinate X 2
payload 10	0x00	Wafer Coordinate Y 1
payload 11	0x00	Wafer Coordinate Y 2

Table B.3: Reading the 11-byte serial number of the front-end microcontroller.

Byte label	MOSI	MISO
header	0x03	0x00
payload 1	0x00	Temperature high byte
payload 2	0x00	Temperature low byte
payload 3	0x00	V_{cc} high byte
payload 4	0x00	V_{cc} low byte
payload 5	0x00	Bandgap high byte*
payload 6	0x00	Bandgap low byte*

Table B.4: Reading the internal microcontroller status. *The 1.1 V bandgap is measured with reference to the $V_{cc}/1.6$. All the other ADC values are measured with reference to internal 1 V.

Byte label	MOSI	MISO
header	0x05	0x00
payload 1	CH0 DAC Sample 1 low byte	0x00
payload 2	CH0 DAC Sample 1 high byte	0x00
payload 3	CH0 DAC Sample 2 low byte	0x00
payload 4	CH0 DAC Sample 2 high byte	0x00
payload 5	CH0 DAC Sample 3 low byte	0x00
payload 6	CH0 DAC Sample 3 high byte	0x00

Table B.5: Sending the DAC CH0 test pulse with 3 sampling points, each 2 bytes.

Byte label	MOSI	MISO
header	0x06	0x00
payload 1	CH1 DAC Sample 1 low byte	0x00
payload 2	CH1 DAC Sample 1 high byte	0x00
payload 3	CH1 DAC Sample 2 low byte	0x00
payload 4	CH1 DAC Sample 2 high byte	0x00
payload 5	CH1 DAC Sample 3 low byte	0x00
payload 6	CH1 DAC Sample 3 high byte	0x00

Table B.6: Sending the DAC Ch1 test pulse with 3 sampling points, each 2 bytes.

Byte label	MOSI	MISO
header	0x07	0x00
payload 1	0x00	ADC CH1 threshold high byte
payload 2	0x00	ADC CH1 threshold low byte
payload 3	0x00	ADC CH2 threshold high byte
payload 4	0x00	ADC CH2 threshold low byte

Table B.7: Reading the PWM threshold feedbacks from the ADC Ch1 and Ch2

Byte label	MOSI	MISO
header	0xDD	0x00
payload 1	0x??	0x??

Table B.8: Echoing 1 byte from the back end.

Byte label	MOSI	MISO
header	0xDE	0x00
payload 1	0x??	0x?? + 0x01
payload 2	0x??	0x?? + 0x01
	\vdots	
payload 8	0x??	0x?? + 0x01

Table B.9: Taking 8 bytes and returning the byte value plus 1.

Appendix C

List of the Back-end Addresses

Back-end Function	Address Byte	I/O Type
Reset Back-end	00	I
On-board Light Emission Diodes	01	I
On-board Button	02	O
On-board Flip Switches	03	O
Firmware Revision	04	O
Channel 0 Time Stamp	06	O
Channel 1 Time Stamp	07	O
Channel 2 Time Stamp	08	O
Channel 3 Time Stamp	09	O
Channel 0 Input Mask Low Byte	10	I
Channel 0 Input Mask High Byte	11	I
Channel 1 Input Mask Low Byte	12	I
Channel 1 Input Mask High Byte	13	I
Channel 2 Input Mask Low Byte	14	I
Channel 2 Input Mask High Byte	15	I

Table C.1: List A of back-end address accessible by the DAQ software.

Back-end Function	Address Byte	I/O Type
Channel 3 Input Mask Low Byte	16	I
Channel 3 Input Mask High Byte	17	I
Test Event Trigger	21	I
Read Event FIFO Data	24	O
Read Event FIFO Index	25	O
Read Event FIFO Count	26	O
Control Single Rate	27	I
Read Single Rate Data	28	O
Read Single Rate Count	29	O
Write Liquid-crystal Display FIFO	30	I
Read Liquid-crystal Display FIFO	31	O
Write LB FIFO	40	I
Read LB FIFO	41	O
Transmit SPI Data	50	I
Receive SPI Data	51	O
Set Front-End Address	54	I
Coincidence Combo Low Byte	68	I
Coincidence Combo High Byte	69	I
Coincidence Time Window Size	6A	I
Read Error Vector 0	F0	O
Read Error Vector 1	F1	O
Firmware Revision	20	O

Table C.2: List B of back-end address accessible by the DAQ software.

Bibliography

- [1] Daya Bay Collaboration, A Precision Measurement of the Neutrino Mixing Angle θ_{13} using Reactor Antineutrinos at Daya Bay, arXiv: hep-ex/0701029v1 (2007).
- [2] Daya Bay Collaboration, The Muon System of the Daya Bay Reactor Antineutrino Experiment, arXiv:1407.0275v2 (2014).
- [3] ATLAS Collaboration, The ATLAS Experiment at the CERN Large Hadron Collider, J. Instrum. 3 S08003 (2010).
- [4] ATLAS Collaboration, Commissioning of the ATLAS Muon Spectrometer with Cosmic Rays, Eur. Phys. J. C70:875-916 (2010).
- [5] ATLAS Collaboration, The ATLAS Inner Detector Commissioning and Calibration, Eur. Phys. J. C70:787-821 (2010).
- [6] E. J. Smith, The Heliospheric Current Sheet and Modulation of Galactic Cosmic Rays, J. Geophys. Res., Vol 95, No. A11 (1990).
- [7] N. Marsh, et al., Cosmic Rays, Clouds, and Climate, Space Science Reviews 00: 1–16 (2000).
- [8] J. Kirkby et al. Role of Sulphuric Acid, Ammonia and Galactic Cosmic Rays in Atmospheric Aerosol Nucleation, Nature 476, 429-433 (2011).
- [9] J. F. Ziegler et al., The effect of Sea Level Cosmic Rays on Electronic Devices, J. Appl. Phys., Vol. 52, No.6 (1981).

- [10] J. F. Ziegler et al., IBM Experiments in Soft Fails in Computer Electronics (1978–1994), IBM J. Res. Develop. Vol. 40 No. 1 (1996).
- [11] K. Borozdin et al., Cosmic Ray Radiography of the Damaged Cores of the Fukushima Reactors, Phys. Rev. Lett. 109. 152501 (2012).
- [12] A. R. Bell, The Acceleration of Cosmic Rays in Shock Fronts, Monthly Notices of the Royal Astronomical Society, Vol. 182 (1978). P.147-156.
- [13] Fermi-LAT collaboration, Detection of the Characteristic Pion-Decay Signature in Supernova Remnants, Science, Vol. 339, No. 6121 (2013). Page. 807-811
- [14] D.F. Smart et al., A Review of Geomagnetic Cutoff Rigidities for Earth-orbiting Spacecraft, Adv. Space Res. 36 (2005). P. 2012 - p. 2020.
- [15] J.J. Quenby et al., Cosmic Ray Threshold Rigidities and the Earth's Magnetic Field, Phil. Mag., Vol 7, 81 (1962).
- [16] Particle Data Group, Review of Particle Physics, Phys. Rev. D86, 010001 (2012). P.305 - p. 311.
- [17] J. Cronin et al., Cosmic Rays at the Energy Frontier, Scientific American 276, 1, 44 (1997).
- [18] T. Hebbeker, et al., A Compilation of High Energy Atmospheric Muon Data at Sea Level, Astropart. Phys. 18 (2002) P. 107 - p. 127.
- [19] T. K. Gaisser, Cosmic rays and particle physics, Cambridge, UK: Univ. Pr. (1990). P. 279.
- [20] A. Tang et al., Muon Simulations for Super-Kamiokande, KamLAND and CHOOZ, Phys. Rev. D 74:053007 (2006).
- [21] C.G.S. Costa, The Prompt Lepton Cookbook, Astropart. Phys. 16 (2001). P. 193 - p. 204.

- [22] Y. L. Chan, Study of Cosmic Ray Variation in Hong Kong, M. Phil. in Physics thesis, Chin. Univ. Hong Kong (2012).
- [23] Y. H. Tam, Study of Cosmic-ray Muons and Muons Induced Neutrons, Ph. D. in Physics thesis, Chin. Univ. Hong Kong (2013).
- [24] Xilinx Inc., Spartan-3E FPGA Family Data Sheet, DS312 v4.1 data sheet (2013).
- [25] Digilent, Inc., Digilent Nexys2 Board Reference Manual, Doc 502-107 Revision June 21, 2008.
- [26] Hamamatsu Photonics K. K., Photosensor Modules H7826 Series, H7826 Series Catalog, Jan 2008.
- [27] International Association of Geomagnetism and Aeronomy, Working Group V-MOD, International Geomagnetic Reference Field: the Eleventh Generation, *Geophysical Journal International*, vol. 183, Dec 2010. P. 1216 - p. 1230.
- [28] N. A. Tsyganenko, A Model of the Near Magnetosphere with a Dawn-dusk Asymmetry 1 and 2, *J. Geophys. Res.*, vol. 107 (2002).
- [29] S. Agostinelli et al., Geant4 - A Simulation Toolkit, *Nuclear Instrum. Methods* 506, 3 (2003). P. 250 - p. 303.
- [30] D. P. Dee et al., The ERA-Interim Reanalysis: Configuration and Performance of the Data Assimilation System, *Q. J. R. Meteorol. Soc.*, Vol 137 (2002). P. 553 - p. 597.
- [31] J. Picone et al., NRLMSISE-00 Empirical Model of the Atmosphere: Statistical Comparisons and Scientific Issues, *J. Geophys. Res.*, Vol 107 (2002).
- [32] Donald E. Groom, et al., Muon Stopping Power And Range Tables 10 MeV – 100 TeV, *Atomic Data and Nuclear Data Tables*, Vol 78, Issue 2 (2001). P. 236.

- [33] Particle Data Group, Review of Particle Physics, Phys. Rev. D86, 010001 (2012). P. 348 - p. 349.
- [34] Atmel Corporation, 8/16-bit Atmel XMEGA A3BUMicrocontroller, 8362F-AVR-02 datasheet (2013).
- [35] Luma Metall, Luma Gold Plated Tungsten Wire, gold plated tungsten wire product sheet (2012).
- [36] T. Trippe, Minimum Tension Requirement for Charpak-Chamber Wires, CERN NP Internal Report 69-18 (1969). P. 4.
- [37] F. Sauli, Principles of Operation of Multiwire Proportional and Drift Chambers, Lectures given in the Academic Training Programme of CERN (1977). P. 52.
- [38] W. R. Leo, Techniques for Nuclear and Particle Physics Experiments, Springer-Verlag (1987).
- [39] G. A. Erskine, Electrostatic Problems in Multiwire Proportional Chambers, Nuclear Instrum. Methods 105, 565 (1972). P. 566.
- [40] W. Diethorn, A Methane Proportional Counter System for Natural Radio-carbon Measurements, US AEC Rep. NYO-6628 (1956).
- [41] R. S. Wolff, Measurements of the Gas Constants for Various Proportional Counter Gas Mixtures, Nuclear Instrum. Methods , 115, 461 (1974).
- [42] R. Veenhof, GARFIELD: a Drift Chamber Simulation Program User's Guide, CERN Program Library, W5050 (1993).
- [43] R. Veenhof, Garfield, Recent Developments, Nuclear Instrum. Methods A, 419 (1998). P. 726 - p. 730.
- [44] L.G. Christophorou, et al., Fast Gas Mixtures for Gas-filled Particle Detectors, Nuclear Instrum. Methods , 163, 1 (1979).

- [45] W. Blum et al., Particle Detection with Drift Chamber, Springer (2008). P. 75.
- [46] Caen Technologies, Inc., N471/NIM High Voltage Power Supply, N471 2 Channel 8 kV Power Supply product sheet (2014).
- [47] Xilinx, Inc., Virtex-5 Family overview, DS100 v5.0 data sheet (2009).
- [48] Digilent, Inc., Genesys Board Reference Manual, Doc 502-138 Revision May 8, 2014.
- [49] Lyndon Evans and Philip Bryant, LHC Machine, JINST 3 S08001 (2008).
- [50] LHCb collaboration, The LHCb Detector at the LHC, JINST 3 S08005 (2008).
- [51] ALICE collaboration, The ALICE experiment at the CERN LHC, JINST 3 S08002 (2008).
- [52] CMS collaboration, The CMS experiment at the CERN LHC, JINST 3 S08004 (2008).
- [53] ATLAS collaboration, Observation of a New Particle in the Search for the Standard Model Higgs Boson with the ATLAS Detector at the LHC, Phys. Lett. B, Vol 716, 1 (2012). P.1 - p.29.
- [54] CMS collaboration, Observation of a New Boson at a Mass of 125 GeV with the CMS Experiment at the LHC, Phys. Lett. B, Vol 716, 1 (2012). P. 30 - p. 61.
- [55] F. Englert and R. Brout, Broken Symmetry and the Mass of Gauge Vector Mesons, Phys. Rev. Lett. 13, 321 (1964).
- [56] P. W. Higgs, Broken Symmetries and the Masses of Gauge Bosons, Phys. Rev. Lett. 13, 508 (1964).

- [57] G. S. Guralnik, C. R. Hagen, and T. W. B. Kibble, Global Conservation Laws and Massless Particles, *Phys. Rev. Lett.* 13, 585 (1964).
- [58] ATLAS IBL Collaboration, ATLAS IBL Pixel Upgrade, *Nuclear Physics B* 215 (2011). P. 147 - p. 150.
- [59] G. Aad, et al., ATLAS Pixel Detector Electronics and Sensors, *JINST* 3 P07007 (2008).
- [60] I. Perić, et al., The FEI3 Readout Chip for the ATLAS Pixel Detector, *Nuclear Instrum. Methods A*, 565, 1 (2006). P. 178 - p. 187.
- [61] P. Vankov, ATLAS Upgrade for the HL-LHC: Meeting the Challenges of a Five-fold Increase in Collision Rate, 2011 Hadron Collider Physics symposium (HCP-2011), ATL-UPGRADE-PROC-2012-003 (2012).
- [62] M. Garcia-Sciveres and ATLAS Collaboration, ATLAS Experiment Pixel Detector Upgrades, DPF 2011 proceedings, ATL-UPGRADE-PROC-2011-006 (2011).
- [63] M. Garcia-Sciveres, et al., The FE-I4 Pixel Readout Integrated Circuit, *Nuclear Instrum. Methods A*, 636, 1 (211). P. S155 - p. S159.
- [64] M. Karagounis, et al., Development of the ATLAS FE-I4 Pixel Readout IC for B-layer Upgrade and Super-LHC, Naxos 2008, Electronics for Particle Physics', CERN-2008-008 (2008). P. 70 - p. 75.
- [65] T. Hemperek, et al., Digital Architecture of the New ATLAS Pixel Chip FE-I4, *IEEE Nuclear Science Symposium Conference Record*, N13-179 (2009).
- [66] FE-I4 Collaboration, The FE-I4A Integrated Circuit Guide, Version 11.6 (2011).
- [67] FE-I4 Collaboration, The FE-I4B Integrated Circuit Guide, Version 2.3 (2012).

- [68] J. J. Teoh, et al., Development of Readout System for FE-I4 Pixel Module Using SiTCP, Nuclear Instrum. Methods A, 731 (2013). P. 237 - p. 241.
- [69] T. Uchida, Hardware-Based TCP Processor for Gigabit Ethernet, IEEE trans. on Nuclear Science, vol. 55, no. 3 (2008).
- [70] Y. Takubo, et al., Development of SiTCP Based DAQ System of Double-sided Silicon Strip Super-module, Nuclear Instrum. Methods A, 699 (2011). P. 116 - p. 119.
- [71] Xilinx, Inc., Virtex-4 Family overview, DS112 v3.1 data sheet (2010).
- [72] J. J. Teoh, Development of SiTCP Based Readout System for the ATLAS Pixel Detector Upgrade, Master thesis in Physics, Yamanaka Taku Laboratory, Osaka University, Japan (2012).
- [73] F. Hügging and ATLAS Collaboration, The ATLAS Pixel Insertable B-Layer (IBL) Nuclear Instrum. Methods A, 650, 1 (2011) P. 45 - p. 49.